NUMERICAL METHODS FOR DIRECTIONAL COUPLING DETECTION FROM TIME SERIES OF COMPLEX SYSTEMS

Martin Brešar

Doctoral Dissertation
Jožef Stefan International Postgraduate School
Ljubljana, Slovenia

Supervisor: Assoc. Prof. Dr. Pavle Boškoski, Jožef Stefan Institute, Ljubljana, Slovenia

Evaluation Board:
Prof. Dr. Juš Kocijan, Chair, Jožef Stefan Institute, Ljubljana, Slovenia
Assoc. Prof. Dr. Zoran Levnajić, Member, Faculty of Information Studies in Novo mesto, Novo mesto, Slovenia
Prof. Dr. Ralph Gregor Andrzejak, Member, Universitat Pompeu Fabra, Barcelona, Spain

MEDNARODNA PODIPLOMSKA ŠOLA JOŽEFA STEFANA
JOŽEF STEFAN INTERNATIONAL POSTGRADUATE SCHOOL

Martin Brešar

NUMERICAL METHODS FOR DIRECTIONAL COUPLING DETECTION FROM TIME SERIES OF COMPLEX SYSTEMS

Doctoral Dissertation

NUMERIČNE METODE ZA DETEKCIJO USMERJENIH SKLOPITEV IZ ČASOVNIH VRST KOMPLEKSNIH SISTEMOV

Doktorska disertacija

Supervisor: Assoc. Prof. Dr. Pavle Boškoski

Ljubljana, Slovenia, August 2024

Acknowledgments

I want to express my deepest gratitude to my supervisor, Assoc. Prof. Dr. Pavle Boškoski, for his guidance, support, and insightful feedback throughout my research. He always took the time to address my questions and concerns, providing invaluable advice and encouragement. From the very beginning, he ensured a relaxed and welcoming environment. I am also thankful to my master's supervisor, Asst. Prof. Dr. Martin Horvat, who, together with Dr. Boškoski, introduced me to the field of my research. Their combined mentorship during my master's studies inspired me to pursue this path. Finally, I would like to thank Prof. Dr. Ralph G. Andrzejak for many insightful discussions that brought me new perspectives to my research, which will surely benefit me in the future.

Furthermore, I would also like to thank all my colleagues at the Jožef Stefan Institute for creating a positive and collaborative atmosphere. We enjoyed countless coffees with interesting discussions on various topics, ranging from scientific theories to everyday life. Special thanks go to Luka and Žiga for fostering a great atmosphere in the office and making our workplace enjoyable and motivating.

I would also like to acknowledge the support of the Young Researchers Programme grant no. PR-10490 and the Research Programme no. P2-0001 of the Slovenian Research and Innovation Agency.

I am also profoundly grateful to my friends, who helped to make the PhD process more pleasant: Luka and Ana, Žiga and Meta, Tilen, Žan and Lana, Tomaž, Sara, Marko, Aljaž, Klemen, Jaka, Andrej, Jan, and many others.

Above all, my deepest gratitude goes to my parents, brother Jure, grandmothers, cousins, uncles and aunts, and everyone else—for their endless support, encouragement, and love throughout my academic journey. Thank you.

Abstract

Complex systems, composed of numerous interacting subsystems, exhibit intricate dynamics that are challenging to model and understand. This dissertation focuses on advancing methodologies for detecting the direction and quantifying the strength of couplings in such systems and presents their application to real data. The basics of dynamical systems and chaos are first presented, followed by an introduction to couplings and synchronization. Then, the methodology for detecting couplings from measured time series is presented. This includes the Granger causality, the phase dynamics methods, the information methods, and the state space methods, with an emphasis on the latter two. An alternative approach called perturbation experiments, applicable to systems that can be directly influenced, is also presented. The subsequent chapters present original research and practical applications.

The first part of the research addresses the solvability of the inverse problem, specifically whether the coupling strength parameter can be inferred from time series by computing information flow. Findings reveal this is possible for weak couplings but not when the response system is highly sensitive to perturbations. Additionally, for strong diffusive couplings, information flow decreases monotonically with increasing coupling strength, making the inverse problem solvable, given that coupling is strong enough.

The research's second part improves the state space methods for directional coupling detection. By introducing cross-distance vectors and analyzing their response to coupling, the initial tails of the cross-distance vectors are recognized as containing information about the coupling. A new measure is defined that quantifies the prominence of this initial tail, enhancing the accuracy of the state space measures and reducing the risk of false positives. This advancement increases the reliability of such methods, broadening their applicability across various scientific fields. Furthermore, a rank-based state space measure is introduced and combined with surrogate data. Application to an EEG database demonstrates the measure's enhanced ability to differentiate between focal and nonfocal EEG signals, highlighting its potential in clinical applications.

The final part presents a perturbation experiment and an analysis of the resulting time series. The experiment is conducted on patients with severe aortic valve stenosis and a healthy control group, with the goal of quantifying neurovascular coupling strength. Results show that computing the visually evoked cerebral blood flow velocity response to quantify the coupling strength can effectively distinguish between the aortic stenosis group and the healthy control group, as found by detecting a statistically significant difference.

Overall, this dissertation provides contributions to the field of detecting interactions within complex systems, offering improved methods for detecting and quantifying directional couplings and demonstrating their practical applications in medical research.

Povzetek

Za kompleksne sisteme, sestavljene iz številnih medsebojno sklopljenih podsistemov, je značilna zapletena dinamika, ki jo je težko modelirati in razumeti. Ta disertacija se osredotoča na razvoj metodologije za detekcijo smeri in kvantifikacijo moči sklopitev v takšnih sistemih ter predstavi njihovo uporabo na izmerjenih podatkih. Najprej so predstavljene osnove dinamičnih sistemov in kaosa, sledi uvod v sklopitve in sinhronizacijo. Nato je predstavljena metodologija za detekcijo sklopitev iz merjenih časovnih vrst. To vključuje Grangerjevo kavzalnost, metode fazne dinamike, informacijske metode in metode faznega prostora, pri čemer je poudarek na zadnjih dveh. Predstavljen je tudi alternativni pristop s perturbacijskim eksperimentom, ki je uporaben za sisteme, na katere imamo neposredni vpliv. Naslednja poglavja predstavljajo izvirne raziskave in praktične aplikacije.

Prvi del raziskav obravnava rešljivost inverznega problema, torej ali je mogoče iz časovnih vrst z izračunom pretoka informacij določiti parameter moči sklopitve. Ugotovitve kažejo, da je to mogoče pri šibkih sklopitvah, vendar ne, ko je gnani sistem zelo občutljiv na perturbacije. Poleg tega se pri močnih difuzijskih sklopitvah pretok informacij monotono zmanjšuje z naraščajočo močjo sklopitve, kar omogoča rešljivost inverznega problema, če je sklopitev dovolj močna.

Drugi del raziskav izboljša natančnost metod za detekcijo sklopitev, ki temeljijo na faznem prostoru. Z uvedbo vektorjev medsebojnih razdalj in analizo njihovega odziva na sklopitve se začetni repi teh vektorjev izkažejo kot nosilci informacije o sklopitvi. Z definicijo novega indeksa, ki kvantificira izstopanje tega začetnega repa, se izboljša natančnost teh metod in zmanjša tveganje lažnih pozitivnih rezultatov. Ta napredek poveča zanesljivost ter uporabnost takšnih metod v različnih področjih. Poleg tega je predstavljen nov indeks, ki temelji na rangiranju. Lahko ga kombiniramo z metodo nadomestnih signalov. Aplikacija na bazi EEG podatkov kaže izboljšano sposobnost razlikovanja med fokalnimi in nefokalnimi EEG signali, kar poudarja potencial novega indeksa v kliničnih aplikacijah.

Zadnji del predstavi perturbacijski eksperiment in analizo pridobljenih časovnih vrst. Eksperiment je bil izveden na pacientih z aortno stenozo in na zdravi kontrolni skupini s ciljem kvantifikacije moči nevrovaskularne sklopitve. Rezultati pokažejo, da s kvantifikacijo moči sklopitve lahko efektivno razločimo med skupino z aortno stenozo in zdravo kontrolno skupino, saj med njima obstaja statistično signifikantna razlika.

Kot celota ta disertacija prispeva k področju detekcije interakcij v kompleksnih sistemih. Predstavi izboljšane metode za detekcijo in kvantifikacijo usmerjenih sklopitev ter prikaže njihove praktične aplikacije v medicini.

Contents

List of Figures

List of Tables

Abbreviations

CMI ... conditional mutual information
CLE ... conditional Lyapunov exponent
ECG ... electrocardiogram
EEG ... electroencephalogram
AS ... aortic stenosis
PCA ... posterior cerebral artery
VEFR .. visually evoked cerebral blood flow velocity response

Chapter 1

Introduction

Complex systems consist of numerous interacting components known as subsystems. Some examples include the human body, ecosystems, the Earth's climate, and financial markets. The distinction between systems and subsystems is largely for convenience and depends on the context. For example, the human body consists of subsystems such as the cardiac system, the vascular system, the respiratory system, and the brain. However, the brain can also be considered a system that consists of many neurons, which are its subsystems. Generally, the main point that defines subsystems is that they are never truly separate due to their mutual interactions.

Complex systems are often hard to model due to a large number of interacting components or due to the possibly complex behavior of their components. In the example of the human body, the heart, i.e., the cardiac subsystem is a complicated system in itself. Although some useful models describing its dynamics have been introduced, the exact dynamics underlying it remain unknown. Including interactions between the heart and all the other parts of the human body significantly increases the difficulty of modeling, if not makes it impossible.

Additionally, the interactions themselves can be complicated. A well-explored example is the relationship between the cardiac and the respiratory subsystems of the human body, called cardiorespiratory coupling. The cardiac subsystem influences the respiratory subsystem by a single mechanism, while the respiratory subsystem influences the cardiac subsystem by three different mechanisms, resulting in a complex interaction [1].

In order to be able to study different systems, one has to characterize them somehow. This can be done by measuring available quantities pertaining to a subsystem. For example, the cardiac system can be characterized with an electrocardiogram (ECG), which measures the heart's electrical activity. This results in a time series, which consists of values of the measured quantity at different points in time. By measuring the time series of a number of subsystems, one can study both the dynamics of individual subsystems and the relationships between them. The focus of this dissertation is the latter.

The study of interactions between systems is also referred to as causal inference. Knowledge about these interactions is just as crucial as knowledge about the systems themselves, as they can reveal emergent properties and dynamics that are not apparent when the subsystems are considered in isolation. Thus, various methods for detecting interactions from measured time series of complex systems have been developed. Two related methodologies can be distinguished. The first is network reconstruction, which focuses on uncovering the various connections within a large number of mutually interacting systems. The second is detecting directional couplings, which aims to infer the direction of coupling between a pair of systems and quantify its strength as accurately as possible. This dissertation considers the latter methodology, emphasizing the accurate detection of individual directional

couplings. It is widely used in various fields, for example in economy [2]–[4], ecology [5], [6], medicine [7]–[10], neuroscience [11]–[13], and Earth system sciences [14], [15].

1.1 Directional Couplings

Consider two systems X and Y, depicted in Figure 1.1. Two properties can characterize an interaction between a pair of subsystems. The first is the *direction of coupling*. The second is the *strength of coupling*. There are four possibilities for the direction of coupling between X and Y:

1. The two subsystems can be independent, meaning there are no interactions between them.
2. The subsystem X can influence the subsystem Y and not vice versa. In this scenario, X is called the *driver* and Y the *response*, reflecting their respective roles within their interaction.
3. The subsystem Y can influence the subsystem X and not vice versa, which makes Y the driver and X the response.
4. Both subsystems can mutually influence each other, in which case no distinction between the driver and the response can be made.

The interaction in the second and the third scenario is considered a *unidirectional coupling*, and the interaction in the last one is considered a *bidirectional coupling*.

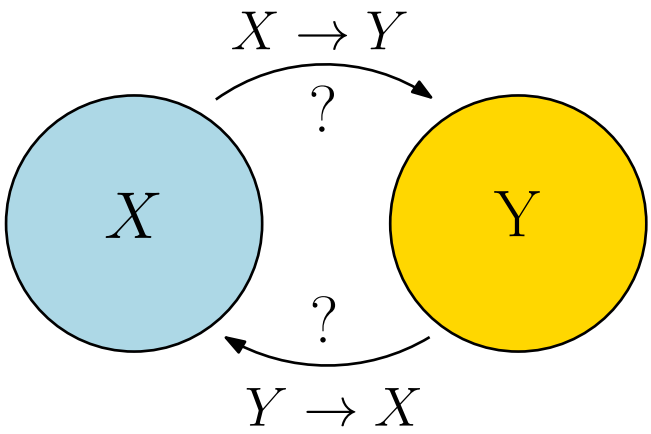

Figure 1.1: A depiction of two interacting subsystems X and Y. The arrows represent the possible directional couplings between them.

On the other hand, the strength of coupling is a continuous value. It can be weak, in which case the dynamics are often similar to those of the isolated subsystems but with a slight perturbation. At the other extreme, when coupling is strong, synchronization can occur, meaning the subsystems can no longer be considered as two separate parts of the whole system but rather as one.

In this dissertation, two different approaches to detecting directional couplings are introduced. The first is used when one does not have direct control over the measured systems. In this case, the time series are measured from the system without an external perturbation to the measured subsystems. The second approach is used when influencing a subsystem is possible, allowing one to discern whether or how another subsystem responds

to this perturbation. For example, one cannot directly influence the Earth's climate, which necessitates adopting the first approach. An example of the second approach is inducing variations in the breathing frequency, allowing one to assess how this affects the heart rate via the cardiorespiratory coupling.

1.2 The Purpose of the Dissertation

The purpose of the dissertation can be divided into three parts:

1. The first pertains to the solvability of an inverse problem of inferring the coupling strength from the information flow. While information flow has been shown to generally increase with increased coupling strength, this relationship has not been thoroughly investigated in different scenarios. This dissertation aims to explore this in greater detail with the purpose of assessing the behavior of information flow in systems in different dynamical regimes.

2. The second concerns state space based methods. While they excel in sensitivity to directional couplings, they are also influenced by other signal properties and, thus, often tend to result in a false positive. The advancement is improving these approaches to decrease the probability of receiving a false positive result. The purpose is to increase the reliability of state space measures, increasing their applicability to various fields of science.

3. The third relates to a perturbation experiment within a clinical study. Conducting an experiment and analyzing the resulting time series allowed for the quantification of neurovascular coupling. The purpose is to provide an index that quantifies this coupling, enabling physicians to perform further statistical analysis.

1.3 Goals

Different methods for coupling detection have different advantages and disadvantages. Understanding the setting for which they were devised is crucial for the correct application, as using the methods incorrectly can lead to false results. With this in mind, the goals of this dissertation are:

1. **Solvability of the inverse problem**: The first goal pertains to the behavior of information flow in the limit of infinite time series length. Information flow between two systems can be estimated from their time series by computing the transfer entropy. The result is two indices, each quantifying information flow between systems in one direction. Information flow has been shown to generally increase with increased coupling strength. However, a thorough investigation of whether and in which cases this increase is strictly monotonic has yet to be done. Thus, the first goal is to assess when, in the limit of infinite time series length, the coupling strength between two dynamical systems uniquely determines information flow.

2. **Increasing the accuracy of state space measures**: The second goal is to improve the accuracy of state space approaches for directional coupling detection. The classical state space measures are excellent at detecting weak directional couplings. However, they have the drawback of being strongly influenced by other signal properties, such as linear cross-correlation, decreasing their reliability in applications. The goal is to alleviate this drawback by introducing an improved state space measure that is less influenced by such properties.

3. **Combining the improved state space measures with surrogate data**: The state space measures always yield nonzero values in practical situations with finite-length time series, even though their expected value across realisations is zero. The surrogate data method offers a statistical test to determine if obtained values are statistically significant, indicating the presence of genuine interactions. Although the new measure discussed earlier in this section has increased accuracy, combining it with surrogate data can present challenges. Therefore, the third goal is to refine this improved measure further to enable its reliable integration with surrogate data. This advanced measure, combined with surrogates, will also be applied to an EEG database to validate its applicability to real data.

4. **Quantifying neurovascular coupling in a perturbation experiment**: If a complex system can be directly influenced, the underlying interactions can be studied directly with a perturbation experiment. By perturbing one subsystem, analyzing the response of another can detect or quantify couplings. The time series from such an experiment are analyzed as a part of this dissertation. The time series include measurements on patients with severe aortic valve stenosis and a healthy control group. The goal is to compute the visually evoked cerebral blood flow velocity response from transcranial Doppler ultrasonography measurements of the posterior cerebral artery, quantifying neurovascular coupling for each individual in the two groups.

1.4 Hypotheses

This dissertation is based on the following hypotheses:

Hypothesis 1: In an ideal situation of infinite time series length, the value of the coupling strength exactly determines the information flow between subsystems.

Hypothesis 2: The accuracy of the state space approaches for directional coupling detection can be improved with the method of cross-distance vectors, resulting in a smaller probability of a false positive result.

Hypothesis 3: Combining the improved state space measure with surrogate data increases its reliability in inferring the true coupling direction.

Hypothesis 4: The index calculated from time series of a perturbation experiment is able to detect a difference between two groups in a clinical study.

1.5 Scientific Contribution

The contributions of this thesis are the following:

- It is shown that the inverse problem of inferring the coupling strength is solvable, but only in certain scenarios. As it turns out, this is possible when the response subsystem remains in an orbit around the same attractor and does not transition to a different attractor when coupled. Furthermore, it is possible only if it is given that the coupling is either weak enough or strong enough. This provides an important insight into when the comparison of information flow is equivalent to comparing coupling strengths.

- A significant improvement is made to the state space methods for directional coupling detection. The new approach provides insights into the signatures of coupling in the time series of coupled dynamical systems, making it interesting from a theoretical perspective.
- The new approach also increases the applicability to real data, as shown by an analysis of an EEG database of patients with epilepsy. Combining the new state space measure with surrogates better distinguishes between the focal signals (measured from brain areas where the seizure was first detected) and the nonfocal signals (not involved in the seizure onset) than the classical measures, which have previously been used for this purpose. Therefore, the contribution is also in increased applicability of state space methods in clinical applications.
- A perturbation experiment was conducted on patients with severe aortic valve stenosis and on a healthy control group. The contribution lies in demonstrating that computing the visually evoked cerebral blood flow velocity response can effectively distinguish between the aortic stenosis group and the healthy control group, as found by detecting a statistically significant difference.

1.6 Structure of the Thesis

The remainder of the thesis is structured as follows. Chapter 2 first discusses the basic theory of coupled dynamical systems and chaos, followed by the introduction of directional couplings and the concept of synchronization. Chapter 3 discusses the methodology for detecting directional couplings from measured time series. Four families of methods are introduced: Granger causality, phase dynamics methods, information methods, and state space methods. Perturbation experiments are also discussed as an alternative approach.

Following the introduction of the methodology, original research is presented. Chapter 4 studies the information flow between two coupled dynamical systems. Specifically, it considers the solvability of the inverse problem of inferring the coupling strength from bivariate time series. Chapter 5 introduces a new state space method for directional coupling detection, more accurate than the classical state space approaches. Furthermore, an analysis of an EEG dataset is performed. Chapter 6 presents a perturbation experiment in which the strength of a neurovascular coupling was compared between patients with severe aortic stenosis and a healthy control group. Finally, Chapter 7 summarizes the dissertation.

Chapter 2

Directional Couplings in Dynamical Systems

2.1 Dynamical Systems

A dynamical system is a deterministic mathematical prescription for the time evolution of variables [16], [17]. Time can be either a discrete or a continuous variable. The time evolution of a discrete-time dynamical system is described by a prescription for the variable values for the next point in time. A general example of an n-dimensional discrete-time dynamical system X is

$$\begin{aligned} x_1(t+1) =& f_1(x_1(t), x_2(t), \ldots, x_n(t)) \\ x_2(t+1) =& f_2(x_1(t), x_2(t), \ldots, x_n(t)) \\ & \vdots \\ x_n(t+1) =& f_n(x_1(t), x_2(t), \ldots, x_n(t)). \end{aligned} \tag{2.1}$$

The time evolution of a continuous-time dynamical system is described by differential equations. A general example of an n-dimensional continuous-time dynamical system X is

$$\begin{aligned} \frac{dx_1(t)}{dt} =& F_1(x_1(t), x_2(t), \ldots, x_n(t)) \\ \frac{dx_2(t)}{dt} =& F_2(x_1(t), x_2(t), \ldots, x_n(t)) \\ & \vdots \\ \frac{dx_n(t)}{dt} =& F_n(x_1(t), x_2(t), \ldots, x_n(t)). \end{aligned} \tag{2.2}$$

This dissertation focuses on continuous-time systems, as they are generally more representative of real systems. The equations (2.2) can be rewritten in vector form as

$$\frac{d\boldsymbol{x}(t)}{dt} = \boldsymbol{F}(\boldsymbol{x}(t)). \tag{2.3}$$

Throughout the dissertation, bold notation represents vector values. The n-dimensional space of all possible states with coordinates $\boldsymbol{x} = (x_1, x_2, \ldots, x_n)$ is called the *state space* (also the *phase space*). Given an initial condition $\boldsymbol{x}(t_0)$, the solution at a later time $\boldsymbol{x}(t)$ is uniquely determined by the time evolution (2.3). The collection of solutions for all times t is called a *trajectory* in the state space.

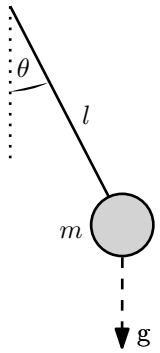

Figure 2.1: Diagram of the pendulum system described by equation (2.4).

Consider a simple example of a pendulum, depicted in Figure 2.1. It consists of a mass attached to a massless rod of length l in a gravitational field g. Let θ be the angle between the orientation of the rod and the gravitational field. The time evolution of θ is determined by

$$\frac{d^2\theta}{dt^2} = -\frac{g}{l}\sin\theta. \tag{2.4}$$

The equation can be transformed into the form (2.2) by setting $\frac{d\theta}{dt} = \eta$, resulting in two first-order equations. In the limit of small angles, the approximation $\sin(\theta) \approx \theta$ results in a harmonic oscillator. Otherwise, we can use a numerical integrator to obtain the approximate solutions. Throughout this dissertation, the Runge-Kutta integrator of fourth order with a constant step [18] is used to obtain numerical solutions of all considered systems.

Three exemplary solutions are shown in Figure 2.2 (a). When the pendulum's energy is small, the angle θ is bounded. When energy is large enough, the pendulum starts rotating, and θ escapes above π. However, its dynamics are still very simple and, more importantly, predictable. Figure 2.2 (b) shows a collection of orbits in the state space $(\theta, \frac{d\theta}{dt})$, called the *phase portrait*. Plots in state space can be useful to understand the behavior of a system. For instance, observing the pendulum's phase portrait makes it clear that the coordinate θ of systems with large enough energy is not bounded.

The systems considered thus far do not explicitly depend on time. Such systems are called autonomous dynamical systems. If there is an explicit time dependence in the time evolution

$$\frac{d\boldsymbol{x}(t)}{dt} = \boldsymbol{F}(\boldsymbol{x}(t), t), \tag{2.5}$$

then the system is called non-autonomous. An example is a pendulum with additional periodic forcing. However, the distinction between autonomous and non-autonomous systems is merely for convenience. An n-dimensional non-autonomous dynamical system is equivalent to an $n+1$-dimensional autonomous system, as evident by defining a new variable x_{n+1} with the time evolution $\frac{dx_{n+1}}{dt} = 1$.

2.2 Chaos in Dynamical Systems

Nonlinear dynamical systems can exhibit chaotic dynamics, characterized by exponential sensitivity to initial conditions [17]. Consider a system X with time evolution $d\boldsymbol{x}(t)/dt = \boldsymbol{F}(\boldsymbol{x}(t))$. Let $\boldsymbol{x}(t)$ be the solution for the initial condition $\boldsymbol{x}(t_0)$ and let $\tilde{\boldsymbol{x}}(t)$ be the solution for the initial condition $\tilde{\boldsymbol{x}}(t_0) = \boldsymbol{x}(t_0) + \delta\boldsymbol{x}(t_0)$, where $|\delta\boldsymbol{x}(t_0)|$ is infinitesimally small.

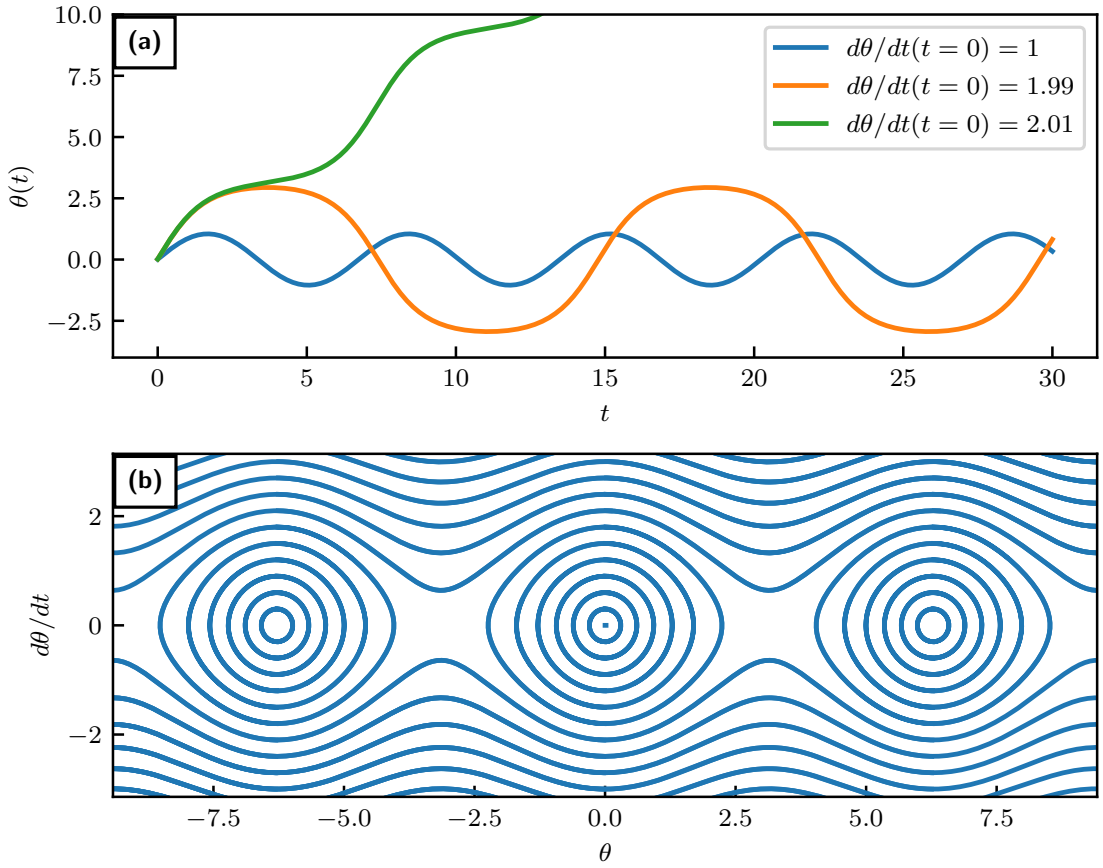

Figure 2.2: (a) Three solutions to the pendulum equation (2.4) with $g = l = 1$ for three different initial conditions (first component is $\theta(t = 0) = 0$ for all three cases), and (b) the phase portrait of the pendulum system.

Here, $|\cdot|$ denotes the Euclidean norm. The time evolution of the displacement vector $\delta\boldsymbol{x}(t) = \tilde{\boldsymbol{x}}(t) - \boldsymbol{x}(t)$ is thus given by

$$\frac{d(\delta\boldsymbol{x})(t)}{dt} = \boldsymbol{J}\delta\boldsymbol{x}(t), \tag{2.6}$$

where $\boldsymbol{J}$ is the Jacobi matrix of $\boldsymbol{F}$. For chaotic systems, the norm of the displacement vector increases exponentially with time

$$|\delta\boldsymbol{x}(t)| = |\delta\boldsymbol{x}(t_0)|e^{\lambda(\boldsymbol{x}(t_0),\delta\boldsymbol{x}(t_0))t}. \tag{2.7}$$

The exponent $\lambda(\boldsymbol{x}(t_0), \delta\boldsymbol{x}(t_0))$ is called the *Lyapunov exponent* for initial condition $\boldsymbol{x}(t_0)$ and initial displacement $\delta\boldsymbol{x}(t_0)$. If it is positive, then the system is said to be chaotic.

More generally, an n-dimensional system has n Lyapunov exponents for an initial condition $\boldsymbol{x}(t_0)$, depending on the orientation of the initial displacement $\delta\boldsymbol{x}(t_0)$. Integrating equation (2.6) over time takes initial displacement vector $\delta\boldsymbol{x}(t_0)$ to a displacement at a later time $\delta\boldsymbol{x}(t)$, which can be considered a map $M(\boldsymbol{x}(t_0), t)$ so that $\delta\boldsymbol{x}(t) = M(\boldsymbol{x}(t_0), t)\delta\boldsymbol{x}(t_0)$. The Lyapunov exponents $\lambda_1, \lambda_2, \ldots, \lambda_n$ are defined as the logarithm of the eigenvalues of the matrix

$$\Lambda = \lim_{t\to\infty} \frac{1}{2t}(M(\boldsymbol{x}(t_0), t)M^T(\boldsymbol{x}(t_0), t)). \tag{2.8}$$

Each Lyapunov exponent λ_i determines how a small displacement in a characteristic direction (the direction in the corresponding eigenvector) either expands when $\lambda_i > 0$ or shrinks when $\lambda_i < 0$.

The maximal Lyapunov exponent is of most importance. Chaos is defined as exponential sensitivity to initial conditions, which corresponds to a positive maximal Lyapunov exponent $\lambda_{max} > 0$. In practice, a chosen random displacement almost always consists of all characteristic directions, and over a long time period, the displacement changes exponentially according to the maximal Lyapunov exponent.

For continuous-time dynamical systems, chaos is possible for $n \geq 3$ dimensions. For non-autonomous continuous-time dynamical systems, chaos is possible for $n \geq 2$ dimensions because time can be considered an additional dimension, as shown in Chapter 2.1. Such an example is the Duffing system, considered in Chapter 4.

The Rössler system [19] is a commonly studied system that exhibits chaotic dynamics. It is a three-dimensional system described by

$$\begin{aligned} \frac{dx_1}{dt} &= -x_2 - x_3 \\ \frac{dx_2}{dt} &= x_1 + ax_2 \\ \frac{dx_3}{dt} &= b + x_3(x_1 - c), \end{aligned} \tag{2.9}$$

where a, b and c are parameters. Although this system of equations is rather simple, the solutions can exhibit rich, chaotic dynamics because of the nonlinear term. An example of a numerically obtained solution is shown in Figure 2.3 (a). A clearer display of the solution can be obtained by plotting it in the three-dimensional state space, which is seen in Figure 2.3 (b). Here, one can see that the solution seems to form a structure called the system's *attractor*. It is the part of the state space the orbit tends towards as time increases, much like the limit cycles of simpler periodic systems [20].

In order to illustrate the Rössler system's exponential sensitivity to initial conditions, let us evolve two trajectories with close initial conditions in time. The first solution has the initial condition $\boldsymbol{x}(t_0)$ which is a point on the Rössler attractor. The second solution has the initial condition $\boldsymbol{x}(t_0) + \delta\boldsymbol{x}(t_0)$, where the displacement has the norm $|\delta\boldsymbol{x}(t_0)| = 10^{-14}$ and has a random orientation. Figure 2.4 (a) shows the time evolution of the first component of the two solutions. At approximately $t \approx 370$, the solutions become visibly different. More information can be gained by observing the time evolution of the displacement norm $|\delta\boldsymbol{x}(t)|$, shown in Figure 2.4 (b). For a large part, it increases linearly on the logarithmic scale. This indicates that the Rössler system (2.3) is indeed chaotic, and the slope determines the largest Lyapunov exponent. It can be roughly approximated by

$$\lambda_{max} \approx \frac{1}{t_1 - t_0} \ln\Big(\frac{|\delta\boldsymbol{x}(t_1)|}{|\delta\boldsymbol{x}(t_0)|}\Big), \tag{2.10}$$

where t_1 is the time when the displacement norm reaches a plateau. This results in $\lambda_{max} \approx 0.09$.

Note that this is a very rough approximation. A more rigorous algorithm to compute all n Lyapunov exponents of an n-dimensional system was proposed by Benettin, Galgani, Giorgilli, *et al.* [21]. It consists of repeatedly evolving n displacement vectors forward in time and performing the Gram-Schmidt orthogonalization every couple of time steps. However, the main idea is similar to the example above.

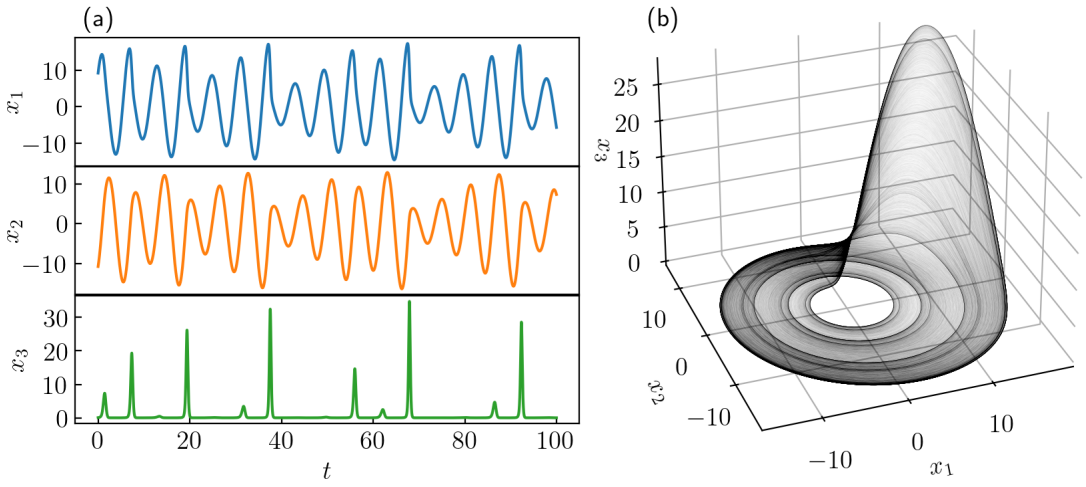

Figure 2.3: A numerical solution of the Rössler system (2.9) with parameters $a = 0.15$, $b = 0.2$, $c = 10$ and random initial conditions. (a) shows the time evolution of all three components, and (b) shows the numerical solution in the three-dimensional state space (x_1, x_2, x_3). The numerical solution was obtained using a Runge-Kutta integrator of fourth order with a time step $\Delta t = 0.01$. First, 10^4 samples were discarded to avoid transients, i.e., for the solution to be on the attractor.

2.3 Coupling of Two Systems

Consider two dynamical systems X and Y described by

$$\begin{aligned} \frac{d\boldsymbol{x}}{dt} &= \boldsymbol{F}_X(\boldsymbol{x}) \\ \frac{d\boldsymbol{y}}{dt} &= \boldsymbol{F}_Y(\boldsymbol{y}). \end{aligned} \tag{2.11}$$

These systems are isolated from each other since the time evolution of X does not depend on the state of Y, and vice versa. If the systems are coupled, their time evolution has additional terms

$$\begin{aligned} \frac{d\boldsymbol{x}}{dt} &= \boldsymbol{F}_X(\boldsymbol{x}) + \boldsymbol{G}_X(\boldsymbol{x}, \boldsymbol{y}) \\ \frac{d\boldsymbol{y}}{dt} &= \boldsymbol{F}_Y(\boldsymbol{y}) + \boldsymbol{G}_Y(\boldsymbol{y}, \boldsymbol{x}). \end{aligned} \tag{2.12}$$

The first terms $\boldsymbol{F}_X, \boldsymbol{F}_Y$ describe isolated dynamics, and the second terms $\boldsymbol{G}_X, \boldsymbol{G}_Y$ are coupling functions [22] that describe interactions. For convenience, X and Y are sometimes referred to as subsystems to differentiate them from the complete system they form. Let us define the central concept of the *direction of coupling*. We have four possibilities:

1. If $\boldsymbol{G}_X = 0$ and $\boldsymbol{G}_Y = 0$, we have independent systems
2. If $\boldsymbol{G}_X \neq 0$ and $\boldsymbol{G}_Y = 0$, we have unidirectional coupling where X (the response subsystem) depends on Y (the driving subsystem), denoted by $Y \to X$
3. If $\boldsymbol{G}_X = 0$ and $\boldsymbol{G}_Y \neq 0$, we have unidirectional coupling where Y (the response subsystem) depends on X (the driving subsystem), denoted by $X \to Y$

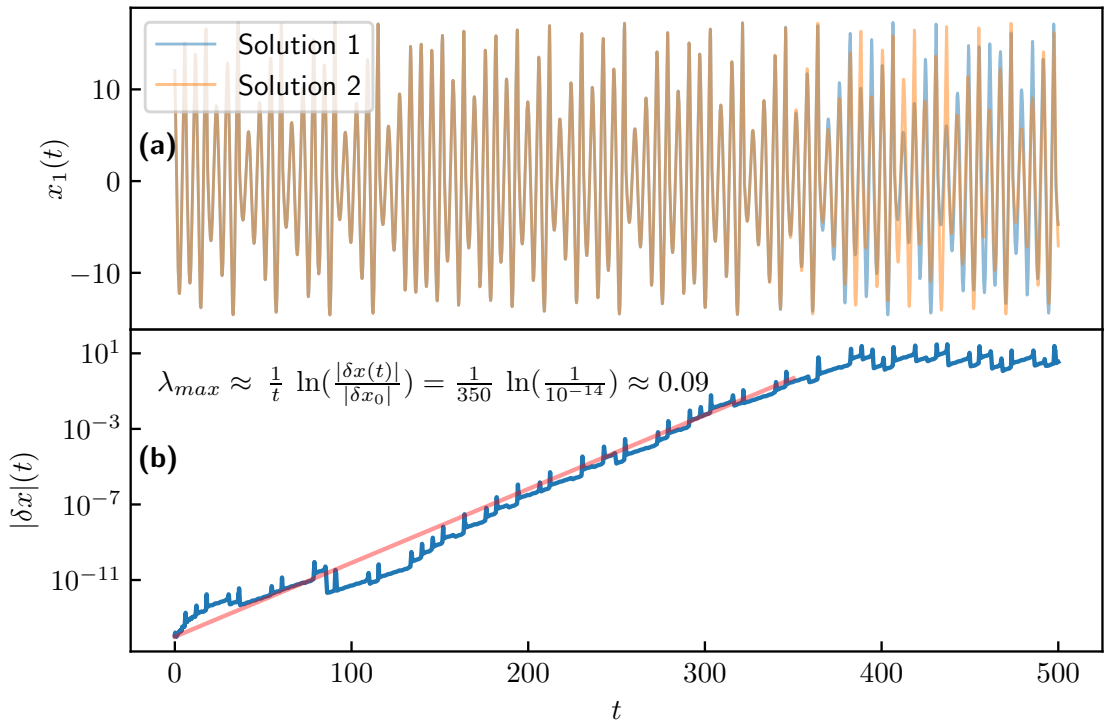

Figure 2.4: (a) The time evolution of the first component of the Rössler system for two slightly displaced initial conditions, and (b) the time evolution of the norm of the displacement vector $|\delta \boldsymbol{x}(t)|$.

4. If $\boldsymbol{G}_X \neq 0$ and $\boldsymbol{G}_Y \neq 0$, we have bidirectional coupling where X and Y mutually interact, denoted by $X \longleftrightarrow Y$

The coupling functions are often written in the form $\boldsymbol{G}(\boldsymbol{x}, \boldsymbol{y}) = \varepsilon \tilde{\boldsymbol{G}}(\boldsymbol{x}, \boldsymbol{y})$. Here, ε is the *coupling strength*. Although ε and $\tilde{\boldsymbol{G}}(\boldsymbol{x}, \boldsymbol{y})$ are not uniquely determined by $\boldsymbol{G}(\boldsymbol{x}, \boldsymbol{y})$, the distinction is often very useful.

Consider the example of two identical Rössler systems (2.9) X and Y with a unidirectional coupling $Y \to X$. They are described by

$$\begin{aligned}
\frac{dx_1}{dt} &= -x_2 - x_3 + \varepsilon(y_1 - x_1) \\
\frac{dx_2}{dt} &= x_1 + 0.15x_2 \\
\frac{dx_3}{dt} &= 0.2 + x_3(x_1 - 10) \\
\frac{dy_1}{dt} &= -y_2 - y_3 \\
\frac{dy_2}{dt} &= y_1 + 0.15y_2 \\
\frac{dy_3}{dt} &= 0.2 + y_3(y_1 - 10)
\end{aligned} \tag{2.13}$$

Here the coupling functions are $\boldsymbol{G}_Y(\boldsymbol{y}, \boldsymbol{x}) = (0, 0, 0)$ and $\boldsymbol{G}_X(\boldsymbol{x}, \boldsymbol{y}) = (\varepsilon(y_1 - x_1), 0, 0)$. Coupling of this form is called diffusive coupling. It forces the values of one variable

towards the values of another. In the limit of large ε (strong coupling), variables coupled in this way will be nearly identical. Figure 2.5 shows numerical solutions to (2.13) for different coupling strengths ε. When $\varepsilon = 0$, the two Rössler systems are independent. By increasing ε, the coupled variables x_1 and y_1 are becoming increasingly similar. When ε is large enough, the subsystems become completely identical. This brings us to the concept of synchronization.

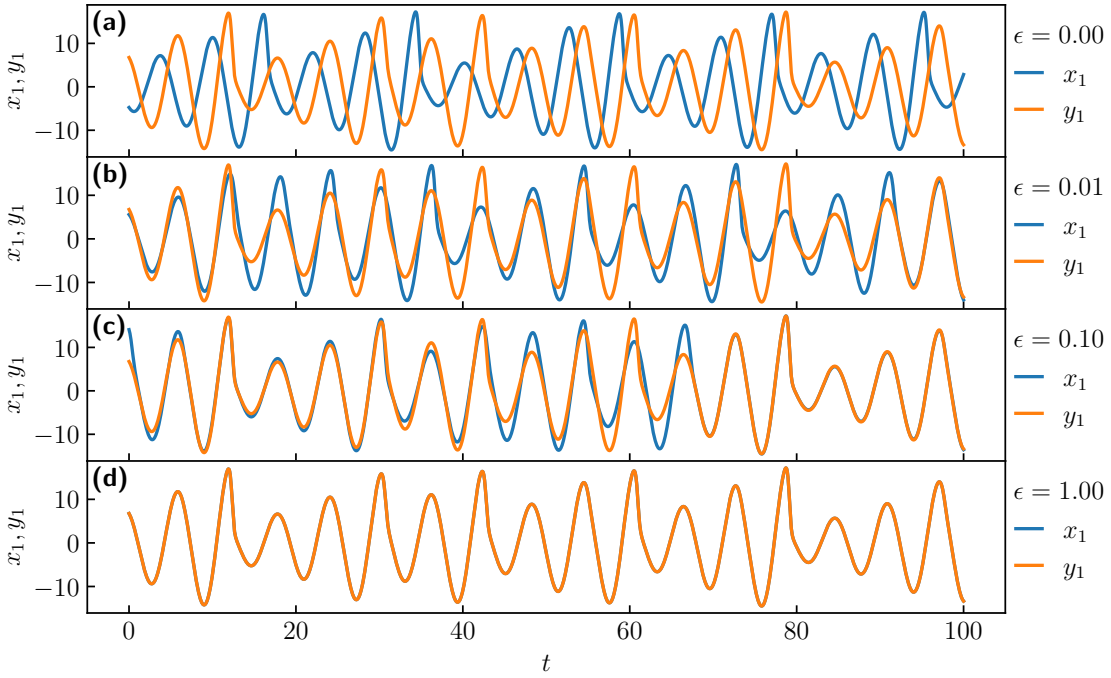

Figure 2.5: The components x_1 and y_1 of the numerical solutions to the coupled Rössler systems (2.13) for four values of the coupling strength ε, increasing from (a) to (d). Initial conditions are the same for all four cases. The integration step is $\Delta t = 0.01$, and the first 10^4 samples were discarded to avoid transients.

2.4 Synchronization of Chaos

When the coupling between two oscillatory systems is strong enough, the systems can *synchronize* [20]. Synchronization is characterized by common dynamical properties between systems, such as common oscillation frequencies. Two systems can oscillate with different frequencies when isolated from each other but begin oscillating in unison once a coupling is introduced. Synchronization was first described in the 17th century by the Dutch scientist Christiaan Huygens, who observed the synchronization of two pendulum clocks. More recently, the concept of synchronization has been described in chaotic systems. Three main types of synchronization of chaos are complete synchronization, phase synchronization, and generalized synchronization.

2.4.1 Complete synchronization

The simplest type of synchronization of chaos is *complete synchronization*. It occurs when two subsystems begin evolving under different initial conditions, but their trajectories eventually become identical. Such synchronization is only possible for identical subsystems.

Consider two identical dynamical systems X and Y with a diffusive coupling in their first components

$$\frac{d\boldsymbol{x}}{dt} = \boldsymbol{F}(\boldsymbol{x}) + (\varepsilon(y_1 - x_1), 0, \ldots, 0) \tag{2.14}$$

$$\frac{d\boldsymbol{y}}{dt} = \boldsymbol{F}(\boldsymbol{y}). \tag{2.15}$$

The trajectory of X tends towards that of Y. When the coupling is sufficiently strong, the trajectories can become identical. This occurs because at the moment the states of both subsystems match $\boldsymbol{x}(t_1) = \boldsymbol{y}(t_1)$, the coupling function becomes zero $\varepsilon(y_1(t_1) - x_1(t_1)) = 0$. From that point onward, the systems evolve according to their isolated dynamics, which are the same for both $\boldsymbol{F}(\boldsymbol{x}(t_1)) = \boldsymbol{F}(\boldsymbol{y}(t_1))$. The trajectories are therefore identical for all future times $\boldsymbol{x}(t) = \boldsymbol{y}(t)$. This is known as complete synchronization.

Note that the coupled Rössler systems (2.13) is an example of such dynamics. In the case of strong coupling, shown in Figure 2.5 (d), the states of the Rössler systems are identical $\boldsymbol{x}(t) = \boldsymbol{y}(t)$. Again, this is only possible because the parameters a, b, and c from (2.9) are identical for both subsystems, as seen in equation (2.13). The two dynamics cannot become identical when the parameters are not identical, making complete synchronization impossible. However, phase synchronization and generalized synchronization can still occur in such cases.

2.4.2 Phase synchronization

Oscillating systems can often be described in terms of their *amplitude* and *phase* [20]. This is typically possible when a system's trajectory circles around a point in state space. Note that the word phase has a different meaning in the contexts of phase space and phase of oscillators. Phase ϕ increases monotonically with time and increases by 2π every oscillation. Defining a phase is mostly straightforward for periodic systems, as a recurrence marks one well-defined oscillation and the increase of phase by 2π. For example, for a periodic trajectory of the pendulum (2.4) (the closed orbits in Figure 2.2), defining a phase is trivial in the $(\theta, d\theta/dt)$ space. Defining the phase of chaotic oscillators is, however, not as straightforward and not always possible. Still, for many systems, a well-defined phase can be determined. Take, for example, the Rössler system (2.9). Looking at Figure 2.3 (b), we see that the projection of the trajectory to the (x_1, x_2) plane circles around the point $(0, 0)$. The phase can therefore be defined as $\phi = \arctan(x_2/x_1)$, and the amplitude as $A = \sqrt{x_1^2 + x_2^2}$ [23].

Furthermore, phase can be extracted from time series numerically. A notable method for numerical phase extraction is the Hilbert transform [20]. It requires a single dominant frequency in order to provide a monotonically increasing phase. If there are multiple dominant peaks, one can use the short-time Fourier transform or the complex wavelet transform [24], which are time-frequency transformations. They provide information about instantaneous amplitudes and instantaneous phases at different frequencies.

The existence of a phase in coupled systems X and Y can lead to *phase synchronization* even in non-identical systems [25]. Formally, it is defined as the condition that

$$|m\phi_X(t) - n\phi_Y(t)| < C \quad \text{where} \quad m, n \in \mathbb{N} \tag{2.16}$$

holds for all times t (after possible transients), where C is a constant. This condition means that the phases of the two coupled oscillators are locked in an $m : n$ ratio. In the time it takes the system X to make n oscillations, the system Y makes exactly m. The simplest case is a $1 : 1$ ratio, where the coupling results in identical frequencies of X and Y, even if they are not identical when the systems are isolated.

2.4.3 Generalized synchronization

The third type of synchronization considered here is *generalized synchronization* [26], [27]. Its onset does not require identical subsystems or a well-defined phase. Consider two unidirectionally coupled subsystems X and Y with time evolution

$$\begin{aligned} \frac{d\boldsymbol{x}}{dt} &= \boldsymbol{F}_X(\boldsymbol{x}) + \boldsymbol{G}_X(\boldsymbol{x}, \boldsymbol{y}) \\ \frac{d\boldsymbol{y}}{dt} &= \boldsymbol{F}_Y(\boldsymbol{y}). \end{aligned} \tag{2.17}$$

Generalized synchronization occurs when the state of the response subsystem X is completely determined by the state of the driving subsystem Y

$$\boldsymbol{x}(t) = \boldsymbol{\psi}(\boldsymbol{y}(t)), \tag{2.18}$$

where $\boldsymbol{\psi}$ is a time-independent function. One could say the response loses its identity and can no longer be considered a separate subsystem from the driver. Complete synchronization is a special case of generalized synchronization where $\boldsymbol{\psi}$ is the identity.

Detecting generalized synchronization numerically is not as straightforward as detecting complete synchronization or phase synchronization. A method based on the closeness of states is briefly discussed in Chapter 3.5.2. Other methods include the conditional Lyapunov exponents [28] and the auxiliary system approach [29]. The latter is especially practical due to its simple implementation.

Chapter 3

Inferring the Direction of Coupling from Time Series

When it comes to complex systems found in nature, how or even if the subsystems interact is often unknown. This raises the question about the direction and strength of possible interactions. Consider two systems, X and Y. If we cannot directly influence these systems, we can only characterize them by measuring their time series. Thus, three central questions arise in the study of time series of possibly interacting complex systems:

1. Can we know, based on the time series, whether or not the systems are coupled?

2. Can we infer the direction of coupling?

3. Can we quantify the strength of coupling?

In many cases, the answer to all three questions is affirmative. Generally couplings are easier to detect if they are strong. However, if they are strong enough to result in the synchronization of subsystems, the coupling direction can no longer be reliably inferred. This is because synchronized systems cannot be considered as two separate subsystems but only as one larger system. For weak couplings that do not result in synchronization, coupling strength, as well as coupling direction, can often be inferred from measured time series.

Historically, linear cross-correlation is perhaps the most commonly used approach to detect connections between dynamical variables. However, it has significant limitations. It can only detect linear dependencies between variables, not nonlinear relationships. Additionally, linear cross-correlation cannot determine the direction of coupling. Therefore, other numerical methods capable of detecting *directional couplings* not only in linear systems but also in *nonlinear dynamics*, which may be chaotic, are needed. Various such methods based on different principles have been developed.

This chapter discusses four of the most prominent families of methods for directional coupling detection, namely Granger causality methods, phase dynamics methods, information methods, and state space methods. The former two are considered only briefly in order to give a more complete overview of the methodology but will not be used further in this dissertation. The latter two are discussed in greater detail, as they are the subject of Chapter 4 and Chapter 5, which present original research on these methods. This chapter also introduces the concept of surrogate data, and the concept of perturbation experiments, which is an alternative approach to inferring interactions.

3.1 Time Series of Dynamical Systems

Systems found in nature can be measured, resulting in time series. A measurement captures the state of a system X at equally spaced times $t_i = t_0 + i\Delta t$, where $i = 1, 2, \ldots, N$. Usually, only one component, or more generally a one-dimensional function ξ of all the components $x(t_i) = \xi(x_1(t_i), x_2(t_i), \ldots, x_n(t_i))$ is measured, which results in a one-dimensional time series $(x(t_i), i = 1, 2, \ldots, N)$ of length N. In what follows, a time series is often denoted as $x(t_i)$ for simplicity. This should not lead to confusion with its components at times t_i as the context will make the intended meaning clear.

The reduction to one dimension, a consequence of measurement, is often not sufficient for analyzing a dynamical system. Fortunately, the dynamics can, in principle, be reconstructed with the Takens' delay embedding [30]. One can define a new multidimensional variable $\tilde{\boldsymbol{x}}$, which at time t_i has values

$$\tilde{\boldsymbol{x}}(t_i) = (x(t_i), x(t_{i+\tau}), \ldots, x(t_{i+(m-1)\tau})) \tag{3.1}$$

where m is the embedding dimension and τ is the time delay. The Takens' embedding theorem states that if $m > 2d$, where d is the dimension of the system's attractor, the dynamics of the embedded vectors are equivalent to the true dynamics of the full system. This is a formal upper bound for m, and a smaller m is often sufficient. In practice, the choice of τ is also important and is usually taken to be around one-tenth to one-half of the mean orbital period around the attractor [31].

In what follows, bivariate time series are considered and represented as two one-dimensional time series $x(t_i)$ and $y(t_i)$. They are always sampled at identical, equally spaced times and have the same length. This assumption is necessary for the methodology presented in this chapter.

3.2 Granger Causality

Clive Granger proposed the first framework for detecting directional couplings from measured time series in 1969 [2]. It is based on the Wiener's principle of observational causality [32]. It states that *for two simultaneously observed processes X, Y, we call Y causal to X if knowledge about the past of Y improves our prediction of X over and above what is predictable from the past of X alone.* Granger put Wiener's definition into practice and developed a statistical test for determining whether a variable Y helps forecast another variable X. Specifically, he tested for whether the past of Y contains unique information about the future of X that is not contained in the past of X. If that turns out to be the case, then Y causes X. For this purpose, Granger proposed to construct the linear vector autoregressive models

$$M_R^X(t_{i+1}) = A + \sum_{j=0}^{k} B_j x(t_{i-j}), \tag{3.2}$$

$$M_F^X(t_{i+1}) = C + \sum_{j=0}^{k} D_j x(t_{i-j}) + \sum_{j=0}^{k} E_j y(t_{i-j}), \tag{3.3}$$

where k is the maximal time lag, and A, C and $B_j, D_j, E_j, j = 0, \ldots, k$ are real constants determined by minimizing the errors between each of the two models and the original time series. For instance, one can minimize the mean square errors $\mathrm{MSE}(M_R^X(t_i), x(t_i))$ and $\mathrm{MSE}(M_F^X(t_i), x(t_i))$. Note that $M_F^X(t_i)$ is the full model that depends on the past of both X and Y, and $M_R^X(t_i)$ is the reduced model that only depends on the past of

X. If the resulting mean square error of the extended model is significantly smaller than that of the reduced model $\mathrm{MSE}(M_F^X(t_i), x(t_i)) < \mathrm{MSE}(M_R^X(t_i), x(t_i))$, then Y is said to Granger-cause X. In other words, it means a directional coupling $Y \to X$ is detected. The significance is assessed by, for example, the F-test [33]. Accordingly, a coupling $X \to Y$ can be detected by swapping the roles of X and Y and constructing the models M_F^Y and M_R^Y in the same manner as M_F^X and M_R^X.

Granger causality is a popular choice due to its simple implementation. Its applications range from economics [3] and finance [34] to meteorology [14] and enviromental science [15]. However, it has its limitations. The linear model does not capture possible nonlinear dynamics within the subsystems X and Y or nonlinear interactions between them. Nonlinear extensions to Granger causality have been proposed by including nonlinear terms to the models (3.2) and (3.3) [33]. They can detect linear couplings in nonlinear systems as well as nonlinear couplings. However, such methods are more challenging to implement and still assume a specific model. Other methods that operate on different principles have been proposed to account for these drawbacks.

3.3 Phase Dynamics Methods

Computing the phases of interacting systems can be used to detect couplings. For the definition of phase, see Chapter 2.4.2. Let $\phi_X(t_i)$ and $\phi_Y(t_i)$ be the time series of the phases extracted from signals $x(t_i)$ and $y(t_i)$, respectively. If the coupling between systems results in phase synchronization, then one can detect a $m : n$ phase lock (2.16) by observing the absolute difference

$$\Delta\phi_{m,n}(t_i) = |m\phi_X(t_i) - n\phi_Y(t_i)|. \tag{3.4}$$

If this difference is bounded for all times, then the phases are in an $m : n$ lock. However, the absolute phase difference will have a positive drift if the coupling is not strong enough to result in phase synchronization. In order to detect weaker couplings, one can compute the phase coherence [35] defined as

$$\Pi_{m,n} = \Big| \frac{1}{N} \sum_{i=1}^{N} e^{i(m\phi_X(t_i) - n\phi_Y(t_i))} \Big|. \tag{3.5}$$

If there is an $m : n$ phase lock, then $\Pi_{m,n}$ will be close to one. Conversely, if there is no $m : n$ lock, it will be close to zero. When the coupling is not so strong as to result in phase synchronization for all times, there can still be short time windows where phases evolve in an $m : n$ ratio. This results in intermediate values of phase coherence. In other words, the expression (3.5) results in values that increase from 0 to 1 as the coupling strength increases. Thus, phase coherence can be used to quantify the coupling strength.

In practice, one can compute the phase coherence for various m and n to search for different phase locks. However, the ability to detect them rapidly diminishes as m and n increase. Although implementing phase coherence is fairly simple, it cannot determine the direction of coupling.

A phase dynamics method introduced to detect specifically the direction of coupling was proposed by Rosenblum and Pikovsky [36]. To detect a coupling from Y to X, first consider the time evolution of the increments of the phase $\Delta_X(k) = \phi_X(t_k + \tau) - \phi_X(t_k)$ for a set time lag τ. These increments can be considered as generated by a noisy map $\Delta_X(k) = F_X(\phi_X(t_k), \phi_Y(t_k))$. Next, one performs a regression of a Fourier series $F_X = \sum_{m,n} A_{m,n} e^{i(m\phi_X + n\phi_Y)}$, where m and n are indices that span all frequencies. Here, the idea becomes apparent. If X is influenced by Y, then some of the constants $A_{m,n}$ with

$n \neq 0$ will be nonzero. In order to quantify the overall coupling strength in the direction $Y \to X$, one computes

$$c_X = \int_0^{2\pi} \int_0^{2\pi} \left(\frac{\partial F_X}{\partial \phi_Y}\right)^2 d\phi_X d\phi_Y. \tag{3.6}$$

Conversely, the coupling $X \to Y$ is quantified by c_Y, which is obtained by swapping X and Y in (3.6) and in all quantities used within. The direction of coupling can thus be determined by comparing the values c_X and c_Y.

The phase methods rely on well-defined phases of the analyzed systems. Notable fields of application include astrophysics [37], medicine [7], and neuroscience [11].

3.4 Information Theory Methods

The third family of methods is based on information theory. These methods do not require a meaningful definition of phase and do not assume a model. Therefore, they are quite general and can detect both linear and nonlinear couplings between linear or nonlinear systems.

Following the idea of Granger causality, one can put Wiener's definition of causality into the framework of information theory: *how much additional information does the past state of Y contain about the future observation of a value of X given that we already know the past state of X?* This can be put into practice, as information is mathematically well-defined and can be estimated from measured time series. This section presents the basic concepts of information theory, followed by the introduction of transfer entropy as the most prominent information theory method for directional coupling detection.

3.4.1 Entropy and information

In the framework of probabilities, the notion of information is a well-defined quantity. If an event e_1 has a large probability of occurring, for example, $p(e_1) = 0.99$, observing this event gives us a small amount of information. If another event e_2 has a small probability of occurring, for example, $p(e_2) = 0.01$, observing it gives us a large amount of information. Mathematically, information of an event e is defined as $I(e) = -\log(p(e))$. The logarithm's base is not important, as it only changes the units. For example, base-2 yields the *bit* as the unit of information, and base-e yields the *nat*.

Note that in this section, the notation X is used to denote random variables rather than dynamical systems. This is specific to this section and should not lead to confusion.

Information can be used to characterize random variables and the relationships between them. The central quantity of this section is the *Shannon entropy* [38], which quantifies the average amount of information given by an outcome of a random variable. In this context, average refers to the average taken across realizations. Let X be a random variable with a probability distribution $p_X(x)$. The Shannon entropy of X is defined as

$$H(X) = -\sum_x p_X(x) \log p_X(x), \tag{3.7}$$

where the sum includes all possible values of X. Shannon entropy can be considered quantifying the expected "surprise" of an outcome of a trial. For example, if X can only take one possible value $p_X(0) = 1$, the outcome of a trial is certain, and the entropy equals zero. If X has two possible values, its entropy will be the largest if both are equally probable. The *joint entropy* of two random variables X and Y with a joint probability distribution $p_{X,Y}(x, y)$ is defined as

$$H(X, Y) = -\sum_{x,y} p_{X,Y}(x, y) \log p_{X,Y}(x, y). \tag{3.8}$$

The meaning of the joint entropy is similar to the entropy $H(X)$, as the variables X and Y can be considered a vector-valued random variable $\tilde{X}$, which makes the joint entropy equivalent to $H(\tilde{X})$. The *conditional entropy* of X given Y is defined as

$$H(X|Y) = -\sum_{x,y} p_{X,Y}(x,y) \log p_{X|Y}(x|y). \tag{3.9}$$

It quantifies the expected surprise of an outcome of X in a trial, given that the outcome of Y in that same trial is already known. To grasp the meaning of this quantity, consider two extreme examples. If $X = Y$, then $H(X|Y) = 0$ because there will be no surprise (or no additional information gained) when looking at the result of X, having already looked at Y. If X and Y are statistically independent, i.e., if $p_{X,Y}(x,y) = p_X(x)p_Y(y)$, then the conditional entropy is $H(X|Y) = H(X)$, since knowing an outcome of Y tells us nothing about X.

Next, we have the *relative entropy*, also called the *Kullback-Leibler divergence*

$$D(p_X || p_Y) = \sum_x p_X(x) \log \Big(\frac{p_X(x)}{p_Y(x)} \Big). \tag{3.10}$$

It can be considered quantifying how much two probability distributions differ, but it is not actually a measure of distance as it is not symmetric in p_X and p_Y. It is equal to zero if $p_X(x) = p_Y(x)$ and is infinite if there is an x such that $p_X(x) > 0$ and $p_Y(x) = 0$.

Finally, we have the *mutual information* of two random variables

$$I(X,Y) = H(X) + H(Y) - H(X,Y). \tag{3.11}$$

It quantifies the average amount of common information contained in two random variables X and Y. If they are statistically independent, then $H(X,Y) = H(X) + H(Y)$, which gives $I(X,Y) = 0$. In the other extreme when $X = Y$, we have $H(X) = H(Y) = H(X,Y)$ and therefore $I(X,X) = H(X) + H(X) - H(X) = H(X)$ is maximal. Combining mutual information (3.11) and conditional entropy (3.9) gives us *conditional mutual information (CMI)*

$$I(X,Y|Z) = H(X|Z) + H(Y|Z) - H(X,Y|Z). \tag{3.12}$$

It quantifies the average amount of common information contained in X and Y given the value of Z. This is the central quantity used for detecting directional couplings. A diagram representing relationships between the CMI and different entropies and informations is shown in Figure 3.1.

3.4.2 Transfer entropy

Although the definitions of entropy and information are rooted in probability theory, they are also applicable to dynamical systems. Consider a realization of a dynamical system X and its time series $x(t_i)$. Let the values of X at time t_i be distributed by some probability distribution. Here, we refer to a distribution across realizations. With a slight abuse of notation, we denote it by $p(x_i)$. If we assume the system is ergodic [39], the averaging over time is equal to the averaging over states, and thus $p(x_i) = p(x_j)$ for all i, j. In order to incorporate information about the dynamical structure, we consider the joint probability distribution of the states of X at two different times $p(x_i, x_{i+k})$. Although both marginal distributions are identical, the joint distribution depends on the time lag k and contains information about the dynamics. This notion allows for the expression of Markov properties central to defining transfer entropy.

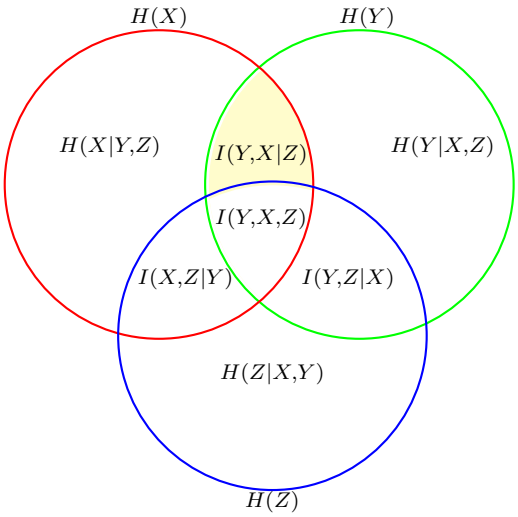

Figure 3.1: A diagram representing the relationships between the CMI $I(X, Y|Z)$ and the different entropies and informations.

Transfer entropy was proposed as an asymmetric measure of information transfer by Schreiber [40]. Assume that X and Y can be approximated by a Markov process of order k. If X and Y are independent, then the following generalized Markov property holds

$$p(x_{i+1}|x_i^{(k)}) = p(x_{i+1}|x_i^{(k)}, y_i^{(l)}), \tag{3.13}$$

where $x_i^{(k)} = (x_i, x_{i-1}, \ldots, x_{i-k+1})$ and $y_i^{(l)} = (y_i, y_{i-1}, \ldots, y_{i-l+1})$, for all l. Schreiber [40] proposed to quantify the incorrectness of this statement by the Kullback-Leibler divergence (3.10) for conditional probabilities, which results in the *transfer entropy*

$$T_{Y\to X} = \sum p(x_{i+1}, x_i^{(k)}, y_i^{(l)}) \log \frac{p(x_{i+1}|x_i^{(k)}, y_i^{(l)})}{p(x_{i+1}|x_i^{(k)})}. \tag{3.14}$$

Here, the sum goes over possible states of x_{i+1}, and over possible states of all the components of $x_i^{(k)}$ and $y_i^{(l)}$. This measure quantifies the amount of additional information about X contained in the past of Y and can be thought of as information transfer from Y to X. It quantifies the strength of a directional coupling $Y \to X$. Conversely, a directional coupling $X \to Y$ is quantified by $T_{X\to Y}$, which is obtained by swapping the roles of X and Y in equation (3.14) and the quantities that are used within.

A similar idea was considered by Paluš, Komárek, Hrnčíř, *et al.* [8]. They proposed to quantify the information flow from Y to X by the following CMI

$$I_{Y\to X} = I(y_i, x_{i+1}|x_i). \tag{3.15}$$

Surprisingly, it turns out that the expressions for transfer entropy (3.14) and the CMI (3.15) are equivalent $T_{Y\to X} \equiv I_{Y\to X}$, given of course that the dimensions of all the variables match [41]. The transfer entropy is thus actually a CMI. Intuitively, it can be thought of as

$$T_{Y\to X} = I(Y^-, X^+|X-), \tag{3.16}$$

where $+$ represents the future and $-$ the past.

While, in theory, the transfer entropy is well-defined for a wide range of systems, estimating the necessary multidimensional probability distributions poses a significant challenge in practice. This becomes increasingly problematic as the number of dimensions of X and Y increase. Although it is far from trivial, this problem can be at least partially alleviated by an educated choice of CMI estimators [42] and by finding only the relevant past variables for conditioning [43]. Thus, transfer entropy has been successfully applied in various fields, including finance [4], medicine [8], and neuroscience [12].

3.5 State Space Methods

The family of state space methods for directional coupling detection relies on a general *cross-mapping property* of weakly coupled dynamical systems. This property states that if two states of the response subsystem are similar $\boldsymbol{x}(t_i) \approx \boldsymbol{x}(t_j)$, then the corresponding states of the driving subsystem $\boldsymbol{y}(t_i)$ and $\boldsymbol{y}(t_j)$ are more likely also to be similar, but not vice versa [44]. In other words, we can say that the close states of the response are mapped to the close states of the driver. Like the information methods, the state space methods make no assumptions about the underlying dynamics, enabling them to detect both linear and nonlinear couplings between linear or nonlinear systems.

This section first defines the concept of the conditioned nearest neighbors, utilized by all state space methods for directional coupling detection. Then, we discuss how the cross-mapping property naturally came to light during the studies on synchronization and, finally, present the most prominent state space methods for directional coupling detection.

3.5.1 Conditioned nearest neighbors

All the state space methods for directional coupling detection quantify the cross-mapping property by analyzing the conditioned nearest neighbors. Let X and Y be two dynamical systems and $x(t_i)$ and $y(t_i)$ their time series of length N_0. First, we reconstruct the dynamics with the Takens' delay embedding, as discussed in Chapter 3.1. The result is embedding vectors

$$\begin{aligned} \tilde{\boldsymbol{x}}(t_i) &= (x(t_i), x(t_{i+\tau}), \ldots, x(t_{i+(m-1)\tau})) \\ \tilde{\boldsymbol{y}}(t_i) &= (y(t_i), y(t_{i+\tau}), \ldots, y(t_{i+(m-1)\tau})), \end{aligned} \tag{3.17}$$

where m is the embedding dimension and τ is the time delay. This restricts the range of the time index to $i = 1, 2, \ldots, N = N_0 - (m-1)\tau$. Allowing a slight abuse of notation, we denote the embedding vectors at time t_i as $\boldsymbol{x}_i$ and $\boldsymbol{y}_i$. Next, we construct the distance matrix $\boldsymbol{D}^X$ of size $N \times N$ with elements $D^X_{ij} = d(\boldsymbol{x}_i, \boldsymbol{x}_j)$, where d is the Euclidean distance. We then compute the index permutations $P^X_i, i = 1, 2, \ldots, N$ so that the i-th row of $\boldsymbol{D}^X$ is sorted in ascending order under that permutation. Thus, we have N permutations of size N, and $P^X_i(j)$ refers to the j-th of the N elements of the permutation P^X_i.

We carry out the same steps of the analysis for the other subsystem leading from the time series $y(t_i)$ to the distance matrix $\boldsymbol{D}^Y$ and the index permutations $P^Y_i, i = 1, 2, \ldots, N$. We can now introduce the *k-th conditioned nearest neighbor* of $\boldsymbol{y}_i$, defined as $\boldsymbol{y}_{P^X_i(k)}$. The k-th conditioned nearest neighbor of $\boldsymbol{y}_i$ is simply the state of Y at another time t_j, namely $\boldsymbol{y}_j$. The time t_j is determined such that $\boldsymbol{x}_j$ is the k-th nearest neighbor of $\boldsymbol{x}_i$ (here, we refer to the true nearest neighbors, not the conditioned ones).

3.5.2 Cross-mapping of close states in synchronized systems

Having introduced conditioned nearest neighbors, let us discuss how they can be utilized to detect generalized synchronization, as first considered by Rulkov, Sushchik, Tsimring,

et al. [26]. This will lead us to detecting directional couplings. Let X and Y be dynamical systems with a strong unidirectional coupling $Y \to X$. Generalised synchronization occurs when a function $\boldsymbol{\psi}$ exists such that $\boldsymbol{x}(t) = \boldsymbol{\psi}(\boldsymbol{y}(t))$. This means that the state of the driving subsystem completely determines the state of the response subsystem. Rulkov, Sushchik, Tsimring, *et al.* [26] proposed a numerical method to detect synchronization from the time series $x(t_i)$ and $y(t_i)$. The idea is as follows: if $\boldsymbol{\psi}$ is sufficiently nice, then close states of Y (the driver) are mapped to close states of X (the response). One can determine whether systems are synchronized by assessing if this cross-mapping of close states is present in the time series.

This is where the conditioned nearest neighbors are used. If the synchronization condition $\boldsymbol{x}(t) = \boldsymbol{\psi}(\boldsymbol{y}(t))$ holds, then the conditioned nearest neighbors of X are, on average, also true neighbors. In order to detect generalized synchronization numerically, one can compute the conditioned nearest neighbors of each subsystem and assess whether they are also true neighbors [26]. This idea evolved into methods for detecting weak directional couplings that do not lead to synchronization, some of which are presented in the following section.

3.5.3 Cross-mapping of close states in non-synchronized systems

One might be tempted to use the method for detecting generalized synchronization to also detect weak couplings that do not lead to synchronization. Le Van Quyen, Martinerie, Adam, *et al.* [45] gave this interpretation that the close states of the driver are mapped to the close states of the response when a weak coupling is present. However, the opposite holds. *When the coupling is weak, the close states of the response subsystem are more likely than in the absence of coupling to be mapped to the close states of the driving subsystem, but not vice versa* [44], [46]. Thus, the conditioned nearest neighbors of the driver are (more likely) to also be true neighbors. This is shown in an example in Figure 3.2.

Moreover, the probability that the conditioned nearest neighbors of the driver are also true neighbors increases with increased coupling. This provides an asymmetric criterion that can quantify directional coupling strength, used by the state space directional couplings measures [5], [44], [46]–[48]. In what follows, some of these methods are presented.

All state space measures require one first to compute the distance matrices $\boldsymbol{D}^X$ and $\boldsymbol{D}^Y$, and the permutations P_i^X and P_i^Y. Before we proceed, it must be noted that we have to somehow suppress the potential influence of linear autocorrelation. Before computing the permutations, we have to exclude the distances between pairs of points that are close in time because they are automatically also close in space. A simple way to do this is with the Theiler correction [49] by applying a constraint to the considered pairs of time indices $|i - j| > W$, where W is the window size. This, in turn, reduces the effective dimension of the distance matrices and the permutations. This section defines the methodology using the full distance matrices of dimension $N \times N$ for the purpose of simpler notation. The only difference in the definitions would be excluding the elements included in the constraint $|i - j| > W$ from any sums over matrices. In practice, it is crucial to account for this.

Two of the methods discussed in this section also share some of the subsequent steps, in addition to the computation of the distance matrices and the permutations. These are now presented. The permutations and the distance matrices are used to construct the following ordered matrices. The permutation P_i^Y is applied to the i-th row of $\boldsymbol{D}^Y$ across $i = 1, \ldots, N$ resulting in the matrix $\boldsymbol{D}^{Y \to Y}$, where $D_{ij}^{Y \to Y} = D_{i,P_i^Y(j)}^Y$ is the distance from $\boldsymbol{y}_i$ to its j-th nearest neighbor. In analogy, the permutation P_i^X is applied to the i-th row of $\boldsymbol{D}^Y$ across $i = 1, \ldots, N$ resulting in the cross-distance matrix $\boldsymbol{D}^{Y \to X}$, where $D_{ij}^{Y \to X} = D_{i,P_i^X(j)}^Y$ is the distance from $\boldsymbol{y}_i$ to its j-th conditioned nearest neighbor. Analogous procedures are used

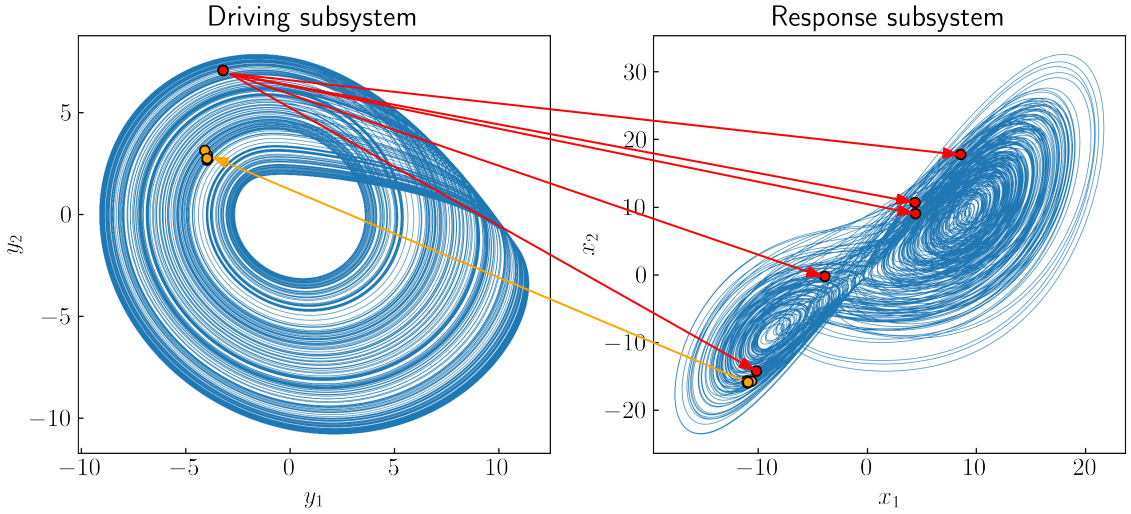

Figure 3.2: An example of the cross-mapping of close states in coupled Rössler systems (2.13). The close states of the response subsystem are mapped to the close states of the driving subsystem (orange dots), but the close states of the driving subsystem are not mapped to the close states of the response subsystem (red dots). Note that this is an actual result of a simulation and not just a schematic drawing.

to determine $\boldsymbol{D}^{X\to X}$ and $\boldsymbol{D}^{X\to Y}$.

3.5.3.1 M measure

The measure $M(Y|X)$ is calculated directly from mean distances [47]. First, the mean distance from $\mathbf{y}_i$ to all other points $\mathbf{y}_j$ is determined by $R_i(Y) = \frac{1}{N}\sum_{j=1}^{N} D_{ij}^{Y}$. The mean distance from $\mathbf{y}_i$ to its k nearest neighbors is given by $R_i^k(Y) = \frac{1}{k}\sum_{j=1}^{k} D_{ij}^{Y\to Y}$, and the mean distance from $\mathbf{y}_i$ to its k conditioned nearest neighbors by $R_i^k(Y|X) = \frac{1}{k}\sum_{j=1}^{k} D_{ij}^{Y\to X}$. Finally, we define

$$M(Y|X) = \frac{1}{N}\sum_{i=1}^{N}\frac{R_i(Y) - R_i^k(Y|X)}{R_i(Y) - R_i^k(Y)}. \tag{3.18}$$

The measure $M(Y|X)$ quantifies the coupling $Y \to X$, and the measure $M(X|Y)$ is obtained by exchanging the role of X and Y in the definitions above to quantify the coupling $X \to Y$.

3.5.3.2 L measure

The measure $L(Y|X)$ is obtained from ranks [48]. We begin with $\boldsymbol{D}^{Y\to X}$ and define the cross-rank matrix $\boldsymbol{B}^{Y\to X}$, where the i-th row of $\boldsymbol{B}^{Y\to X}$ is obtained by ranking the values of the i-th row of $\boldsymbol{D}^{Y\to X}$. The mean rank is given by $G(Y) = \frac{1}{N}\sum_{j=1}^{N} j = \frac{N+1}{2}$ and the mean of the first k ranks by $G^k(Y) = \frac{1}{k}\sum_{j=1}^{k} j = \frac{k+1}{2}$. The mean rank of the distances from $\boldsymbol{y}_i$ to its k conditioned nearest neighbors is determined by $G_i^k(Y|X) = \frac{1}{k}\sum_{j=1}^{k} B_{ij}^{Y\to X}$. Finally, in analogy to (3.18), we define

$$L(Y|X) = \frac{1}{N}\sum_{i=1}^{N}\frac{G(Y) - G_i^k(Y|X)}{G(Y) - G^k(Y)}. \tag{3.19}$$

The measure $L(Y|X)$ quantifies the coupling $Y \to X$, and by exchanging the role of X and Y in the definitions above, we obtain the measure $L(X|Y)$ to quantify the coupling $X \to Y$.

3.5.3.3 ρ measure

The measure $\rho(Y|X)$ (also called the convergent cross-mapping) [5] quantifies the cross-mapping property by constructing an estimate of one time series from the conditioned nearest neighbors. The estimate is constructed back in the one-dimensional domain by reducing the delay embedded points to their first component. First, we define the cross-mapping matrix $\boldsymbol{C}^{Y\to X}$, where $C_{ij}^{Y\to X} = y(t_{P_i^X(j)})$ is the first component of the j-th conditioned nearest neighbor of $\boldsymbol{y}_i$. The estimate of each point is then defined as

$$\hat{y}(t_i) = \sum_{j=1}^{k} w_{ij}^X C_{ij}^{Y\to X}, \tag{3.20}$$

where

$$w_{ij}^X = \frac{\exp(-D_{ij}^X/D_{i1}^X)}{\sum_{l=1}^{k}\exp(-D_{il}^X/D_{i1}^X)} \tag{3.21}$$

are normalized weights. After constructing an estimate of the whole time series $(\hat{y}(t_1), \hat{y}(t_2), \ldots, \hat{y}(t_N))$, the linear zero-lag Pearson correlation coefficient between the estimate and the original time series is calculated

$$\rho(Y|X) = \mathrm{corr}(y, \hat{y}) \tag{3.22}$$

as the final measure that quantifies the coupling $Y \to X$. The measure $\rho(X|Y)$ is obtained by exchanging the role of X and Y in the definitions above to quantify the coupling $X \to Y$.

All three measures, M, L, and ρ are distributed around 0 for independent dynamics and reach the maximal value of 1 when the two time series are identical. Essentially, they all assess whether conditioned nearest neighbors are also true neighbors. Due to their high sensitivity to directional couplings, the state space methods are used in various fields of science, including ecology, [5], medicine [9], and neuroscience [13].

3.6 Surrogate Data

The measures defined in the previous sections are all sensitive to couplings. If a coupling is present between the underlying systems, then the measures will have larger values than if a coupling was not present. However, other signal properties can also influence the measures' values. For instance, a strong linear cross-correlation between two time series often leads to large values of the measures. In the simplest scenario, one can obtain an arbitrary degree of linear cross-correlation without coupling by linear mixing of two signals, measured from independent systems. Hence, the question arises: what values of the coupling detection measures can be expected in the absence of coupling but in the presence of some degree of linear cross-correlation between the time series?

This problem can be addressed by the concept of surrogate data [47], [50], [51]. The surrogate data methods provide different constrained randomization procedures of the original time series. The result is a surrogate time series that retains some of the properties of the original time series, such as the distribution of values. All the other properties are destroyed by the randomization. Randomization allows for the computation of a number of surrogates, which correspond to different realizations of the same system. Thus, the value of a chosen measure computed for the measured time series can be compared to

the distribution of values obtained from the surrogates. Formally, this allows for testing various null hypotheses about the dynamics underlying the measured time series.

Each type of surrogate corresponds to its own specific null hypothesis. A procedure for computing the surrogates is designed such that all the assumptions of the respective null hypothesis hold for the surrogate time series. For example, the Fourier transform surrogates retain the power spectral density of the original time series [51]. The procedure to compute them is to simply randomize the phases of the signal's Fourier transform and then apply the inverse Fourier transform to return to the time domain. The result is a surrogate time series with an identical power spectral density to that of the original time series but is otherwise random. Formally, these surrogates can be used to test whether the data were generated by a stationary linear correlated Gaussian process. They are used to test for nonlinearities within a time series. Other surrogate types include, for example, the wavelet transform-based surrogates, the cycle shuffled surrogates, and the twin surrogates [52]. In what follows, we discuss using bivariate surrogates to aid in detecting directional couplings.

3.6.1 Bivariate iterative amplitude adjusted Fourier surrogates

This dissertation will combine the state space measures with the surrogates in Chapter 5.2. These measures detect signatures of nonlinear interdependence between the underlying dynamics. The term nonlinear interdependence can mean either nonlinear coupling between linear systems or any coupling between nonlinear systems. However, linear cross-correlation can also strongly influence them, which is a drawback. This suggests that constructing bivariate surrogates that retain linear cross-correlation between two signals can be beneficial in assessing whether large values of the measures are due to nonlinear interdependence or due to linear cross-correlation. Such bivariate surrogates are now introduced.

Starting with a pair of time series $x(t_i)$ and $y(t_i)$, one can construct a bivariate surrogate $s_x(t_i)$, $s_y(t_i)$ such that it *retains the distribution of values and the power spectral density of each individual time series, as well as the linear cross-correlation between them, but is otherwise random.* Note that the power spectral densities exactly determine the auto-correlations. Thus, the corresponding null hypothesis consists of the following assumptions: the bivariate time series was generated by a bivariate, linear, stochastic, correlated, Gaussian process. This is because such a process is exactly determined by the auto-correlations of the two components and the cross-correlation between them. Since the distributions of values are preserved in the surrogates, they are also consistent with the notion that the time series were obtained through an invertible but potentially nonlinear measurement function [9].

Consider combining these surrogates with a state space measure. Nonlinear interdependence is not consistent with the null hypothesis, which only allows for a nonlinear measurement of a linear system. If the underlying systems are nonlinear interdependent, the value of a chosen state space measure, obtained from the original time series, will be above the range of values obtained from the surrogates. If the underlying systems are only linearly correlated, the original value will not be above the surrogate range because the level of linear cross-correlation present in the data is consistent with the null hypothesis.

There is, however, a challenge when using the surrogates. The null hypothesis should, in principle, be rejected if any one of its assumptions does not hold. For example, if a chosen directional coupling measure is influenced by the couplings and non-stationarity, then a rejection of the null hypothesis could mean that the underlying subsystems are either non-stationary or nonlinear interdependent. Therefore, all the possibilities for a specific outcome must be considered when using surrogates. Moreover, the null hypothesis often inherently does not hold in specific systems. For example, if a system is known to be strictly deterministic, the null hypothesis never holds as it assumes a stochastic process.

However, the surrogates can still provide value to such a system's analysis. Although this is not as formal as testing for different hypotheses, the surrogates can be used to provide a *baseline* for the coupling measures. This baseline provides an estimate for the value of a coupling measure, which is expected in the absence of nonlinear interdependence (which we are trying to detect) but with signal properties common to the original time series. If the original value (obtained from measured time series) is larger than the distribution of surrogate values, this provides additional verification of the existence of coupling.

The procedure for constructing the bivariate surrogates described above is called *bivariate iterative amplitude adjusted Fourier surrogates* and consists of the following steps [51]:

1. Compute the Fourier transform of the two time series $x(t_i)$ and $y(t_i)$, resulting in the amplitudes $|F_{x,k}|$,$|F_{y,k}|$ and the phases $\phi_{x,k}$,$\phi_{y,k}$. Here, k is the frequency index, and i is the time index.

2. Generate random permutations of the time series $x(t_i)$ and $y(t_i)$, resulting in $s_x^{(0)}(t_i)$ and $s_y^{(0)}(t_i)$.

3. Fourier transform the current (j-th) iterations $s_x^{(j)}(t_i)$ and $s_y^{(j)}(t_i)$ to obtain the amplitudes $|F_{x,k}^{(j)}|$,$|F_{y,k}^{(j)}|$ and the phases $\psi_{x,k}^{(j)}$,$\psi_{y,k}^{(j)}$. Replace the Fourier amplitudes with those of the original time series $|F_{x,k}|$ and $|F_{y,k}|$. This ensures that both resulting time series will have an identical power spectral density to the respective original time series.

   Replace the phases with $\phi_{x,k}^{(j)} = \psi_{x,k}^{(j)} + \alpha_k^{(j)}$ and $\phi_{y,k}^{(j)} = \psi_{y,k}^{(j)} + \alpha_k^{(j)}$, where $\alpha_k^{(j)}$ is determined by

$$\tan(\alpha_k^{(j)}) = \frac{\sin(\phi_{x,k}^{(j)} - \phi_{x,k}) + \sin(\phi_{y,k}^{(j)} - \phi_{y,k})}{\cos(\phi_{x,k}^{(j)} - \phi_{x,k}) + \cos(\phi_{y,k}^{(j)} - \phi_{y,k})}. \tag{3.23}$$

   Here, $\alpha_k^{(j)}$ must be chosen in the correct quadrant. This ensures that the resulting pair of time series will have an identical linear cross-correlation to the original pair of time series.

   Apply the inverse Fourier transform to obtain the time series $\tilde{s}_x^{(j+1)}(t_i)$ and $\tilde{s}_y^{(j+1)}(t_i)$. These time series have identical Fourier amplitudes and cross-correlation to the original ones.

4. Rescale the values of the time series $\tilde{s}_x^{(j+1)}(t_i)$ and $\tilde{s}_y^{(j+1)}(t_i)$ to the values of the original time series $x(t_i)$ and $y(t_i)$, resulting in two time series $s_x^{(j+1)}(t_i)$ and $s_y^{(j+1)}(t_i)$. This is done by permuting the values of $x(t_i)$ and $y(t_i)$ such that the rankings of $\tilde{s}_x^{(j+1)}(t_i)$ and $\tilde{s}_y^{(j+1)}(t_i)$ are identical to the rankings of the resulting $s_x^{(j+1)}(t_i)$ and $s_y^{(j+1)}(t_i)$, respectively. This step ensures that both resulting time series have identical value distributions to the respective original time series.

5. Repeat steps 3 and 4 until convergence. As the final surrogate signals, take $\tilde{s}_x^{(j+1)}(t_i)$ and $\tilde{s}_y^{(j+1)}(t_i)$ to exactly preserve the power spectrum and the cross-correlation (type-2 surrogate), or take $s_x^{(j+1)}(t_i)$ and $s_y^{(j+1)}(t_i)$ to exactly preserve the value distribution (type-1 surrogate). In either case, the other property will be nearly, though not completely identical.

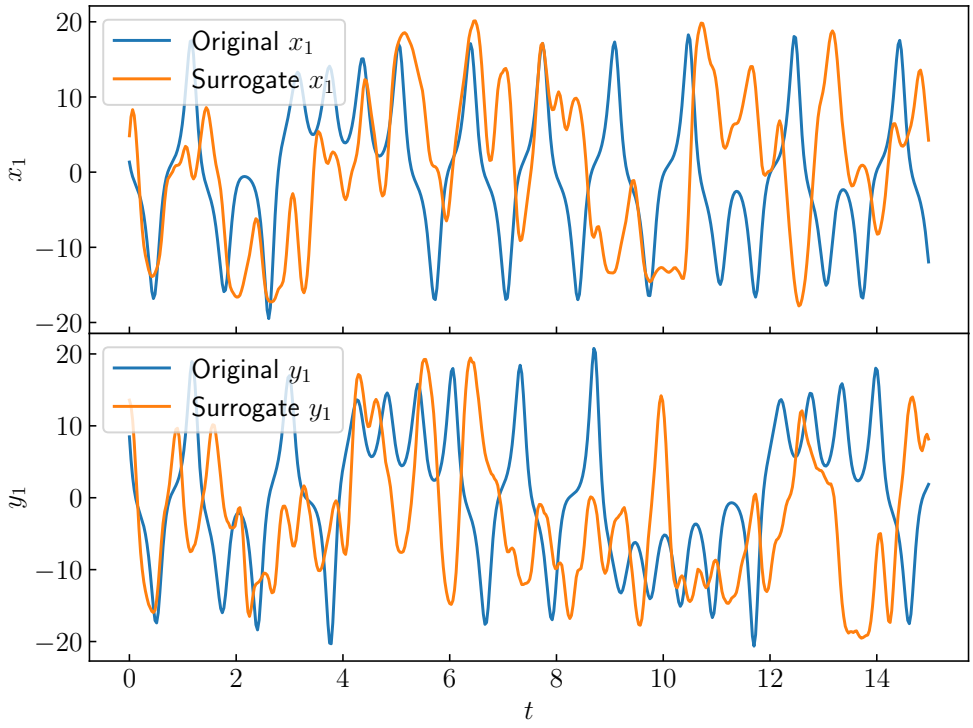

Figure 3.3: The components x_1 (a) and y_1 (b) of a realization of the Lorenz dynamics (3.24) with $\varepsilon = 0$, sampled at $\Delta t = 0.03$ and their bivariate iterative amplitude adjusted Fourier surrogate. The plots show only the beginning of a longer signal of length $t_{max} = 300$.

3.6.2 Example

The following example illustrates the usefulness of the surrogates for detecting directional couplings. Consider a pair of unidirectionally coupled Lorenz systems [53] with offset parameters

$$\begin{aligned}
\frac{dx_1}{dt} &= 10(x_2 - x_1) + \varepsilon(y_1 - x_1) \\
\frac{dx_2}{dt} &= 35x_1 - x_2 - x_1x_3 \\
\frac{dx_3}{dt} &= x_1x_2 - \frac{8}{3}x_3 \\
\frac{dy_1}{dt} &= 10(y_2 - y_1) \\
\frac{dy_2}{dt} &= 39y_1 - y_2 - y_1y_3 \\
\frac{dy_3}{dt} &= y_1y_2 - \frac{8}{3}y_3.
\end{aligned} \tag{3.24}$$

Both Lorenz subsystems are chaotic for all values of ε. An example of a Lorenz time series and a bivariate surrogate time series is shown in Figure 3.3. One can see that each surrogate has the same amplitudes and common oscillation frequencies as its respective time series it was obtained from, as expected. Let us compute a directional coupling measure for

this system's time series of realizations at different coupling strengths ε, and also for 19 bivariate surrogates at each ε.

Note that the null hypothesis of the surrogates formally never holds for this system, as Lorenz systems are deterministic and not stochastic. Thus, this example aims to show that combining a directional coupling measure with surrogates to get a baseline can provide additional value compared to not using surrogates. The chosen measure for this is the L measure (3.19), as it has been successfully combined with bivariate surrogates in real data [9].

Let us vary the coupling strength ε equidistantly on a logarithmic scale, from a negligibly small value up to and above the threshold that leads to generalized synchronization. The system is again solved numerically with random initial conditions using a fourth-order Runge-Kutta integrator with integration step 0.005. Each realization's first 10^6 points are discarded to remove transients, and the rest are sampled at $\Delta t = 0.03$. Finally, 10^4 samples of each subsystem's first component x_1 and y_1 are analyzed. The L measure is computed by applying the Theiler correction with an exclusion window of $W = 50$ samples, as discussed in Chapter 3.5. The nearest neighbor parameter is $k = 10$. For simplicity, the embedding parameters $\tau = 1, m = 20$ are used.

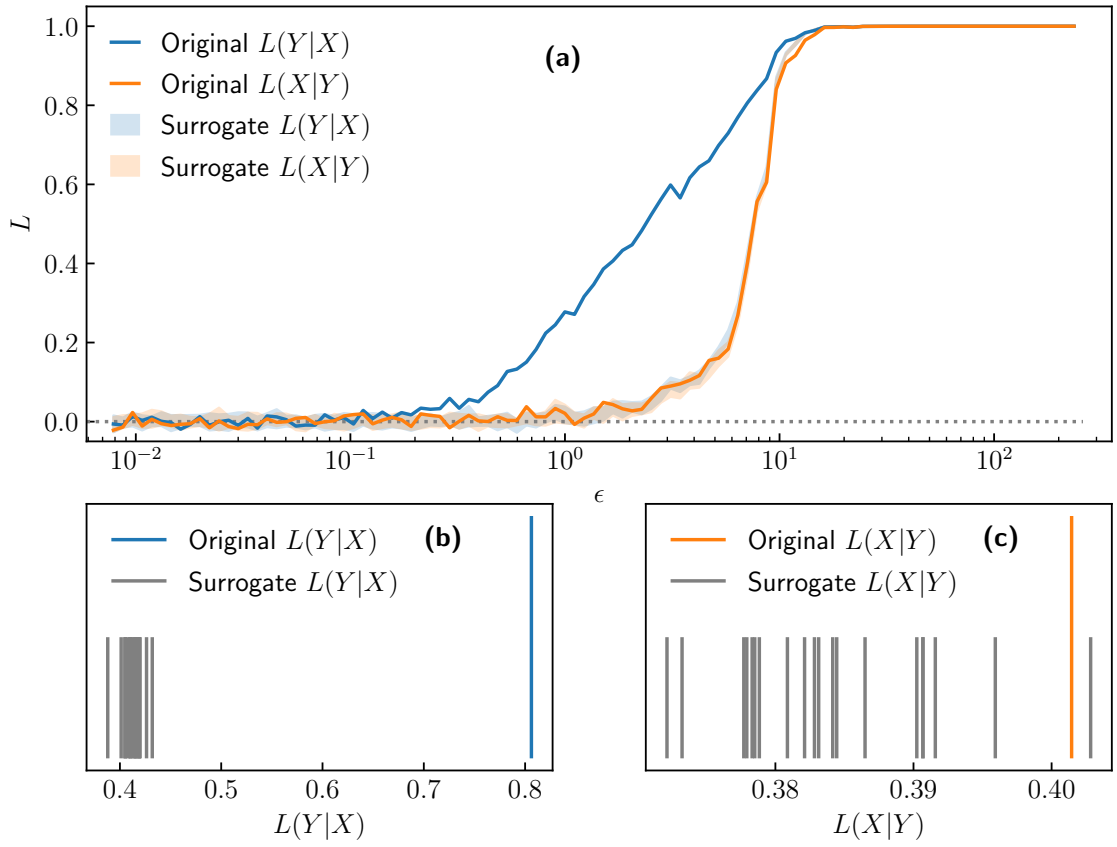

Figure 3.4: (a) The values of $L(Y|X)$ and $L(X|Y)$ computed for realizations of the coupled Lorenz systems (3.24) at different coupling strengths ε. Recall that a unidirectional coupling $Y \to X$ is present in the dynamics. The colored bands represent the range of the 19 values obtained from surrogates at each ε. Note that both surrogate bands coincide with the values $L(X|Y)$ obtained from the original time series for all ε. Panels (b) and (c) compare the original values of $L(Y|X)$ and $L(X|Y)$, obtained for the realization at $\varepsilon = 0.7$, to their respective surrogate values.

The results are shown in Figure 3.4 (a). One can see that the values $L(Y|X)$ quickly increase with increased ε, as expected of any directional coupling measure. However, the other measure $L(X|Y)$ also begins to increase at $\varepsilon \approx 1$, although it should stay close to zero because there is no coupling $X \to Y$. This is the point where the surrogates provide their usefulness. The values of $L(X|Y)$ obtained from the original data are generally inside the range of $L(X|Y)$ values obtained from the surrogates. On the other hand, the original values of $L(Y|X)$ are significantly larger than the surrogate range of $L(Y|X)$, providing validation of a genuine coupling $Y \to X$. This shows that comparing the original values to those of the surrogates can improve the accuracy of the results.

To further prove this point, consider the realization at coupling strength $\varepsilon = 7$. In this case, the values obtained on the original time series are $L(Y|X) \approx 0.8$ and $L(X|Y) \approx 0.4$. The comparison of the original values to the surrogate values for this example is shown in Figure 3.4 (b),(c). If an experiment yielded this pair of time series, then based on the original measure values, one might conclude that the coupling between the measured subsystems is bidirectional. However, once the surrogates are included in the analysis, the true coupling direction becomes clear, as only $L(Y|X)$ is outside its surrogate range, while $L(X|Y)$ is inside its surrogate range.

3.7 Networks of Systems

The methodology discussed in this chapter concerns bivariate time series. This corresponds to the dynamics of two subsystems, ignoring potential outside influences. Using bivariate methods in a multidimensional setting of a network of systems can lead to false conclusions because bivariate methods also detect indirect interactions and common influences. This is illustrated in the following two examples.

Indirect interactions

Consider two scenarios of interactions within three subsystems X, Y, and Z. In the first, we have two couplings $Y \to X$ and $Z \to Y$, as illustrated in Figure 3.5 (a). In the second, in addition to the two couplings from the first scenario, we also have the coupling $Z \to X$, as illustrated in Figure 3.5 (b). Bivariate methods cannot distinguish between these two scenarios, as they also detect indirect influences. Applying a bivariate method three times to all the pairs of variables (X, Y), (X, Z), and (Y, Z) will give the same result for both scenarios: we will detect three couplings $Z \to Y$, $Y \to X$, and $Z \to X$. In order to distinguish a direct influence from an indirect one, a multivariate method that considers the dynamics of all three variables at once must be used.

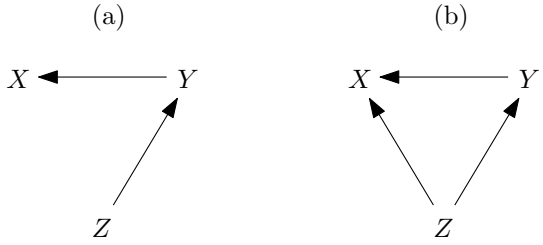

Figure 3.5: Two scenarios of interactions within a network of three systems, which a pairwise analysis cannot distinguish due to an indirect interaction $Z \to X$.

Common influences

Consider three subsystems X, Y, and Z with two couplings $Z \to X$ and $Z \to Y$, as illustrated in Figure 3.6 (a). Although there is no coupling between X and Y, a bivariate method tends to detect one because X and Y have the common influence Z. Applying a bivariate method three times to all the pairs of variables (X, Y), (X, Z), and (Y, Z) will result in also inferring a bidirectional coupling $X \longleftrightarrow Y$, incorrectly suggesting the scenario illustrated in Figure 3.6 (b). Once again, a multivariate method is necessary to exclude this possibility and detect only direct interactions.

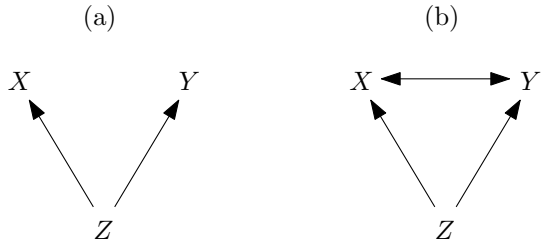

Figure 3.6: Two scenarios of interactions within a network of three systems, which a pairwise analysis cannot distinguish due to a common influence Z.

Multivariate methods

For the purpose of distinguishing direct interactions from indirect ones, various extensions of bivariate methods have been introduced. For example, multivariate extensions to Granger causality include conditional Granger causality [54], partial Granger causality [55], and partial directed coherence [56], and multivariate extensions to transfer entropy include causation entropy [57] and the PCMCI algorithm [58]. However, multivariate methods are out of the scope of this dissertation. The emphasis is on accurate quantification of directional couplings from bivariate time series.

3.8 Coupling Analysis Through a Perturbation Experiment

The methodology discussed thus far pertains to complex systems over which one does not have direct control. This is, however, not always the case. If one can perturb a subsystem directly, this enables the detection of possible couplings by observing the response of other subsystems to the perturbation. This alternative approach to coupling detection is called a perturbation experiment. Generally speaking, a perturbation experiment consists of the following steps: (1) measure the relevant quantities; (2) subject the system to some external influence (the perturbation), which is preferably controlled; and (3) measure the relevant quantities again to detect a response to the perturbation [59]. Perturbation experiments have been realized in, for example, ecology for inferring relationships between species [6], in biology for predicting the response of cells to substances [60], and in medicine for quantifying interaction strength between physiological systems [10]. The type of perturbation that can be applied to the system, as well as the choice of a quantity used to infer couplings, varies greatly depending on the specific case. Therefore, let us present an example of a perturbation experiment in a simple ecological system.

3.8.1 Example

Consider an example of an ecosystem consisting of a prey species X and a predator species Y with populations x and y, respectively. A simple model describing predator-prey dynamics is the Lotka-Volterra model [61]

$$\begin{aligned} \frac{dx}{dt} &= \alpha x - \beta xy \\ \frac{dy}{dt} &= -\gamma y + \delta xy. \end{aligned} \tag{3.25}$$

Predators Y require prey X to survive, leading to an interaction modeled by a coupling $+\delta xy$. The isolated dynamics of the predators is exponentially decreasing. Conversely, the isolated dynamics of the prey is exponentially increasing. The number of prey species is decreased when predators are present, which is modeled by a coupling $-\beta xy$. An example of a solution to the equations (3.25) is shown in Figure 3.7 (a). One can see that the populations of the two species oscillate due to their predator-prey relationship.

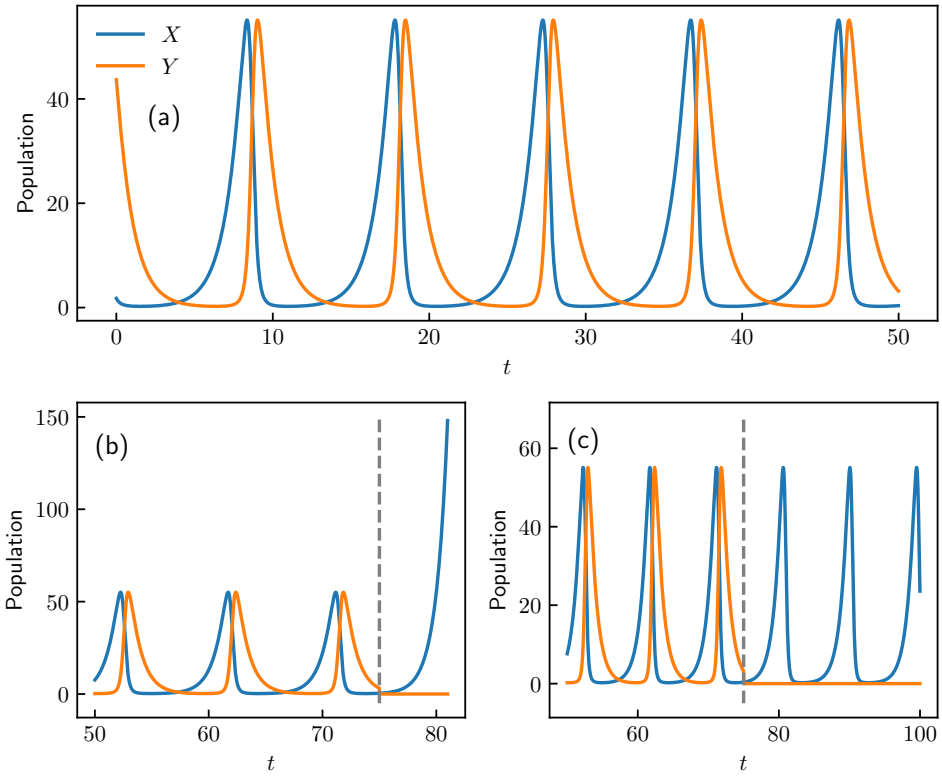

Figure 3.7: (a) A solution to the unperturbed Lotka-Volterra model with parameters $\alpha = \gamma = 1$, $\beta = \delta = 0.1$. (b) and (c) show two different responses of the population of X to the removal of Y one might expect in an experiment. The vertical gray lines show the time $t = 75$ where the perturbation is performed.

Consider a scenario in which the equations (3.25) are governing the dynamics of two species X and Y. Furthermore, consider that we do not know the underlying dynamics and wish to assess whether X and Y have a predator-prey relationship. If we can perturb the system by transporting all individuals of the species Y to a different location and thus removing them from the ecosystem, we could observe a possible relationship directly. In this case, our chosen quantity for inferring a coupling is simply the population of the

species X. If it suddenly starts increasing upon applying the perturbation, as depicted in Figure 3.7 (b), that would indicate that the two species have a predator-prey relationship. This would be the result of such a perturbation experiment conducted on a system governed by the Lotka-Volterra equations (3.25). Conversely, if the dynamics of X would stay unchanged, as depicted in Figure 3.7 (c), that would indicate there is no coupling $Y \to X$.

Chapter 4

The Inverse Problem

Consider an application of transfer entropy. One measures a pair of time series $x(t_i)$ and $y(t_i)$ and computes information flow between them. The result is two values that quantify information flow in each direction. When the time series length is finite, a positive value of information flow is expected even between two independent white noise signals. In order to assess whether an obtained value of information flow is significant, transfer entropy is usually paired with surrogate data, discussed in Chapter 3.6. The absolute value of information flow is much more challenging to interpret.

Still, numerous simulation studies have shown that information flow between two subsystems increases with increased coupling strength [8], [40], [41]. This suggests that information flow quantifies coupling strength, at least to some extent. This raises the following question: to what extent does information flow actually quantify coupling strength? This chapter investigates which scenarios result in information flow increasing monotonically with increased coupling strength.

The problem is illustrated by the following example. Consider two dynamical systems X and Y with a unidirectional coupling $Y \to X$

$$\begin{aligned} \frac{d\boldsymbol{x}}{dt} &= \boldsymbol{F}_X(\boldsymbol{x}) + \varepsilon \boldsymbol{G}_X(\boldsymbol{x}, \boldsymbol{y}) \\ \frac{d\boldsymbol{y}}{dt} &= \boldsymbol{F}_Y(\boldsymbol{y}). \end{aligned} \tag{4.1}$$

Further, consider a realization of the system at a set value of the coupling strength ε and a pair of time series $x(t_i)$ and $y(t_i)$ of length N. We are interested in the behavior of the information flow in the direction of coupling $I_{Y \to X}$. When the time series length is finite, the obtained value of $I_{Y \to X}$ varies with different system realizations. However, in the limit of infinite time series $N \to \infty$, the value of information flow will be identical for all realizations (given, of course, they are on the same attractor). Let us denote this value as $I_S(\varepsilon)$. Now, the inverse problem can be stated in the following manner: *if the dynamics of the system described by* (4.1) *are known apart from the value of* ε*, can the information flow* I_S *be used to infer the value of* ε*?*

This chapter presents original research conducted as part of this dissertation. It studies the solvability of the inverse problem in two Duffing oscillator systems [62] with a unidirectional diffusive coupling [63]. Six different Duffing systems, which exhibit both periodic and chaotic dynamics, are considered, leading to a wide range of different dynamics when coupled. All results from this study can be fully reproduced using the code available at `https://repo.ijs.si/mbresar/duffing-cmi`.

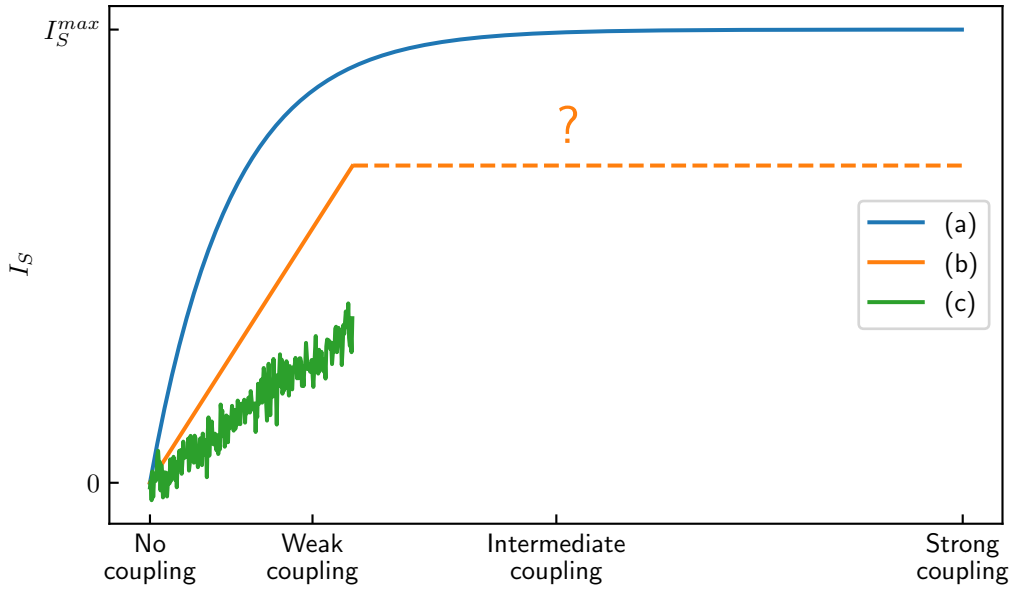

Figure 4.1: A sketch of the three possibilities for the dependence $I_S(\varepsilon)$.

Let us distinguish three possibilities for the dependence of $I_S(\varepsilon)$, depicted in Figure 4.1.

- In scenario (a), the information flow increases monotonically towards the asymptotic value I_S^{max} for all positive values of ε, and the inverse problem is solvable in general.
- In scenario (b), the information flow increases monotonically only for weak couplings, while it has an arbitrary dependence for intermediate coupling strengths. In this case, the inverse problem is solvable only if $\varepsilon < \varepsilon_{max}$ is given, where ε_{max} is the coupling strength where the information flow stops increasing.
- In scenario (c), the dependence $I_S(\varepsilon)$, while generally increasing, is not continuous and does not increase monotonically even for weak couplings. In this case, the inverse problem is not solvable.

It turns out that it does not come to the scenario (a) in systems with diffusive coupling, as such coupling leads to nearly identical coupled components when the coupling is strong, resulting in a decrease in $I_S(\varepsilon \to \infty)$.

Scenario (c) is possible when the response system is highly sensitive and can easily transition to a different orbit around a different attractor when coupled. This leads to large deviations in the obtained values of the information flow and a non-continuous, or even an undefined $I_S(\varepsilon)$.

Finally, the scenario (b) can also occur. For $I_S(\varepsilon)$ to be monotonic, it has to be (at least piecewise) continuous. Analyzing $I_S(\varepsilon)$ for different time series lengths, it turns out that it can converge towards a continuous function in the limit $N \to \infty$. The dependence $I_S(\varepsilon)$ can be continuous for all ε, in which case ε_{max} is determined by the first peak in the dependence. Additionally, it can also be continuous only for weak coupling due to system bifurcations. In this case, the onset of the first bifurcation marks ε_{max}.

Interestingly, for strong coupling where the subsystems become increasingly similar, the dependence $I_S(\varepsilon)$ is monotonically decreasing. This means the inverse problem is also solvable in the limit of strong couplings.

4.1 Solvability of the Inverse Problem in Duffing Systems Using Information Flow

Chaos ARTICLE scitation.org/journal/cha

Detection of coupling in Duffing oscillator systems

Cite as: Chaos **31**, 0631 30 (2021); doi: 1 0.1 063/5.0050790
Submitted: 1 8 March 2021 · Accepted: 28 May 2021 ·
Published Online: 1 8 June 2021

Martin Brešar,[1,2,a)] Pavle Boškoski,[1,b)] and Martin Horvat[3,c)]

AFFILIATIONS

[1] Department of Systems and Control, Jožef Stefan Institute, Jamova cesta, 39, SI-1000 Ljubljana, Slovenia
[2] Jožef Stefan International Postgraduate School, Jamova cesta 39, SI-1000 Ljubljana, Slovenia
[3] Faculty of Mathematics and Physics, University of Ljubljana, Jadranska cesta, 19 SI-1000 Ljubljana, Slovenia

[a)] **Author to whom correspondence should be addressed:** martin.bresar@ijs.si
[b)] **Electronic mail:** pavle.boskoski@ijs.si
[c)] **Electronic mail:** martin.horvat@fmf.uni-lj.si

ABSTRACT

In complex dynamical systems, the detection of coupling and its direction from observed time series is a challenging task. We study coupling in coupled Duffing oscillator systems in regular and chaotic dynamical regimes. By observing the conditional mutual information (CMI) based on the Shannon entropy, we successfully infer the direction of coupling for different system regimes. Moreover, we show that, in the weak coupling limit, the values of CMI can be used to infer the coupling parameters by computing the derivative of the conditional mutual information with respect to the coupling strength, called the *information susceptibility*. The complete numerical implementation is available at https://repo.ijs.si/mbresar/duffing-cmi.

Complex systems encountered in nature can be divided into simpler subsystems that are coupled to each other, a prime example being a biological system. The problem of the detection of coupling from measured time series of subsystems has been of great interest in different branches of science. In this article, we study methods for the detection of coupling based on information transfer on a mathematical model. We show that information transfer estimation can be used to infer the exact value of the model coupling parameter.

I. INTRODUCTION

In nature, we encounter many complex systems that are divided into better known subsystems that are coupled to each other. The subsystems can be nonautonomous, i.e., time-dependent. In experimental practice, we typically only have measurements of observables of the identified individual subsystems in the form of signals. Studying these signals naturally raises a question of what we can infer from them about the system structure, i.e., subsystem properties and their coupling. In this paper, we focus predominantly on the last property.

More precisely, we study the effects of time-independent coupling between two nonautonomous systems through information transfer or flow between the trajectories of the systems determined by the conditional mutual information.[1] As an example of such systems, we use the well known Duffing oscillators,[2] i.e., periodically driven nonlinear harmonic oscillators. Although information flow is usually observed in the context of detecting the direction of coupling, the focus here is on the absolute values of information flow in a mathematical model. The goal is to solve the inverse problem of inferring the coupling parameter in different coupled nonautonomous oscillator systems from the calculated information flow.

Estimating the conditional mutual information has been successfully applied in numerous studies, including biological systems. For example, information flow has been used in the analysis of EEG recordings of epileptic patients,[3] in rats under the influence of different anaesthetics,[4] and in the human cardiorespiratory system.[5] Studies have also been done on various theoretical systems, such as simple phase oscillators,[6] discrete Henon maps,[3] Rossler and Lorenz systems,[5] and different chaotic, stochastic, and nonautonomous systems.[7] It has been shown that information flow can correctly detect both the existence and the direction of coupling

Chaos ARTICLE scitation.org/journal/cha

in two coupled, but not yet synchronised systems. This means that the coupling must be sufficiently small. While it has been shown that the information flow between systems increases as the coupling increases, this relationship has not been thoroughly investigated.

Another measure for quantifying information transfer between systems is the transfer entropy proposed by Schreiber.[8] It has been shown that the transfer entropy in a specific (although generally useful) setup is mathematically equivalent to the conditional mutual information, see, e.g., Ref. 5 (Appendix A). In a more general setup, the transfer entropy can suffer from a lack of statistical significance of distributions (due to high parameter dimensionality) used in calculations for short input signals.

First, we study the numerical properties of the information flow calculation, where the convergence was found to be faster than expected. Next, we consider the behavior of the information flow when different pairs of Duffing systems are coupled. Addressing the issue of the dependence of the information flow on the coupling strength, we study the inverse problem, i.e., inferring the coupling parameter from the information flow. The result is an estimate of the information susceptibility as a derivative of the information flow. For details, see Sec. V C. It was found that the inverse problem is solvable in the limit of strong coupling and for most cases of driven chaotic systems in the limit of weak coupling. Finally, the range of the coupling parameter where this is possible is given for individual pairs of systems.

II. INFERRING THE DIRECTION OF COUPLING

Consider two nonautonomous dynamical systems with trajectories denoted by $\mathbf{x}(t)$ and $\mathbf{y}(t)$ and let the time evolution of such coupled systems be given by equations

$$\frac{d\mathbf{x}(t)}{dt} = \mathbf{f}_x(\mathbf{x}, t) + \mathbf{g}_x(\mathbf{x}, \mathbf{y}, t), \tag{1}$$

$$\frac{d\mathbf{y}(t)}{dt} = \mathbf{f}_y(\mathbf{y}, t) + \mathbf{g}_y(\mathbf{y}, \mathbf{x}, t), \tag{2}$$

where $\mathbf{x}(t)$ and $\mathbf{y}(t)$ can be multidimensional and are, therefore, written in bold letters. In the case where both $\mathbf{g}_x$ and $\mathbf{g}_y$ are nonzero, the coupling is bidirectional. In our studies of the inverse problem, the coupling functions $\mathbf{g}_x$ and $\mathbf{g}_y$ are time indepedent. If only one is nonzero, the coupling is unidirectional. In the subsequent analysis, only unidirectional coupling is analyzed. When $\mathbf{g}_y = 0$ and $\mathbf{g}_x \neq 0$, we call $\mathbf{x}(t)$ the driven system and $\mathbf{y}(t)$ the driving system.

The trajectories of both subsystems $\mathbf{x}(t)$ and $\mathbf{y}(t)$ are observed at equally spaced times $t_i = t_0 + i\Delta t$ for $i \in \mathbb{Z}$. Thus, we obtain time series of these trajetories $(\mathbf{x}(t_i) : i \in \mathbb{Z})$ and $(\mathbf{y}(t_i) : i \in \mathbb{Z})$. The methods presented in the following are used to determine the direction and, in some cases, the magnitude of the coupling based on such measured time series.

A. Conditional mutual information

In the context of information theory, the amount of information being transferred from one system to another is quantified by the Shannon entropy.[1] The Shannon entropy of a random variable X with a probability distribution p_X and its support R_X (subset of the range of X) is defined as

$$H(X) = -\sum_{x \in R_X} p_X(x) \log p_X(x). \tag{3}$$

The joint entropy of two random variables X and Y with a joint probability distribution $p_{X,Y}$ is defined as

$$H(X, Y) = -\sum_{x \in R_X, y \in R_Y} p_{X,Y}(x, y) \log p_{X,Y}(x, y). \tag{4}$$

Their mutual information $I(X, Y)$, which is a measure of the amount of common information contained in X and Y, is defined as

$$I(X, Y) = H(X) + H(Y) - H(X, Y) \tag{5}$$

and is maximal if $X = Y$ and equal to 0 if X and Y are independent. The conditional entropy of X and Y is

$$H(X|Y) = -\sum_{x \in R_X, y \in R_Y} p_{X,Y}(x, y) \log p_{X|Y}(x|y), \tag{6}$$

where $p_{X|Y}$ is the conditional probability distribution. Conditional entropy measures the uncertainty in X, provided that everything about Y is known. Conditional entropy $H(X, Y|Z)$ is defined similarly, which leads to conditional mutual information (CMI)

$$I(X, Y|Z) = H(X|Z) + H(Y|Z) - H(X, Y|Z). \tag{7}$$

It quantifies the average amount of common information contained in X and Y given the value of Z.

While a measurement almost certainly contains uncorrelated noise that is stochastic in nature, the underlying dynamics of the measured system can still be deterministic.

Let us consider two possibly coupled systems with trajectories $\mathbf{x}(t)$ and $\mathbf{y}(t)$. Their corresponding time series are $(\mathbf{x}(t_i) : i \in \mathbb{Z})$ and $(\mathbf{y}(t_i) : i \in \mathbb{Z})$. Their values are distributed according to the probability distributions $p_{\mathbf{X}}$ and $p_{\mathbf{Y}}$. We think of the values in the series $\mathbf{x}(t_i)$ and $\mathbf{y}(t_i)$ as a realization of the random variables denoted by $\mathbf{X}$ and $\mathbf{Y}$ at time t_i. By just discussing their distributions, we lose the information about time. To restore the notion of time, we need to introduce the time-lagged random variables $\mathbf{X}_\tau$ and $\mathbf{Y}_\tau$ with realizations $\mathbf{x}(t_{i+\tau})$ and $\mathbf{y}(t_{i+\tau})$ at times t_i and discuss them in parallel with their non time-lagged versions.

In order to infer a possible influence of the trajectory $\mathbf{x}(t)$ on $\mathbf{y}(t)$ from their time series, we need to compute the mutual information between the random variable of the first system $\mathbf{X}$ and the time-lagged random variable of the second system $\mathbf{Y}_\tau$ given by $I(\mathbf{X}, \mathbf{Y}_\tau)$. However, the mutual information captures the connection between $\mathbf{X}$ and $\mathbf{Y}$ as well as between $\mathbf{Y}$ and $\mathbf{Y}_\tau$ when the two systems are not independent. Therefore, Paluš *et al.*[3] proposed to observe the conditional mutual information $I(\mathbf{X}, \mathbf{Y}_\tau|\mathbf{Y})$ to infer causal relations between trajectories $\mathbf{x}(t)$ and $\mathbf{y}(t)$. This quantity only captures the net information flow from $\mathbf{x}(t)$ to $\mathbf{y}(t)$. A tweak to increase precision is to instead calculate

$$I(\mathbf{X}, \Delta_\tau \mathbf{Y}|\mathbf{Y}) = H(\mathbf{X}|\mathbf{Y}) + H(\Delta_\tau \mathbf{Y}|\mathbf{Y}) - H(\mathbf{X}, \Delta_\tau \mathbf{Y}|\mathbf{Y}), \tag{8}$$

where $\Delta_\tau \mathbf{Y} = \mathbf{Y}_\tau - \mathbf{Y}$. This allows us to look at small local changes in $\mathbf{y}(t)$ rather than the entire range of data. Information flow from $\mathbf{y}(t)$ to $\mathbf{x}(t)$ is calculated as $I(\mathbf{Y}, \Delta_\tau \mathbf{X}|\mathbf{X})$ by swapping $\mathbf{X}$ and $\mathbf{Y}$.

Chaos ARTICLE scitation.org/journal/cha

B. Information flow

Both $I(\mathbf{X}, \mathbf{Y}_\tau|\mathbf{Y})$ and $I(\mathbf{X}, \Delta_\tau\mathbf{Y}|\mathbf{Y})$ are zero for $\tau = 0$. However, $\lim_{\tau\to 0^+} I(\mathbf{X}, \mathbf{Y}_\tau|\mathbf{Y}) = 0$ and $\lim_{\tau\to 0^+} I(\mathbf{X}, \Delta_\tau\mathbf{Y}|\mathbf{Y}) \neq 0$. Since we are interested in small time lags in Secs. IV and V, we use the second definition.

To obtain a numerically more robust measure, we can average the CMIs $I(\mathbf{X}, \Delta_\tau\mathbf{Y}|\mathbf{Y})$ over some time lags τ in order to better approximate the information flow between two systems,[3]

$$I(\mathbf{x} \to \mathbf{y}) = \frac{1}{l}\sum_{i=1}^{l} I(\mathbf{X}, \Delta_i\mathbf{Y}|\mathbf{Y}). \tag{9}$$

The appropriate values of l are discussed in Sec. IV A.

When calculating information flow from one subsystem to another, we use the values of trajectories. The trajectories capture the full extent of information about the dynamics of a particular system and can be multidimensional. In realistic situations, however, the measurement of a system or a subsystem is usually one-dimensional. A possible solution to account for a multidimensional phase space is the use of time-delay embedding vectors[9] or instantaneous phase representation in the case of oscillatory systems.[6,10]

III. NUMERICAL ANALYSIS

Information theory is thoroughly researched and well understood. However, numerical computation of entropies is challenging due to limitations and necessary approximations. It is therefore important to be aware of them and study their effect on known systems in order to be able to analyze unknown ones.

A. Numerical implementation

A convenient way to numerically implement the calculation of CMI is to use the chain rule for entropies $H(X|Y) = H(X, Y) - H(Y)$ and rewrite (7) as

$$I(\mathbf{X}, \Delta_\tau\mathbf{Y}|\mathbf{Y}) = H(\mathbf{X}, \mathbf{Y}) + H(\Delta_\tau\mathbf{Y}, \mathbf{Y}) - H(\mathbf{Y}) - H(\mathbf{X}, \Delta_\tau\mathbf{Y}, \mathbf{Y}). \tag{10}$$

The biggest issue in calculating CMI (10) from the involved entropies is the estimation of the underlying probability distributions by the corresponding histograms. The latter are computed from long enough series of trajectories: having a time series of length n, we assign its values in each dimension into N bins, where $N \ll n$, and construct a histogram. Multidimensional histograms are used to estimate multidimensional probability distributions. Consider a system with two k-dimensional subsystems. When computing the joint entropy in CMI (10), the histogram used in its calculation has N^{3k} bins. Individual bins must contain a significant number of data points to sufficiently approximate the distribution. Therefore, the total number of bins cannot be too large.

The simplest way to construct a histogram is to use equidistant binning, which means that the widths of all histogram bins are equal. We found this binning procedure to be sufficient for our problem. Other binning procedures can also be used, such as marginal equiquantization, where the marginal bins are chosen so that they each contain the same number of data points.[5]

B. Duffing oscillator systems

The model we have chosen for numerical analysis is the Duffing oscillator system, which is studied in detail in Ref. 11. Its properties make it very convenient, since it is a nonautonomous oscillator that can be in a regular or in a chaotic dynamical regime. It is defined by

$$\frac{d^2x}{dt^2} + \delta\frac{dx}{dt} + \alpha x + \beta x^3 = \gamma\cos(\omega t). \tag{11}$$

It is a nonlinear periodically forced oscillator with damping. Its trajectory is denoted by $(x(t), \frac{dx}{dt}(t))$ and the associated phase space is two-dimensional. The choice of the model parameters $(\delta, \alpha, \beta, \gamma, \omega)$ yields different systems which can be in a regular or in a chaotic dynamical regime.[12] This allows us to test the behavior of CMI on systems in different regimes.

For regular behavior, a high damping $\delta = 0.2$ and a linear potential $\beta = 0$ were chosen. The orbits of the chosen regular systems are circles, same as in normal driven harmonic oscillators, while chaotic systems exhibit richer dynamics. For chaotic behavior, it is beneficial to have low damping. In fact, increasing the damping parameter δ of a chaotic system makes it regular. Four different chaotic systems denoted C_1 to C_4 and two regular ones denoted R_1 and R_2 were chosen. The parameters and the maximal Lyapunov exponents of the chosen systems are presented in Table I. The maximal Lyapunov exponents were calculated from the stroboscopic map at $\cos\omega t = 1$ using the Benettin algorithm.[13] The negative maximal Lyapunov exponents of regular systems were obtained due to orbits converging toward a limit cycle. Two examples of chaotic systems are shown in Fig. 1.

Systems C_1 and C_2 are similar to each other, and so are C_3 and C_4, as can be seen from the table of parameters. Systems C_1 and C_2 have a highly nonlinear potential (high β) and no damping ($\delta = 0$), while C_3 and C_4 have a small β and a high δ, making their dynamics less "wild" but still chaotic. In fact, the system C_4 has a fractal attractor with dimension of around 1.4.[14] The driving frequencies ω of the different systems were chosen so that one is not a multiple of another.

C. Duffing system's CMIs

Two Duffing systems can be coupled in different ways. We have chosen a unidirectional linear coupling of the form $+\varepsilon_1(x_2 - x_1)$ due to its intuitive interpretation. Such a coupling forces the driven

TABLE I. Parameters of the six Duffing systems under consideration and their maximal Lyapunov exponents λ_{max}. The systems R_1, R_2 are in a regular regime. The chaotic systems C_1, C_2 have a high nonlinear term and C_3, C_4 have a low nonlinear term.

System	δ	α	β	γ	ω	λ_{max}
R_1	0.2	1	0	1	0.51	−1.23(2)
R_2	0.2	1	0	1	1.83	−0.34(3)
C_1	0	1	400	1	1.1	0.6(2)
C_2	0	1	80	1	3.1	0.2(3)
C_3	0.3	−1	1	0.5	1.2	0.5(7)
C_4	0.2	−1	1	0.3	1	0.9(9)

Chaos ARTICLE scitation.org/journal/cha

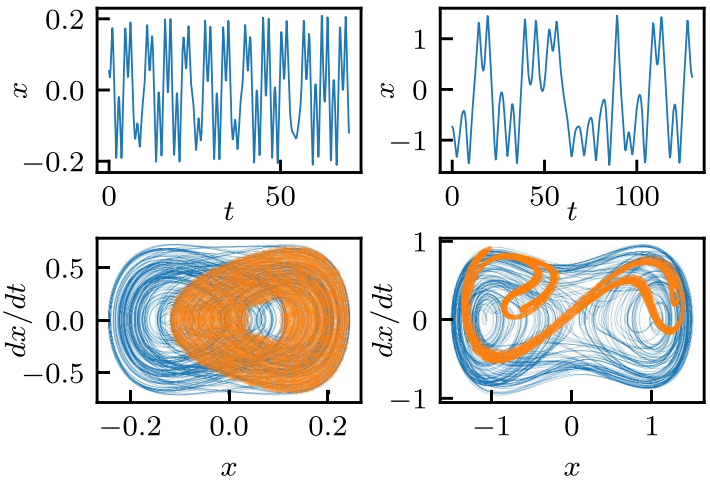

FIG. 1. Chaotic Duffing oscillator systems C_1 (left) and C_4 (right). The orange dots represent a stroboscopic map at $\cos(\omega t) = 1$ obtained for long times $t_{\max} = 10^5$.

system toward the driving system and can cause synchronization. If the coupling is very strong, the systems become identical. Coupled Duffing systems are thus defined as

$$\frac{d^2x_1}{dt^2} + \delta_1 \frac{dx_1}{dt} + \alpha_1 x_1 + \beta_1 x_1^3 = \gamma_1 \cos(\omega_1 t) + \varepsilon_1 (x_2 - x_1), \quad (12)$$

$$\frac{d^2x_2}{dt^2} + \delta_2 \frac{dx_2}{dt} + \alpha_2 x_2 + \beta_2 x_2^3 = \gamma_2 \cos(\omega_2 t). \quad (13)$$

While the term driven can also be used to describe an individual Duffing oscillator, i.e., it is driven by an external periodic force, we use the terms driving and driven to distinguish between x_1 and x_2. We say that the driven system x_1 depends on the driving system x_2.

We write a trajectory of the coupled Duffing system as $(x_1(t), \frac{dx_1}{dt}(t), x_2(t), \frac{dx_2}{dt}(t))$ and trajectories of its subsystems as $\mathbf{x}_i(t) = (x_i(t), \frac{dx_i}{dt}(t))$ for $i = 1, 2$. The phase space of the whole system is thus four-dimensional. In our calculations, we ensured that our system is on the attractor so that the results do not depend on the initial conditions. This was accomplished by taking the initial conditions $(x_1(0), \frac{dx_1}{dt}(0), x_2(0), \frac{dx_2}{dt}(0)) = (0, 0, 0, 0)$ and only considering the data from the trajectories from time $t = 100$ onward. This way, the energy of the system is gained entirely from the nonautonomous parts of subsystems (12) and (13).

The trajectory of the whole system, or more precisely, the corresponding time series, was obtained by first transforming the equations of motion (12) and (13) to a system of four first order differential equations and then integrating them using the Runge–Kutta 4 integrator with a fixed integration step equal to $\Delta t = 0.002$ and the time series length of $n = 10^7$ throughout our study. The use of a constant integration step is convenient for calculating probability distributions of points on the trajectory. In the calculation of the histogram of points pertaining to the evaluation of CMI, we use equidistant binning for each two-dimensional subsystem, as explained in Sec. III A. In this study, we use 4 bins for x direction and 4 for dx/dt direction unless otherwise specified. This effectively gives 16 bins per subsystem.

The convergence of CMI with the length of the trajectory t, more precisely the number of steps in the sample $n(\approx t/\Delta t)$, is shown in Fig. 2. In the direction without coupling (a), the CMI values decrease with the length of the time series n and stabilize at a nonzero value. We attribute this to approximation errors of the discrete probability distributions. In the direction of coupling (b), the values converge to a constant. The convergence is slower in the

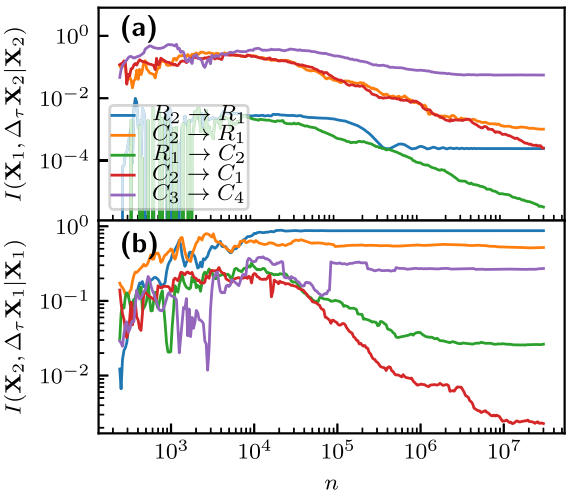

FIG. 2. The convergence of CMI (8) for time lag $\tau = 1$ between different systems in the direction without coupling (a) and in the direction of coupling (b). The coupling parameter is $\varepsilon_1 = 0.5$, the integration step is $\Delta t = 0.002$ and 4 bins per scalar variable were used in the histograms.

Chaos ARTICLE scitation.org/journal/cha

presence of chaotic systems, especially for C_1 and C_2. In a certain range of ε_1 we see that the dependence is linear in the log–log scale. Fitting a function of the form $f(t) = At^{-C}$ in this range, we obtain the coefficient $C = 1$ for convergence, even for chaotic systems.

This is a bit surprising, since CMI is essentially a difference of entropies determined by the empirical distributions which converge for periodic and stochastic (chaotic) signals as $O(t^{-1})$ and $O(t^{-1/2})$, respectively. The latter was checked in our study. The $O(t^{-1})$ convergence of CMI is therefore faster than of its ingredients. This seems to be a consequence of the fact that the stochastic corrections to entropies of order of magnitude $O(t^{-1/2})$ are correlated and cancel each other out in the calculation of CMI, and only the next possible order $O(1/t)$ remains. This is good news for the usability of CMI, as even shorter samples can deliver relatively precise results. Further discussion of the convergence is given in Appendix A.

IV. ANALYSIS OF CMI AND INFORMATION FLOW

We have defined CMI between two subsystems and information flow as the average of CMIs over time lags. In this section, we study the behavior of these quantities for various combinations of coupled Duffing systems. Mainly, we examine the dependence of CMI on the time lag and the dependence of information flow on the coupling parameter. We denote the direction of coupling by (C) and the direction without coupling by (N), e.g., information flow in the direction of coupling is denoted by $I(C)$. Here, C stands for coupled and N stands for not coupled.

A. Dependence of CMI on the time lag

First, it is important to observe the dependence of CMIs (8) on the time lag τ in order to determine the averaging in the definition of information flow (9). It is shown for four examples of coupled Duffing systems in Fig. 3.

Three main conclusions can be drawn from these dependences. First, we note that the values in the direction of coupling CMI(C) (upper row) are much larger than CMI(N) (lower row), as can be seen in all examples from (a) to (d). Therefore, the CMI values can be used to determine the direction of coupling. Second, we see that CMI(C) increases with increased coupling ε_1. This means that our measure of coupling between systems increases with coupling. Finally, CMI(C) decreases with increased time lag. It falls with the correlation time of the time-lagged system. On the contrary, CMI(N) increases with increased time lag. An exception is the system $C_2 \to C_1$, where CMI(C) increases again to an even higher value at $\tau\Delta t \approx 1$ and then proceeds to decrease.

This shows that the appropriate averaging in the definition (9) is over small time lags τ, where the values of CMI are large and information about the driving system is still present in the driven one. The averaging decreases errors due to dynamic fluctuations and possible noise. The simulation of the system is noiseless and the errors of dynamical fluctuations are decreased with the length of the time series. Therefore, taking only one value of CMI is shown to be sufficient. Since CMI(C) generally falls and CMI(N) generally increases for small time lags, the values at the smallest possible time lag $\tau = 1$ are taken into account. Our measure of information flow in either direction is therefore the very first point in Fig. 3.

Since oscillator systems are similar to themselves when they are time-lagged, we also detect oscillations at the frequency of the time-lagged system. They are most expressed for the system $R_1 \to C_2$. It is important to mention that while CMI generally decreases with τ for small coupling, the dependence can be different for bigger coupling.

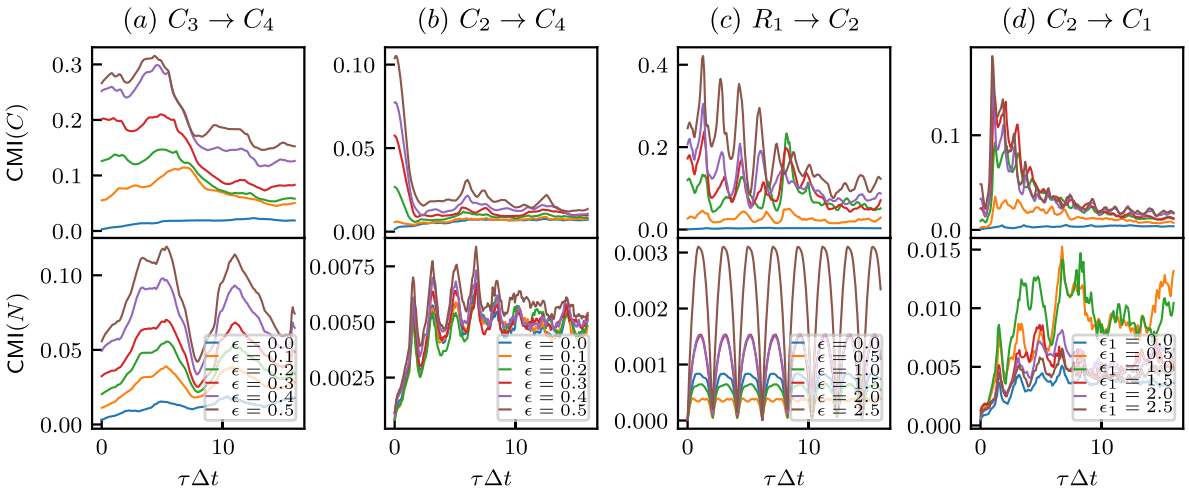

FIG. 3. The dependence of CMI in both directions on the time lag τ. Four different systems are examined from (a) to (d).

Chaos ARTICLE scitation.org/journal/cha

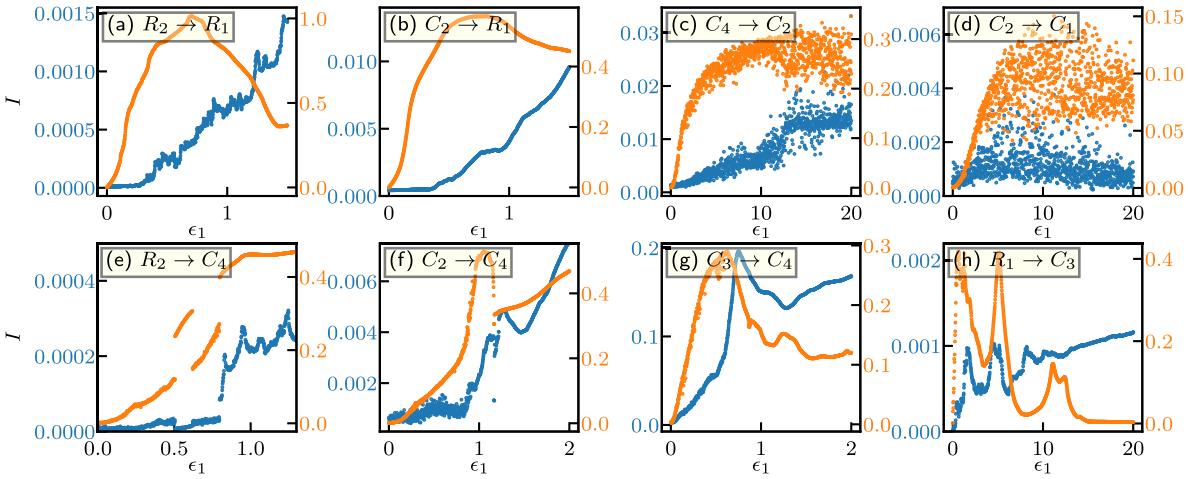

FIG. 4. The dependence of the information flow (9) on the coupling parameter ε_1. The orange lines represent the flow in the direction of coupling $I(C)$ and the blue lines in the direction without coupling $I(N)$. The dependences for weak coupling are shown for various systems in (a) to (g). For the system $R_1 \to C_3$, strong coupling is also shown in (h). The calculations were done for 1000 evenly spaced values of ε_1 for each case.

B. Dependence of information flow on the coupling parameter

We can now study the information flow between different systems to see how it characterises them. The focus here is on observing the dependence of the information flow on the coupling parameter. This dependence is shown in Fig. 4 for various coupled Duffing systems.

The general behavior is similar for any two coupled systems. The information flow $I(C)$ is very close to 0 in the absence of coupling, since the systems are independent. It then generally increases as the coupling parameter increases. This can be seen in the examples from (a) to (f) in Fig. 4.

For intermediate values, this dependence can have many local extremes until it begins to decrease and reaches zero in the limit $\varepsilon_1 \to \infty$, as indicated by Fig. 4(h). In this limit, the systems are the same because the orbit of one system is pushed toward that of the other, and there is no information transfer between identical systems.

It can also be seen that $I(C)$ is much greater than $I(N)$. This means that the direction of coupling can be easily inferred from the information flow. There are some exceptions when it comes to bigger coupling, one of which can be seen in Fig. 4(g). We have not found a general rule for which systems exhibit this property. However, it seems to occur when similar pairs of systems are coupled, for example for all four cases $C_i \to R_j$, for $i, j \in \{1, 2\}$.

In the limits of weak and strong coupling, the dependence can be monotonic, which will be discussed in detail in Sec. V. A difference is observed between chaotic systems with high and with low nonlinear terms β. If the driven system is one with a high nonlinear term C_1 or C_2, the dependence appears much more noisy, especially when two of these systems are coupled. Monotonicity is harder to show or find in these cases, which makes solving the inverse problem harder.

V. THE INVERSE PROBLEM

In this section, we are interested in whether the coupling parameter is uniquely determined by the information flow $I(C)$ in some range of values, i.e., whether this dependence is monotonic. If this is the case, the coupling parameter can be inferred from the time series of two known systems by calculating the information flow.

For most pairs of systems, there are two cases that exhibit monotonic dependence of the information flow on the coupling parameter, as indicated in Sec. IV B. The first is the limit of strong coupling, i.e., for large values of the coupling parameter. The second is the limit of weak coupling, which is most often observed in nature. These limiting cases will be studied in detail. For intermediate values, the inverse problem is generally not solvable.

A. Limit of strong coupling

First, we consider the limiting case of large coupling parameters ε_1. As explained in Sec. IV B, the information flow $I(C)$ decreases toward zero in this limit. The dependence for large ε_1 is shown in Fig. 5 in a double logarithmic scale. Since the dependence in this scale is linear for sufficiently large ε_1, we know its form is

$$f(\varepsilon_1) = A\varepsilon_1^{-B}. \tag{14}$$

Using least squares regression on points in the marked areas, the value $B = 1$ was obtained for all cases. The obtained formulas hold for a wide range of values of ε_1. The value $B = 1$ holds regardless of the number of bins chosen, as does the range of ε_1 with this

Chaos ARTICLE scitation.org/journal/cha

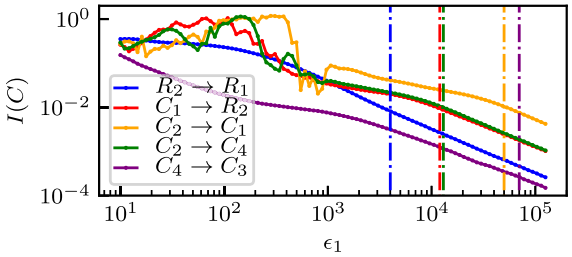

FIG. 5. Information flow in the direction of coupling for large ε_1 for different coupled systems. Vertical lines mark the lower boundaries of areas used for regression.

dependence (checked up to 24 bins per variable). Thus, the inverse problem is solvable in the limit of large coupling.

B. Limit of weak coupling

The case of weak coupling is much more interesting, since it is usually encountered in physical systems. All numerical tests suggest that in most cases the information flow grows monotonically with increasing ε_1, up to a value $\varepsilon_{\max}$ where the monotonicity ends. It may end due to a distinct peak in the dependence, as in Figs. 4(f) and 4(g), due to a discrete jump as in Fig. 4(e), or due to the appearence of noise as in Fig. 4(c). The analysis of different coupled Duffing systems gives different answers to the solvability of the inverse problem.

In most cases where the monotonicity ends with a distinct peak in the dependence on the coupling parameter, it is due to the synchronization of subsystems. In a mathematical model, the appearance of synchronization can be observed with conditional Lyapunov exponents (CLE), i.e., the Lyapunov exponents of the driven subsystem.[15] The dependence of the information flow on ε_1 and the dependence of CLE on ε_1 is shown in Fig. 6 for one of these cases. Synchronization, which is marked by the largest exponent becoming negative, occurs close to the point where the dependence of the information flow suddenly changes, which is similar to observations made in Refs. 5 and 16. A thorough survey on synchronization is given in Ref. 17.

In cases of the discrete jumps in the information flow dependence, the observation of phase state portraits and conditional Lyapunov exponents reveal bifurcations of the driven subsystem. These cases are examined in detail in Appendix B.

Let us now consider two coupled regular systems $R_2 \to R_1$. The dependence in Fig. 4(a) indicates a monotonic trend up to $\varepsilon_{\max} \approx 0.7$. This value should not strongly depend on the details of numerical calculation in order to determine the value of $\varepsilon_{\max}$ as a property of a system.

By increasing the number of marginal bins N, the results approach the exact analytic dependence for smooth variables.[18] However, $\varepsilon_{\max}$ moves toward 0 as the number of marginal bins of the histograms increases, as can be seen in Fig. 7. This is observed in all cases when the driven system is regular. We have done the same test with two coupled harmonic oscillators and obtained very similar results. Therefore, we suspect that this is due to the singularity of the probability distribution $p(x, dx/dt)$ of regular systems, since their orbits are circles in 2D space and even a very weak coupling changes the probability distributions significantly so that it cannot be explained by linear perturbation theory.

For driven chaotic systems, the value of ε_{max} did not change for different numbers of histogram bins. The numerical analysis of $R_1 \to C_2$ is done in Fig. 8. Increasing the number of marginal bins N while keeping the length of the time series n constant does not affect the general shape, as seen in Fig. 8(a). However, the values increase at $\varepsilon_1 = 0$ because the bins become poorly populated. With increasing length n at a high $N = 16$, the value decreases again toward 0, as seen in Fig. 8(b). This shows that while a finer partition is generally beneficial, taking too many bins will cause them to be poorly populated and distorts the results.

Moreover, the dependence is found to converge toward a monotonic dependence as n is further increased. Due to numerical imprecisions, the dependence will never be exactly monotonic when considering values of ε_1 that are very close to each other. Instead, we show monotonicity empirically by doing ever more

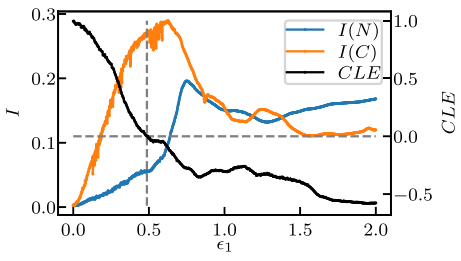

FIG. 6. Information flow in both directions and the largest Lyapunov exponent of the driven subsystem (conditional Lyapunov exponent) for system $C_3 \to C_4$. Gray lines represent the point where the exponent reaches zero, i.e., the point of synchronization.

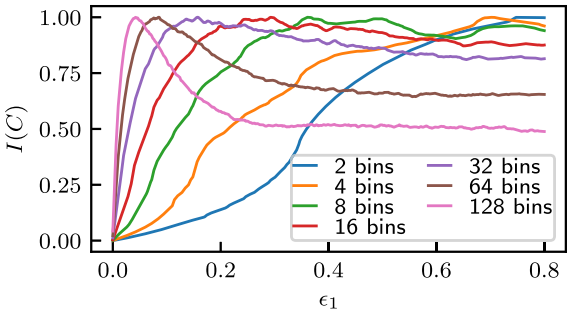

FIG. 7. Information flow in the direction of coupling for unidirectionally coupled systems $R_2 \to R_1$, calculated with different numbers of bins per variable N. The dependences are normalized to be easily comparable.

Chaos ARTICLE scitation.org/journal/cha

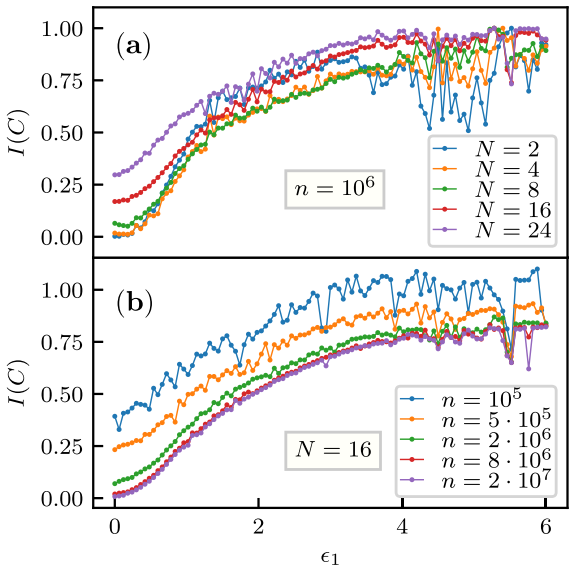

FIG. 8. Information flow in the direction of coupling for unidirectionally coupled systems $R_1 \to C_2$, calculated with data length $n = 10^6$ at different number of bins N (a) and with $N = 16$ at different n (b). In (a), the dependences are normalized to be easily comparable.

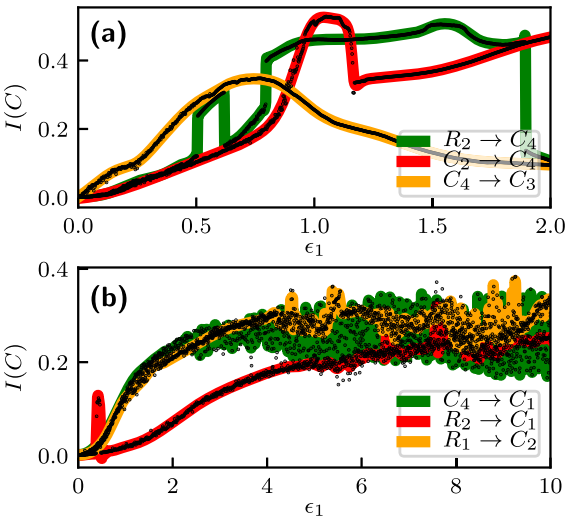

FIG. 9. Information flow data and their smoothed fit as a function of the coupling parameter ε_1 for different pairs of systems, driven system having a small (a) and a large (b) nonlinear term.

precise calculations. These can be done by increasing n, and perhaps N. Decreasing the time step of the integration Δt changes the results only minimally.

For most cases of driven chaotic systems, monotonicity has been shown in the regime of weak coupling strength ε_1. For the coupling of two systems with high nonlinear term $C_i \to C_j$, for $i, j \in \{1, 2\}$, seen in Fig. 4(d), the dependence always contains a lot of noise that does not decrease with longer time series. This is due to bifurcations already at very small values of the coupling parameter. Bifurcations of the driven system destroy the monotonicity, as explained in the next section.

C. Information susceptibility

To determine the values of $\varepsilon_{\max}$, we introduce a smooth function I_s obtained by fitting splines to the dependence of the information flow $I(C)$ on the coupling constant. This allows us to calculate the information susceptibility, which we define as

$$\chi_I(\varepsilon_1) = \frac{dI_s}{d\varepsilon_1}(\varepsilon_1). \tag{15}$$

The smooth dependence allows a simple calculation of the derivative, which is not possible for discrete points of the information flow. The information susceptibility $\chi_I(\varepsilon_1)$ is positive for small ε_1. While it is positive, the dependence of CMI on ε_1 is monotonic and the inverse problem is solvable. The value of $\varepsilon_{\max}$ is then marked by the change of sign of $\chi_I(\varepsilon_1)$, i.e., the first point at which it is equal to 0.

This was done for systems where a monotonic dependence on the coupling parameter was found. The function `UnivariateSpline` from the package `scipy.interpolate` in `Python 3` was used to obtain I_s. Parameters chosen were $k = 3$ for cubic splines and a smoothing factor between $0.005 \leq s \leq 0.1$.

For the cases where the driven system is either C_3 or C_4, this is straightforward most of the times, as can be seen in Fig. 9(a). An odd example $R_2 \to C_4$ can also be seen. It contains a nonsmooth dependence at $\varepsilon_1 = 0.51$. Observing the phase space portraits of the driven system has shown that this is due to bifurcations. For $0.51 < \varepsilon_1 < 0.61$ and for $\varepsilon_1 > 0.8$ the driven subsystem C_4 is in a regular periodic regime. If the driven system's dynamics change significantly at some value of ε_1 before a distinct peak in the information flow is observed (in this case at $\varepsilon_1 = 0.51$), this value marks $\varepsilon_{\max}$. Such cases are shown in Appendix B. A peak in the information flow can still be seen in such cases, but does not mark $\varepsilon_{\max}$.

For the cases seen in Fig. 9(b) where either C_1 or C_2 is the driven system, the exact value of $\varepsilon_{\max}$ could not be determined due to a noisy dependence already seen in Fig. 4(c). When these two systems are driven, their orbits can get stuck in a region of phase space for some time. This can have a seemingly random effect on the information flow, which results in the noisiness. The monotonicity could only be reliably shown up to a certain point where this noise started. In these cases, this point was taken as $\varepsilon_{\max}$.

Once a smooth function is obtained, the derivative in (15) is simple to calculate. Some examples of the information susceptibility and the obtained values of $\varepsilon_{\max}$ are shown in Fig. 10. The values of χ_I are always smaller in the cases of driven C_1, C_2 than for driven C_3, C_4, implying that these systems are less adaptable to the driving system.

Chaos ARTICLE scitation.org/journal/cha

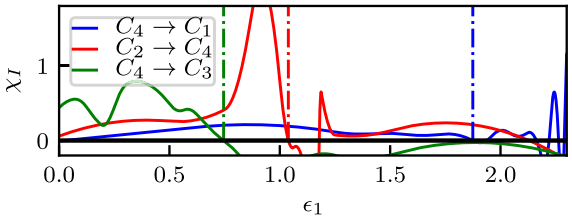

FIG. 10. Information susceptibility (15) for different systems. Dashed vertical lines mark the obtained values of ε_{max}.

Finally, we show the results for the solvability of the inverse problem in the limit of weak coupling in Table II. Only driven chaotic systems are considered, since the results for driven regular systems depend strongly on the partition of the phase space. Some properties of the individual systems and the information flow can be derived from the table.

Most notably, a difference between chaotic systems with a large and with a small nonlinear term is seen. For driven chaotic systems with a large nonlinear term, ε_{max} was mostly marked by the appearence of noise. Nevertheless, the values of ε_{max} are generally larger than for driven C_3, C_4. This means that C_1 and C_2 are harder to adapt to the driving system, which is also implied by the smaller values of information flow and information susceptibility. For driven C_3 or C_4, the noisy dependence was never observed and the values converged faster.

There are six cases in which ε_{max} is marked by bifurcations in the driven subsystem. In all these cases except $R_1 \to C_4$, there is a discrete jump in the information flow at the point of system change.

In summary, we have shown that the coupling parameter of most systems is uniquely determined by the information flow in the limit of weak coupling. In measured time series, the models of the measured systems are usually unknown and surrogate data are often needed to determine the direction of coupling. In coupled Duffing systems, we can determine both the direction and the magnitude of the coupling in the limit of weak coupling. This is possible because the model of the systems is known, or rather known not to change. Only the coupling parameter changes, while the other system parameters are kept constant. If this was known to be the case in a realistic system, inferring the direction as well as the magnitude of coupling might be feasible solely by calculating the information flow.

VI. CONCLUSION

One of the challenges in studying complex systems is to infer the coupling between individual systems from their time series. We studied the behavior of information-based coupling detection methods on coupled Duffing oscillator systems. The information flow successfully determined the direction of coupling between chaotic or regular systems. This was always possible for small coupling, and in most cases, also for large coupling.

To find the numerical properties, the convergence of CMI with the length of the time series and the dependence on different partitions were observed. The convergence was found to be faster than expected, and a finer partition to be generally beneficial as long as the individual bins are well populated.

While the absolute value of CMI is considered of little value in experimental data, we can analyze it thoroughly in mathematical models. Thus, we studied the dependence of CMI on the coupling parameter. We evaluated the usefulness of CMI in solving the inverse problem of inferring the coupling parameter. By defining the information susceptibility, we found that in some cases the coupling parameter is uniquely determined by the information flow. This is the case in the limit of strong coupling and, at least in some cases, in the limit of weak coupling. Although this knowledge cannot be applied to arbitrary experimental data, it might be possible if accurate models of the systems were known.

The inverse problem proved to be complex because bifurcations can occur when systems are coupled. The exact classification of systems for which it is solvable remains to be seen.

ACKNOWLEDGMENTS

M.B. and P.B. acknowledge financial support from the Slovenian Research Agency (Research Program No. P2–0001). M.H. acknowledges financial support from the Slovenian Research Agency (Research Program No. P1-0402 and Research Project No. J1-1698).

APPENDIX A: CONVERGENCE OF CMI

The expected convergence of histograms with time $p(t) = p_0 + At^{-C}$ is $C = 1/2$ for chaotic and $C = 1$ for regular systems. In Fig. 2, it was found that the convergence of the information flow is $C = 1$ for all systems. To find out why this is the case, we tested the convergence of different variables for the system $C_2 \to C_1$. For this test, we chose $\varepsilon_1 = 0$, since we expect CMI to converge close to 0.

TABLE II. Values of ε_{max} for various driven and driving systems. Cases where the monotonicity of the information flow in the low coupling regime could not be shown are marked with a question mark. Systems that exhibit non-continuous dependencies due to bifurcations are marked from 1 to 6 as a reference to the appendix where they are examined.

		Driving system					
		R_1	R_2	C_1	C_2	C_3	C_4
Driven system	C_1	$\varepsilon_{max} = 1.(0)$	$\varepsilon_{max} = 0.3(8)^1$		?	$\varepsilon_{max} = 1.(9)$	$\varepsilon_{max} = 1.(8)$
	C_2	$\varepsilon_{max} = 3.(9)$	$\varepsilon_{max} = 5.(4)$	?		$\varepsilon_{max} = 0.(9)$	$\varepsilon_{max} = 0.(7)$
	C_3	$\varepsilon_{max} = 0.0(4)$	$\varepsilon_{max} = 0.02(1)^5$	$\varepsilon_{max} = 0.02(3)^6$	$\varepsilon_{max} = 0.02(1)^3$		$\varepsilon_{max} = 0.7(4)$
	C_4	$\varepsilon_{max} = 0.3(2)^4$	$\varepsilon_{max} = 0.5(1)^2$	$\varepsilon_{max} = 0.4(7)$	$\varepsilon_{max} = 1.0(4)$	$\varepsilon_{max} = 0.5(8)$	

Chaos ARTICLE scitation.org/journal/cha

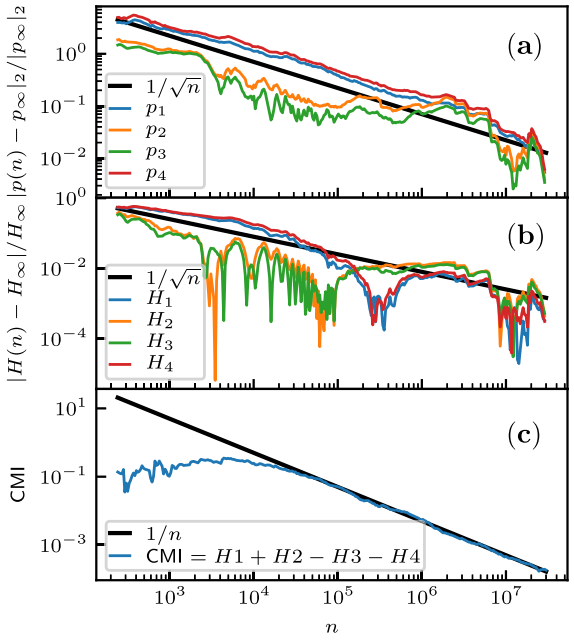

FIG. 11. The convergence of probabilities (a), entropies (b) and conditional mutual information (time-lagging C_2 with $\tau = 1$) (c) with the length of the time series n for the system $C_2 \to C_1$ with $\varepsilon_1 = 0$. The black lines are given to indicate the type of convergence.

We looked at the convergence of the conditional mutual information (8) toward 0, the four entropies involved in the calculation of CMI (10) and the probability distributions used to calculate these entropies. In Fig. 11, the probability distributions are denoted as p_1 to p_4 and the entropies as H_1 to H_4, according to the order in (10). The entropy H_3 has two arguments, the entropies H_1 and H_2 have four arguments, and the entropy H_4 has six arguments. The same holds for the corresponding distributions.

As expected, the empirical probability distributions p_i converge with $C = 1/2$. This was verified by treating the distributions as vectors and observing their convergence with increasing length of the series n in 2-norm $|\cdot|_2$. The converged values are denoted by p_∞ and H_∞. The entropies H_i also converge slower than with $C = 1$. However, taking the sum and difference of the entropies defining the information flow CMI, the convergence is evidently faster than the constituting terms with $C = 1$.

APPENDIX B: SYSTEMS WITH BIFURCATIONS

Some systems exhibit bifurcations, i.e., sudden qualitative changes in the system behavior caused by a small change in the coupling parameter ε_1. In such cases, observing the phase space and conditional Lyapunov exponents helps in understanding the dependence of the information flow and the solvability of the inverse problem.

1. System $R_2 \to C_1$

The information flow dependence, the CLE dependence, and the phase space portraits for the system $R_2 \to C_1$ are shown in Fig. 12. The inverse problem is solvable for $\varepsilon_1 \leq 0.38$, where the dynamics of the system change. The change can also be seen from smaller values of the CLE.

2. System $R_2 \to C_4$

The information flow dependence, the CLE dependence, and the phase space portraits for the system $R_2 \to C_4$ are shown in Fig. 13. In the regions $0.51 < \varepsilon_1 < 0.61$ and $\varepsilon_1 < 0.8$, the driven subsystem exhibits regular dynamics and the information flow takes higher values, while the CLE takes negative values. The inverse problem is solvable until the first appearance of regular dynamics at $\varepsilon_{\max} = 0.51$.

3. System $C_2 \to C_3$

The information flow dependence, the CLE dependence, and the phase space portraits for the system $C_2 \to C_3$ are shown in Fig. 14. The system dynamics change several times, the first time at $\varepsilon_{\max} = 0.021$. This is seen in an intense behavior of the information flow and the CLE values.

4. System $R_1 \to C_4$

The information flow dependence, the CLE dependence, and the phase space portraits for the system $R_1 \to C_4$ are shown in Fig. 15. The inverse problem is solvable up to $\varepsilon_{\max} = 0.32$, where the dynamics of the driven subsystem become regular, which is reflected in the negative values of the CLE. The driven subsystem becomes periodic with a period of exactly 100, i.e., $t_{period} = 100 \cdot 2\pi/\omega_1$.

5. System $R_2 \to C_3$

The information flow dependence, the CLE dependence, and the phase space portraits for the system $R_2 \to C_3$ are shown in Fig. 16. The dynamics of the driven subsystem become regular at $\varepsilon_{\max} = 0.022$, which is reflected in the negative values of the CLE.

6. System $C_1 \to C_3$

The information flow dependence, the CLE dependence, and the phase space portraits for the system $C_1 \to C_3$ are shown in Fig. 17. The dynamics of the driven subsystem become regular at $\varepsilon_{\max} = 0.023$, which is reflected in the negative values of the CLE.

Chaos ARTICLE scitation.org/journal/cha

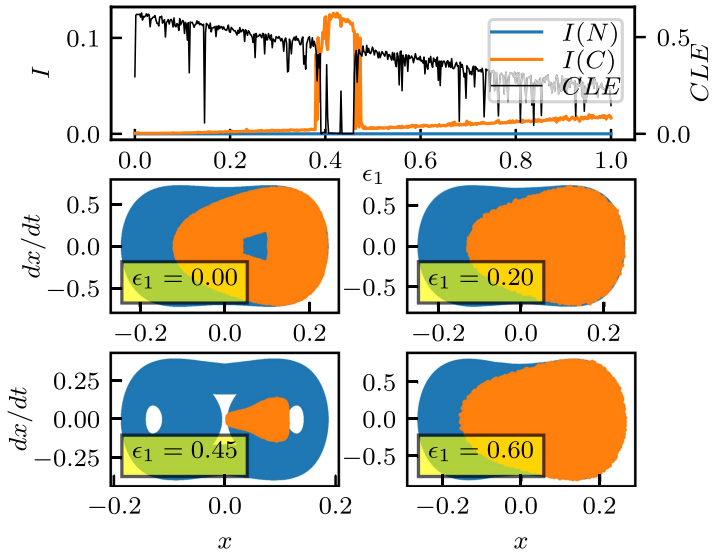

FIG. 12. The information flow and CLE dependences on the coupling parameter and the corresponding phase space portraits of the driven subsystem for $R_2 \to C_1$. The orange dots represent a stroboscopic map at $\cos(\omega_1 t) = 1$.

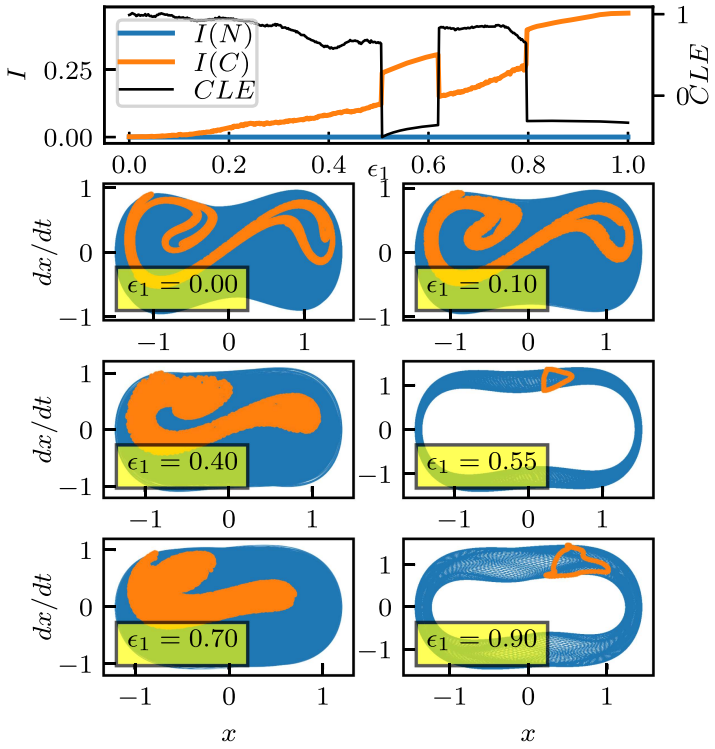

FIG. 13. The information flow and CLE dependences on the coupling parameter and the corresponding phase space portraits of the driven subsystem for $R_2 \to C_4$. The orange dots represent a stroboscopic map at $\cos(\omega_1 t) = 1$.

Chaos ARTICLE scitation.org/journal/cha

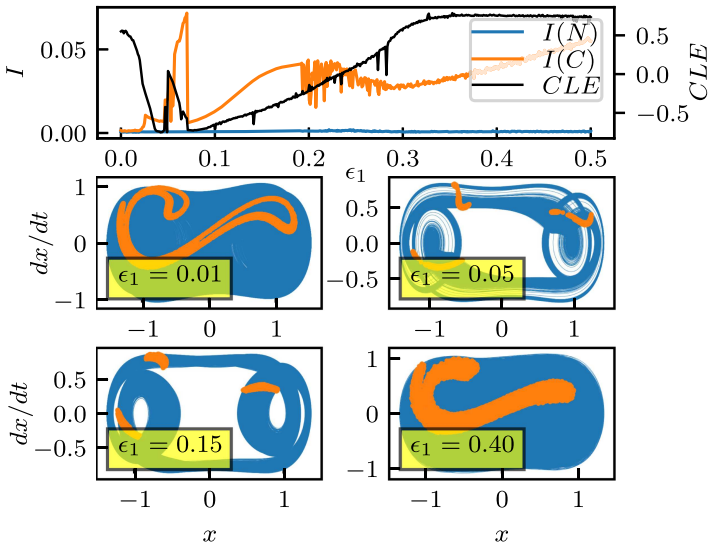

FIG. 14. The information flow and CLE dependences on the coupling parameter and the corresponding phase space portraits of the driven subsystem for $C_2 \to C_3$. The orange dots represent a stroboscopic map at $\cos(\omega_1 t) = 1$.

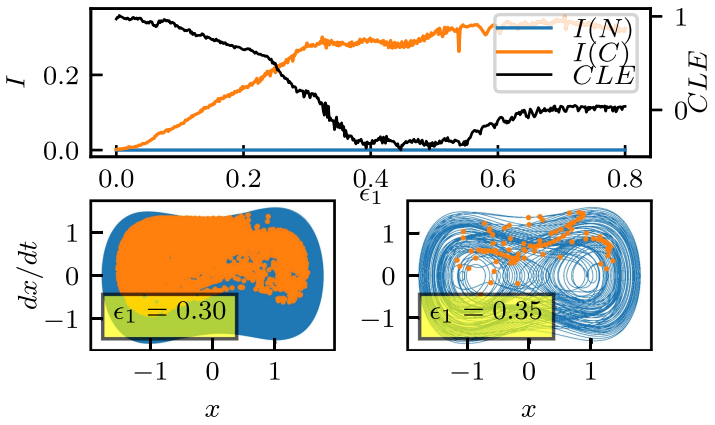

FIG. 15. The information flow and CLE dependences on the coupling parameter and the corresponding phase space portraits of the driven subsystem for $R_1 \to C_4$. The orange dots represent a stroboscopic map at $\cos(\omega_1 t) = 1$.

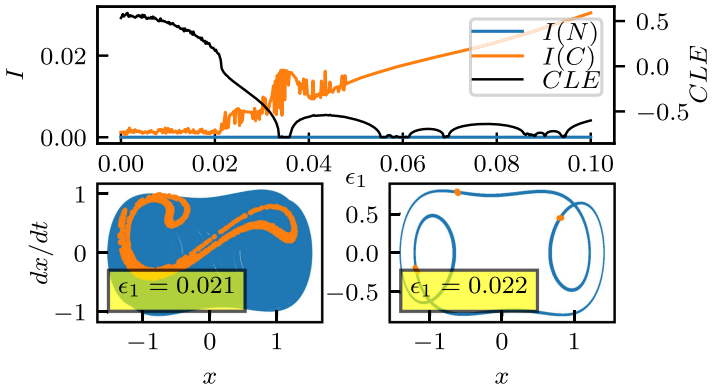

FIG. 16. The information flow and CLE dependences on the coupling parameter and the corresponding phase space portraits of the driven subsystem for $R_2 \to C_3$. The orange dots represent a stroboscopic map at $\cos(\omega_1 t) = 1$.

Chaos ARTICLE scitation.org/journal/cha

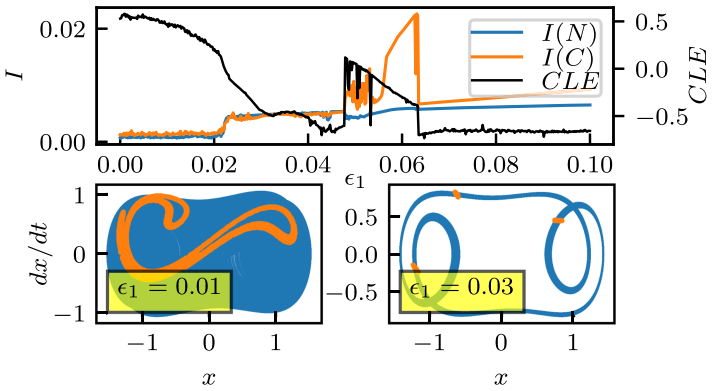

FIG. 17. The information flow and CLE dependences on the coupling parameter and the corresponding phase space portraits of the driven subsystem for $C_1 \rightarrow C_3$. The orange dots represent a stroboscopic map at $\cos(\omega_1 t) = 1$.

DATA AVAILABILITY

The data that support the analysis of this article have been generated by the authors and can be fully reproduced from the repository in Duffing CMI, https://repo.ijs.si/mbresar/duffing-cmi, Ref. 19.

REFERENCES

[1] J. A. T. Thomas M. Cover, *Elements of Information Theory* (John Wiley & Sons, 2006).
[2] P. Holmes, "A nonlinear oscillator with a strange attractor," Philos. Trans. R. Soc. Lond. Ser A Math. Phys. Sci. **292**, . 419–448 (1979).
[3] M. Paluš, V. Komárek, Z. Hrnčíř, and K. Štěrbová, "Synchronization as adjustment of information rates: Detection from bivariate time series," Phys. Rev. E **63**, 046211 (2001).
[4] B. Musizza, A. Stefanovska, P. V. E. McClintock, M. Paluš, J. Petrovčič, S. Ribarič, and F. F. Bajrovič, "Interactions between cardiac, respiratory and EEG-δ oscillations in rats during anaesthesia," J. Physiol. **580**, 315–326 (2007).
[5] M. Paluš and M. Vejmelka, "Directionality of coupling from bivariate time series: How to avoid false causalities and missed connections," Phys. Rev. E **75**, 056211 (2007).
[6] M. Paluš and A. Stefanovska, "Direction of coupling from phases of interacting oscillators: An information-theoretic approach," Phys. Rev. E **67**, 055201(R) (2003).
[7] P. T. Clemson and A. Stefanovska, "Discerning non-autonomous dynamics," Phys. Rep. **542**, 297–368 (2014).
[8] T. Schreiber, "Measuring information transfer," Phys. Rev. Lett. **85**, 461–464 (2000).
[9] D. A. Rand, *Dynamical Systems and Turbulence, Warwick 1980: Proceedings of a Symposium Held at the University of Warwick 1979-80* (Springer-Verlag, Berlin, 1981).
[10] M. G. Rosenblum, A. S. Pikovsky, and J. Kurths, "Phase synchronization of chaotic oscillators," Phys. Rev. Lett. **76**, 1804–1807 (1996).
[11] *The Duffing Equation*, edited by I. Kovacic and M. J. Brennan (John Wiley & Sons, Ltd, 2011).
[12] Y. Ueda, Randomly transitional phenomena in the system governed by Duffing's equation," J. Stat. Phys. **20**, 181–196 (1979).
[13] G. Benettin, L. Galgani, A. Giorgilli, and J.-M. Strelcyn, "Lyapunov characteristic exponents for smooth dynamical systems and for Hamiltonian systems: A method for computing all of them. part 2: Numerical application," Meccanica **15**, 21–30 (1980).
[14] M. Tarnopolski, "On the fractal dimension of the Duffing attractor," Rom. Rep. Phys. **66**, 907–917 (2013).
[15] L. M. Pecora and T. L. Carroll, "Synchronization of chaotic systems," Chaos **25**, 097611 (2015).
[16] M. Palus, "Linked by dynamics: Wavelet-based mutual information rate as a connectivity measure and scale-specific networks," in *Advances in Nonlinear Geosciences* (Springer, 2018), pp. 427–463.
[17] A. Pikovsky, M. Rosenblum, and J. Kurths, *Synchronization: A Universal Concept in Nonlinear Sciences*, Cambridge Nonlinear Science Series (Cambridge University Press, 2001).
[18] W. Härdle, M. Müller, S. A. Sperlich, and A. Werwatz, *Nonparametric and Semiparametric Models* (Springer, 2004).
[19] "Python code for studying coupling between Duffing systems with conditional mutual information," Duffing CMI, https://repo.ijs.si/mbresar/duffing-cmi.

Chapter 5

Improving the Accuracy of State Space Measures

The classical state space measures [5], [44], [46]–[48] can be used to determine the coupling direction when the coupling is weak enough so that the dynamics do not synchronize. However, they all have a significant drawback. In order to illustrate it, consider an analysis of the unidirectionally coupled Rössler systems with slightly offset frequencies

$$\begin{aligned}
\frac{dx_1}{dt} &= -0.99x_2 - x_3 + \varepsilon(y_1 - x_1) \\
\frac{dx_2}{dt} &= 0.99x_1 + 0.15x_2 \\
\frac{dx_3}{dt} &= 0.2 + x_3(x_1 - 10) \\
\frac{dy_1}{dt} &= -1.01y_2 - y_3 \\
\frac{dy_2}{dt} &= 1.01y_1 + 0.15y_2 \\
\frac{dy_3}{dt} &= 0.2 + y_3(y_1 - 10)
\end{aligned} \tag{5.1}$$

Figure 5.1 (a),(b),(c) shows the measures M, L, and ρ, respectively, obtained for different values of ε. One can see that the value of the measures' variants used to detect couplings $Y \to X$ increases when coupling strength increases, as is expected. However, the other variant used to detect couplings $X \to Y$ also increases, although to a lesser degree. This substantially decreases these measures' ability to determine the coupling direction for intermediate coupling strengths. This happens because these measures are influenced not only by couplings but also by other properties like linear cross-correlation.

This chapter presents original research conducted as part of this dissertation. It introduces a novel state space measure c, which significantly alleviates the drawback of the established state space measures. Let us discuss the idea behind it. Let X and Y be two dynamical systems with a unidirectional coupling $Y \to X$. Recall the cross-mapping property utilized by the state space measures: the close states of the response subsystem X are mapped to the close states of the driving subsystem Y, but not vice versa. Furthermore, recall the definition of the k-th conditioned nearest neighbor of $\boldsymbol{y}_i$, which is $\boldsymbol{y}_{P_i^X(k)}$ (Chapter 3.5.1), and the definition of the cross-distance matrix $D_{ij}^{Y \to X} = d(\boldsymbol{y}_i, \boldsymbol{y}_{P_i^X(j)})$ (Chapter 3.5.3).

The classical state space measures utilize the following. If a coupling $Y \to X$ exists, then because of the cross-mapping property, the first k conditioned nearest neighbors of $\boldsymbol{y}_i$

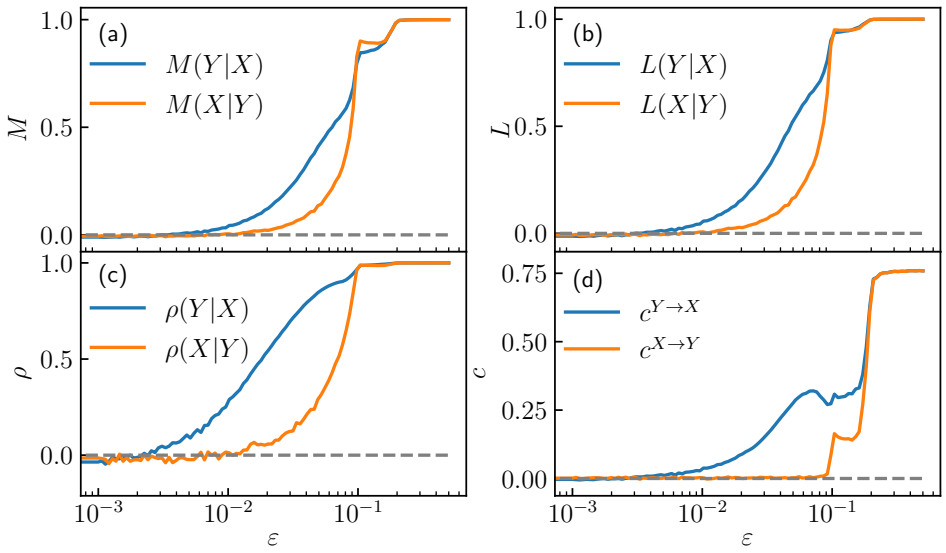

Figure 5.1: Values of the directional coupling measures M (a), L (b) ρ (c), and c (d), obtained for unidirectionally coupled Rössler systems (5.1) for 100 values of ε spaced equidistantly on a logarithmic scale. Solid lines represent the mean values of 100 realizations, and colored bands represent $\pm$ one standard deviation at each value of ε. The system is solved with random initial conditions with an integration step 0.01. Each realization's first 10^6 points are discarded to remove transients, and the rest are sampled at $\Delta t = 0.2$. Finally, 10^4 samples of each subsystem's first component are analyzed. The embedding parameters are $\tau = 1$, $m = 20$, and the Theiler correction window of $W = 50$ samples is used. The classical measures' nearest neighbor parameter is $k = 10$, and the c measure's parameters are $k_1 = 10, k_2 = 100$.

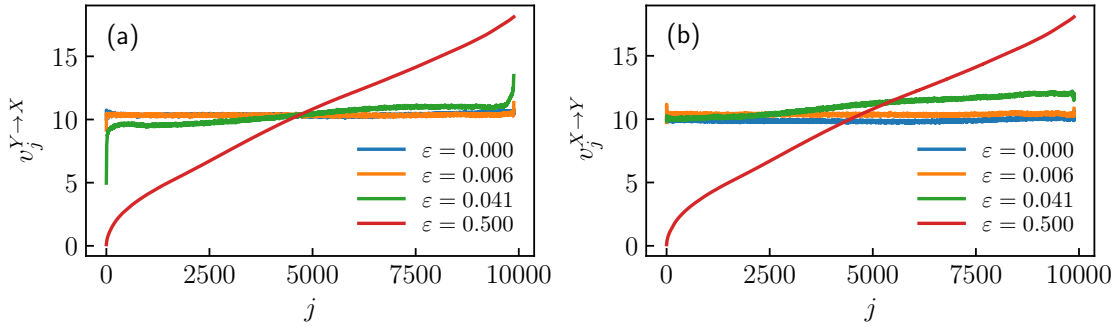

Figure 5.2: Plot of the values of components of the cross-distance vectors $v_j^{Y\to X}$ (a) and $v_j^{X\to Y}$ (b), obtained for realizations of the coupled Rössler systems (5.1) at four different values of the coupling strength ε.

are (on average) more similar to $\boldsymbol{y}_i$ than a random point $\boldsymbol{y}_l$ is. However, these measures do not consider *the dependence of the distance* $d(\boldsymbol{y}_i, \boldsymbol{y}_{P_i^X(k)})$ *on* k. This dependence can be observed by computing the *cross-distance vectors*, defined as the mean of the rows of

the cross-distance matrix [64]

$$\boldsymbol{v}^{Y\to X},\, v_j^{Y\to X} = \frac{1}{N}\sum_{i=1}^{N} D_{ij}^{Y\to X}. \tag{5.2}$$

The j-th component $v_j^{Y\to X}$ quantifies the average distance (average over all $\boldsymbol{y}_i$) from $\boldsymbol{y}_i$ to its j-th conditioned nearest neighbor. In general, one might expect $v_j^{Y\to X}$ to be a linear, a sigmoid, or any other increasing function of j. However, the main effect of a coupling $Y \to X$ on this vector turns out to be the appearance of an initial tail, while the bulk of the vector can have different trends regardless of coupling. This is seen in Figure 5.2. Contrary to the classical state space measures, the new measure c presented in this chapter takes into account this dependence by quantifying the prominence of the initial tail of the cross-distance vectors. It is defined as

$$c^{Y\to X} = \frac{V_{k_1+1:k_2}^{Y\to X} - V_{1:k_1}^{Y\to X}}{V_{1:k_2}^{Y\to X}}, \tag{5.3}$$

where $V_{i:j}^{Y\to X} = \frac{1}{j-i+1}\sum_{h=i}^{j} v_h^{Y\to X}$. The choice of k_1 and k_2 is not very important, but both have to be much smaller than the time series length. In this dissertation, $k_1 = 10$ and $k_2 = 100$ is used.

Figure 5.1 (d) shows the measure c obtained for the coupled Rössler systems for different values of ε. Let us compare the behaviour of c and the behaviour of the classical state space measures M, L, and ρ. Recall that the coupling direction is $Y \to X$. Note that the values of $c^{Y\to X}$ increase with increased ε much like the other measures' variants used to detect a coupling $Y \to X$. However, the measure $c^{X\to Y}$ starts increasing from zero at $\varepsilon \approx 0.1$, while the other three measures' variants used to detect a coupling $X \to Y$ start increasing already at $\varepsilon \approx 0.01$. This shows the advantage of c over other state space measures. It is able to more accurately determine the coupling direction over a wider range of coupling strengths with a decreased risk of false detection. All results from this study can be fully reproduced using the code available at `https://repo.ijs.si/e2pub/cd-vec`.

5.1 A Distance-Based Measure with Improved Accuracy

PHYSICAL REVIEW E **107**, 044220 (2023)

Directional coupling detection through cross-distance vectors

Martin Brešar*
Jožef Stefan Institute, Jamova cesta 39, SI-1000 Ljubljana, Slovenia
and Jožef Stefan International Postgraduate School, Jamova cesta 39, SI-1000 Ljubljana, Slovenia

Pavle Boškoski
Jožef Stefan Institute, Jamova cesta 39, SI-1000 Ljubljana, Slovenia

(Received 5 December 2022; accepted 3 April 2023; published 27 April 2023)

Inferring the coupling direction from measured time series of complex systems is challenging. We propose a state-space-based causality measure obtained from *cross-distance vectors* for quantifying interaction strength. It is a model-free noise-robust approach that requires only a few parameters. The approach is applicable to bivariate time series and is resilient to artefacts and missing values. The result is two *coupling indices* that quantify coupling strength in each direction more accurately than the already established state-space measures. We test the proposed method on different dynamical systems and analyze numerical stability. As a result, a procedure for optimal parameter selection is proposed, circumventing the challenge of determining the optimal embedding parameters. We show it is robust to noise and reliable in shorter time series. Moreover, we show that it can detect cardiorespiratory interaction in measured data. A numerically efficient implementation is available at https://repo.ijs.si/e2pub/cd-vec.

DOI: 10.1103/PhysRevE.107.044220

I. INTRODUCTION

Complex systems found in nature can often be considered as many interacting subsystems. Subsystems are often inherently connected and cannot be considered isolated from each other, which raises the question of how they interact with each other. In this article, we propose a method that belongs to the family of state-space distance approaches. It is capable of detecting and quantifying interactions in a computationally efficient way. It can be applied to bivariate time series to quantify the coupling strength in both directions. Furthermore, it is applicable to both linear and nonlinear coupling.

When considering two subsystems, there are four possibilities for the direction of their interaction. They can be independent, unidirectionally coupled (in either direction), or bidirectionally coupled. Another property often of interest is the nature of coupling, e.g., linear or nonlinear. Additionally, the coupling can be time-dependent, which poses a new problem in detecting it. The problem becomes even more complex in the case of more than two subsystems.

Typically, we measure a subsystem. For example, consider the system of a human body. We can characterize the cardiac subsystem by measuring the heart's electrical activity with an electrocardiogram. By performing such measurements for each subsystem, we obtain time series. The goal is to infer the direction and the nature of the interactions between the subsystems from measured time series.

This article shows that the proposed coupling indices can infer the coupling direction for various regular and chaotic systems. It can quantify the coupling strength in both directions for unidirectional or bidirectional coupling. It turns out to be noise robust and also efficient for shorter time series. Most importantly, compared to the most prominent state-space approaches, the proposed indices more accurately and reliably detect the coupling direction. We discuss the possible pitfalls of state-space approaches in detail. We present an in-depth analysis of the behavior of the proposed quantities. As a result, we propose a procedure of selecting optimal parameter values, thus achieving a robust performance. In such a way, we circumvent the problem of optimal embedding parameters selection. Additionally, we present a means of dealing with artefacts or missing values. Finally, we test the effectiveness of the approach on measured cardiorespiratory data.

Related work

Identifying causal relationships arises in different fields that deal with complex systems. For this purpose, different methods for detecting coupling between subsystems are being developed. Some of the most widely used are Granger causality, information theory, phase dynamics, and state-space methods. Prominent examples of areas where they are applicable are physiology [1,2], neuroscience [3], earth system sciences [4], ecology [5,6], and economics [7,8].

A brief overview of coupling detection methods is given below. For a more comprehensive overview of the available approaches, the prospective reader is referred to the overviews [9,10] and references therein.

*martin.bresar@ijs.si

Granger causality. Coupling detection methods often follow the idea of Granger causality [7]. The method in the original work is based on fitting a vector autoregressive model. Based on this idea, numerous other methods were proposed, such as partial directed coherence [11], which is a multivariate frequency approach to the original Granger causality.

Information transfer. A widely used family of methods for studying interactions is based on information theory. Most commonly studied is the transfer entropy [12], which quantifies information transfer from one subsystem to another. It is mathematically equivalent to conditional mutual information [13]. It is a model-free method that can detect both linear and nonlinear coupling. Entropy methods rely on estimating multidimensional probability distributions, which can be challenging for shorter time series.

Phase dynamics. For oscillatory systems, methods based on the oscillation phase can be used. Rosenblum and Pikovsky [14] proposed a method for quantifying asymmetry in the interaction between two oscillating subsystems. Phase transformation can be used together with information measures to more accurately quantify information flow between oscillators [15]. Time-frequency approaches can also be used, such as wavelet phase coherence [16] for detecting linear interactions, and wavelet bispectral analysis [17] for detecting nonlinear interactions.

State-space methods. In weakly coupled bivariate systems, close states of the driven subsystem are mapped to close states of the driving subsystem. The opposite effect is much smaller. Different methods quantifying this effect in both directions have been proposed [18–20].

Bivariate versus multivariate. An important distinction is between bivariate and multivariate methods. In the case of more than two interacting subsystems, all of them must be accounted for when analyzing interactions. This necessity led to the multivariate approach of many of the mentioned approaches. Partial Granger causality [21] is an extension to the Granger causality that excludes the effects of latent variables. Causation entropy [22] is a measure similar to transfer entropy that considers multiple variables. Multivariate methods, however, often lead to the curse of dimensionality, which means the estimation of multivariate measures becomes increasingly problematic with an increasing dimension of the measured system.

II. CROSS-DISTANCE VECTORS

Consider a pair of unidirectionally coupled subsystems $\boldsymbol{x}(t) = (x_1(t), \ldots, x_{n_x}(t))$ and $\boldsymbol{y}(t) = (y_1(t), \ldots, y_{n_y}(t))$. If the coupling direction is $y \to x$, their time evolution is described by

$$\frac{d\boldsymbol{x}(t)}{dt} = \boldsymbol{f}(\boldsymbol{x}, t) + \boldsymbol{g}(\boldsymbol{x}, \boldsymbol{y}), \tag{1a}$$

$$\frac{d\boldsymbol{y}(t)}{dt} = \boldsymbol{h}(\boldsymbol{y}, t), \tag{1b}$$

where $\boldsymbol{g}(\boldsymbol{x}, \boldsymbol{y})$ is the coupling function. We consider time-independent coupling functions, though they generally can depend on time. Our goal is to define a measure for the magnitude and direction of coupling from the observed time series. For $\boldsymbol{g}(\boldsymbol{x}, \boldsymbol{y}) \neq 0$, the subsystems, and therefore their trajectories, are not independent.

The trajectories of both subsystems $\boldsymbol{x}(t)$ and $\boldsymbol{y}(t)$ are observed at equally spaced times $t_i = t_0 + i\Delta t$ for $i \in \mathbb{Z}$. Thus, we obtain time series of these trajectories $[\boldsymbol{x}(t_i) : i \in \mathbb{Z}]$ and $[\boldsymbol{y}(t_i) : i \in \mathbb{Z}]$. We assume that Δt is sufficiently small to capture all the necessary information. The influence of Δt and potential downsampling are described in detail in Sec. IV E. Furthermore, we assume that the signals do not contain any trends, no commensurate frequency components, and other trivial artefacts that can be easily removed by a simple preprocessing.

Most often, only one dimension of a subsystem is measured. Thus, a single time series of length N is obtained. Therefore, we consider time series of one-dimensional values and omit the bold notation.

We split the time series into segments of length L. There are a total of $N - L + 1$ segments for each time series. Segments at a time moment t_i are defined as

$$\boldsymbol{o}_i^x = (x(t_i), x(t_{i+1}), \ldots, x(t_{i+L-1})), \tag{2}$$

$$\boldsymbol{o}_i^y = (y(t_i), y(t_{i+1}), \ldots, y(t_{i+L-1})). \tag{3}$$

Furthermore, let us assume a measure of the similarity of two segments, i.e., a distance between two vectors

$$d\left(\boldsymbol{o}_i^x, \boldsymbol{o}_j^x\right) = \left\|\boldsymbol{o}_i^x - \boldsymbol{o}_j^x\right\|. \tag{4}$$

We ask two questions:

(i) If two segments of the driven subsystem $\boldsymbol{o}_i^x$ and $\boldsymbol{o}_j^x$ at times t_i and t_j are similar, are the segments at those times of the driving subsystem $\boldsymbol{o}_i^y$ and $\boldsymbol{o}_j^y$ also similar?

(ii) Inversely, if two segments of the driving subsystem $\boldsymbol{o}_i^y$ and $\boldsymbol{o}_j^y$ at times t_i and t_j are similar, are the segments at those times of the driven subsystem $\boldsymbol{o}_i^x$ and $\boldsymbol{o}_j^x$ also similar?

To clarify, we ask whether the following statements are true in the coupling direction $y \to x$:

$$\text{(i)} \quad d\left(\boldsymbol{o}_i^x, \boldsymbol{o}_j^x\right) \approx 0 \Rightarrow d\left(\boldsymbol{o}_i^y, \boldsymbol{o}_j^y\right) \approx 0, \tag{5}$$

$$\text{(ii)} \quad d\left(\boldsymbol{o}_i^y, \boldsymbol{o}_j^y\right) \approx 0 \Rightarrow d\left(\boldsymbol{o}_i^x, \boldsymbol{o}_j^x\right) \approx 0. \tag{6}$$

It is well known that statement (5) is *true* and (6) is *false* for weakly coupled oscillators [18]. We provide an explanation of why this is the case for different subsystems in Appendix A. State-space methods take advantage of this property to infer the coupling direction from measured time series. In what follows, we propose a measure that quantifies coupling strength in each direction more accurately than the already established state-space indices.

A. Cross-distance vector algorithm

First, we construct segments (2) and (3) and choose a distance measure (4). In this article, we use

$$d\left(\boldsymbol{o}_i^x, \boldsymbol{o}_j^x\right) = \sqrt{\frac{1}{L}\sum_{m=1}^{L}(x(t_{i+m-1}) - x(t_{j+m-1}))^2}. \tag{7}$$

Next, we construct the distance matrix

$$\boldsymbol{D}^x, D_{ij}^x = d\left(\boldsymbol{o}_i^x, \boldsymbol{o}_j^x\right) \tag{8}$$

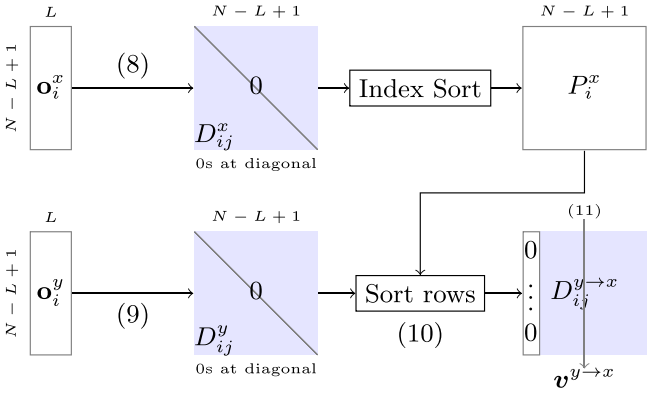

FIG. 1. Schematic representation of the algorithm for calculating the cross-distance vector $\boldsymbol{v}^{y\to x}$ in (11).

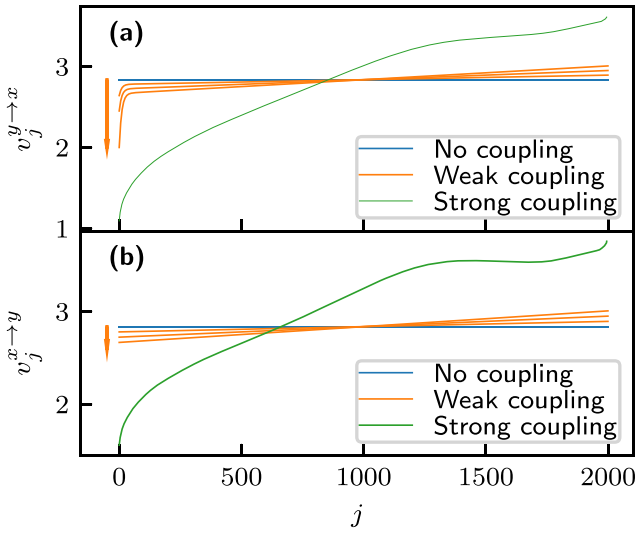

FIG. 2. A generic example of the behavior of cross-distance vectors $\boldsymbol{v}^{y\to x}$ and $\boldsymbol{v}^{x\to y}$ in different limits of the coupling strength. The direction of coupling in the example is $y \to x$. The orange arrows represent increasing coupling strength for the three weak-coupling examples. Note the appearance of tails in the beginning of $\boldsymbol{v}^{y\to x}$, but not in $\boldsymbol{v}^{x\to y}$.

of size $(N - L + 1) \times (N - L + 1)$, which contains the distances between all pairs of segments. We similarly calculate the distance matrix of the other time series,

$$\boldsymbol{D}^y, D_{ij}^y = d\left(\boldsymbol{o}_i^y, \boldsymbol{o}_j^y\right). \tag{9}$$

The goal is to rearrange the ith row of $\boldsymbol{D}^y$ in the same order as if the ith row of $\boldsymbol{D}^x$ was to be sorted in ascending order. This is achieved by calculating an index permutation P_i^x so that the ith row is sorted in ascending order under that permutation. We do this for every row and obtain $N - L + 1$ permutations.

Now, we sort the ith row of $\boldsymbol{D}^y$ according to the permutation P_i^x for all rows, and we obtain the matrix

$$\boldsymbol{D}^{y\to x}, D_{ij}^{y\to x} = D_{i,P_i^x(j)}^y \ . \tag{10}$$

This matrix highlights whether segments of y are similar at times at which segments of x are similar. For example, if the first few elements of the ith row of matrix (10) are the smallest entries in that row, this indicates that statement (5) is true. To evaluate this for all rows, we finally average out the rows of the matrix to obtain the *cross-distance vector*

$$\boldsymbol{v}^{y\to x}, v_j^{y\to x} = \frac{1}{N - L + 1} \sum_i D_{ij}^{y\to x}. \tag{11}$$

Similarly, we calculate the matrix $\boldsymbol{D}^{x\to y}$ and the vector $\boldsymbol{v}^{x\to y}$ by inverting the roles of x and y. The vector $\boldsymbol{v}^{y\to x}$ can be used to assess the truth of statement (5) and thus detect coupling in the direction $y \to x$. Conversely, the vector $\boldsymbol{v}^{x\to y}$ can be used to assess the truth of statement (6) and thus detect coupling in the direction $x \to y$. The complete algorithm is schematically shown in Fig. 1.

It should be noted that the first entry $v_0^{y\to x}$ of cross-distance vectors (11) will always be precisely zero due to zero diagonals of the distance matrices. So, $v_1^{y\to x}$ is the first nonzero entry. In the subsequent analysis, we will always omit the zero values in graphs.

B. Coupling index

We can define two *coupling indices* to quantify coupling strength in each direction. Ideally, an index is zero when there is no coupling and increases with increased coupling. Let us again consider unidirectionally coupled subsystems (1). Mind that the coupling direction is $y \to x$, i.e., x is the driven subsystem and y is the driving subsystem. Consider three limits of the coupling strength: no coupling, weak coupling, and strong coupling. The general behavior of cross-distance vectors in these limits is shown in Fig. 2.

The two subsystems $\boldsymbol{x}$ and $\boldsymbol{y}$ are independent if there is no coupling, i.e., $\boldsymbol{g}(\boldsymbol{x}, \boldsymbol{y}) = 0$ in (1a). Therefore, one subsystem's sorting permutation P_i^x is random for the subsystem y, and the cross-distance vector (11) is expected to be roughly constant. In the limit of infinite time series, both $\boldsymbol{v}^{y\to x}$ and $\boldsymbol{v}^{x\to y}$ will be constant. There are examples in which this is not the case (e.g., uncoupled subsystems that contain an oscillatory component with the same frequency), but these are exceptions.

In the limit of strong coupling, the term $\boldsymbol{g}(\boldsymbol{x}, \boldsymbol{y})$ in (1a) causes the subsystems to synchronize. In this case, the cross-distance vectors generally cannot be used to infer the coupling direction.

If there is *weak coupling* in the direction $y \to x$, the values of $\boldsymbol{v}^{y\to x}$ change significantly from a constant since statement (5) is true. The beginning of $\boldsymbol{v}^{y\to x}$ decreases [note the initial tails in Fig. 2(a)]. Apart from this initial tail, the bulk of $\boldsymbol{v}^{y\to x}$ remains roughly constant (though often gains an increasing trend). Conversely, the other cross-distance vector $\boldsymbol{v}^{x\to y}$ stays roughly constant without the initial tail since statement (6) is false. This is shown in Fig. 2(b).

The *decrease in the initial values of* $\boldsymbol{v}^{y\to x}$ is what allows us to detect the coupling direction from the cross-distance vectors, since the tail is present due to the term $\boldsymbol{g}(\boldsymbol{x}, \boldsymbol{y}) \neq 0$ in Eq. (1a). Note that if a similar term also exists in (1b) (which means that coupling is bidirectional), the initial values of both cross-distance vectors $\boldsymbol{v}^{y\to x}$ and $\boldsymbol{v}^{x\to y}$ exhibit an initial tail. To obtain the coupling indices, i.e., two values quantifying the detected coupling strength in each direction, we must somehow quantify this effect. While this can be done in different ways, we propose a simple but effective approach.

We define the coupling index $c^{y\to x}$, which quantifies coupling strength in the direction $y \to x$, as the normalized difference between the means of $v_j^{y\to x}$ for small j and for larger j,

$$c^{y\to x} = \frac{V_{k_1+1:k_2}^{y\to x} - V_{1:k_1}^{y\to x}}{V_{1:k_2}^{y\to x}}, \tag{12}$$

where

$$V_{i:j}^{y\to x} = \frac{1}{j-i+1}\sum_{k=i}^{j} v_k^{y\to x}. \tag{13}$$

The possible range of k_1 and k_2 is $1 \leqslant k_1 < k_2 \leqslant N - L$.

To quantify coupling strength in the other direction, we calculate $c^{x\to y}$ by swapping x and y. Defined in this way, coupling indices are *zero in the absence of coupling* and *increase with increasing coupling strength* (at least in the limit of weak coupling). Due to normalization, indices will roughly range from 0 to 1. They can be slightly negative if there is no coupling due to finite time series, as seen in most examples in this article. This is, however, not a problem, as a negative index can be taken as a strong indicator of the absence of coupling.

The purpose of Eq. (12) is to quantify the prominence of the initial tail. The parameter k_1 defines the part of $\boldsymbol{v}^{y\to x}$ that includes only the initial tail. Conversely, k_2 defines the subsequent part, where the rate of increase of $\boldsymbol{v}^{y\to x}$ is significantly smaller.

One might argue that this selection is arbitrary. Other options, such as kurtosis, could be explored to quantify the prominence of the initial tail. For simplicity, we quantify coupling strength with (12) in the subsequent analysis.

Related state space causality measure. From the family of the state-space approaches, our index (12) is closest to $M(Y|X)$ [19]. It will therefore be compared to and used as a benchmark to test the reliability of the proposed indices c. Using our notation, $M(Y|X)$ is defined as

$$M(Y|X) = \frac{1}{N-L+1}\sum_{i=1}^{N-L+1}\frac{R_i(Y) - R_i^k(Y|X)}{R_i(Y) - R_i^k(Y)}, \tag{14}$$

where

$$R_i(Y) = \frac{1}{N-L}\sum_{j=1, j\neq i}^{N-L+1} D_{ij}^{y}, \tag{15a}$$

$$R_i^k(Y) = \frac{1}{k}\sum_{j=2}^{k+1} D_{ij}^{y\to y}, \tag{15b}$$

$$R_i^k(Y|X) = \frac{1}{k}\sum_{j=2}^{k+1} D_{ij}^{y\to x}. \tag{15c}$$

Roughly speaking, $M(Y|X)$ quantifies the mean of the initial tail of $\boldsymbol{v}^{y\to x}$ compared to the mean of the whole vector, which is highly influenced by possible trends in the vector. This undesired property is also present in other state-space measures. On the other hand, the indices (12) quantify only the prominence of the initial tail, *ignoring possible trends* and thus resulting in smaller values in the direction without coupling, which is desired.

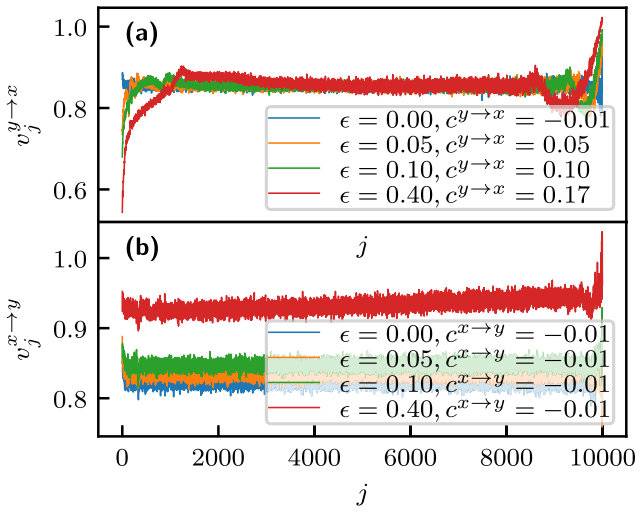

FIG. 3. The cross-distance vectors for the system of two coupled harmonic oscillators (18). The system parameters are $\omega_1 = 0.83$, $\omega_2 = 2.11$, the time series parameters are $N = 10^4$, $\Delta t = 0.05$, the segment length is $L = 10$, and the coupling index parameters are $k_1 = 100$, $k_2 = 1000$.

C. An example

Consider the system of analytically solvable unidirectionally coupled harmonic oscillators,

$$\ddot{x} = -\omega_1^2 x + \epsilon(y - x), \tag{16}$$

$$\ddot{y} = -\omega_2^2 y. \tag{17}$$

The coupling direction is $y \to x$. The solutions to these equations are oscillations with frequencies ω_2 and $\sqrt{\omega_1^2 + \epsilon}$. For example, given the initial conditions $x(0) = 1$, $\dot{x}(0) = 0$, $y(0) = 1$, $\dot{y}(0) = 0$, the solution is

$$x(t) = \frac{1}{\epsilon + \omega_1^2 - \omega_2^2}\Big(\epsilon\cos(\omega_2 t) + \big(\omega_1^2 - \omega_2^2\big)\cos\Big(\sqrt{\epsilon + \omega_1^2}\,t\Big)\Big),$$

$$y(t) = \cos(\omega_2 t). \tag{18}$$

Since we have the analytical solution, we can verify statements (5) and (6) directly.

Two segments of x will be similar when the phases of both of its oscillatory components will match, one of them being $\cos(\omega_2 t)$. Since this is also the component of $y(t)$, its segments at those times will also be similar. This confirms that the statement (5) is indeed *true*.

If two segments of $y(t)$ are similar, the phase of only one oscillatory component of $x(t)$ will match. In contrast, the phase of the other component can take any value [unless the frequencies of the components of $x(t)$ are commensurable, which is an exception]. This confirms that the statement (6) is indeed *false*.

Numerically calculated cross-distance vectors are shown in Fig. 3. As expected, the beginning of $\boldsymbol{v}^{y\to x}$ is significantly smaller than the bulk [Fig. 3(a)], and $\boldsymbol{v}^{x\to y}$ stays roughly constant at nonzero coupling [Fig. 3(b)].

Additionally, Fig. 3 shows that the coupling index of the direction of coupling $c^{y\to x}$ increases with increased coupling parameter ϵ. In contrast, the coupling index in the direction without coupling $c^{x\to y}$ remains roughly constant. By simply comparing the values, we can correctly determine the coupling direction.

We also notice that the end of $\boldsymbol{v}^{y\to x}$ has larger values than the bulk of the vector, which indicates that a statement similar to (5) is also true for dissimilarity: if two segments at times t_i and t_j of the driven subsystem are very dissimilar, the segments at these times of the driving subsystem are more likely also to be dissimilar. This opposite effect is, however, not as expressed and does not appear in all systems.

When numerically calculating the cross-distance vectors, we added Gaussian noise $\mathcal{N}(0, \sigma^2 = 10^{-4})$ to the time series. In noiseless periodic systems, cross-distance vectors can exhibit periodic oscillations. By adding small noise, they disappear, and the vectors behave the same as in chaotic systems. We still used this example due to the availability of the analytical solution. In practice, periodic systems are of lesser interest and always contain noise.

In the following section, we will present a numerical analysis that shows that cross-distance vectors can be used to determine the direction of coupling in different systems.

III. DIFFERENT SYSTEMS ANALYSIS

The previous section shows that the cross-distance vectors can detect the coupling direction in the coupled harmonic oscillators system. Here, we will show that detection is possible not only for regular subsystems but also for discrete chaotic subsystems and for autonomous and nonautonomous continuous chaotic subsystems. For an overview on chaotic dynamical systems, the reader is referred to [23,24]. We chose systems that have already been analyzed with a coupling detection method. The indices $M(Y|X)$ and $M(X|Y)$ will be shown next to $c^{y\to x}$ and $c^{x\to y}$. At the end of this section, these two methods will be compared.

A. Hénon maps

The Hénon map is a discrete-time dynamical system. Based on the values of its two parameters a and b, it can be chaotic or converge to a periodic orbit. We choose the most commonly studied map with parameter values $a = 1.4$ and $b = 0.3$, which yield chaotic dynamics. Two unidirectionally coupled maps are defined by four equations. The driven subsystem is described by

$$x_1' = a - \left(\epsilon x_1 y_1 + (1-\epsilon)x_1^2\right) + b x_2, \tag{19}$$

$$x_2' = x_1, \tag{20}$$

and the driving one by

$$y_1' = a - y_1^2 + b y_2, \tag{21}$$

$$y_2' = y_1. \tag{22}$$

The coupling direction is $y \to x$. This system was analyzed in [25]. We choose time-series length $N = 2 \times 10^4$ and segment length $L = 10$. The cross-distance vectors at a few values of the coupling parameter ϵ are shown in Fig. 4. They behave as expected. In the absence of coupling, they are both constant. For weak coupling, the initial values of $\boldsymbol{v}^{y\to x}$ decrease with increased coupling, while this does not happen with $\boldsymbol{v}^{x\to y}$. For strong coupling, both $\boldsymbol{v}^{y\to x}$ and $\boldsymbol{v}^{x\to y}$ lose the straight shape, and the coupling direction cannot be inferred from them.

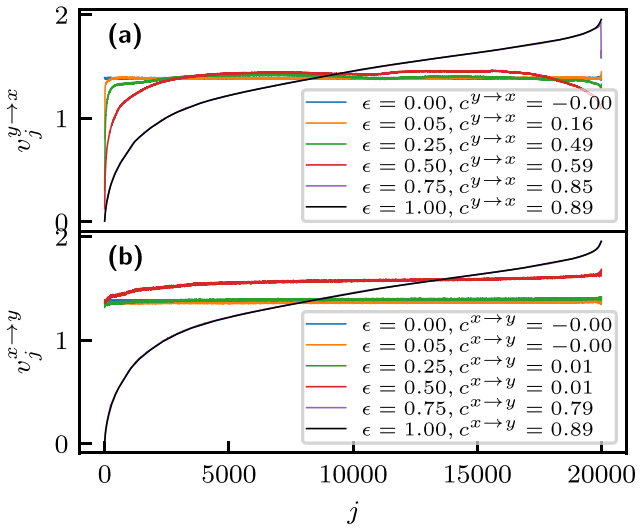

FIG. 4. The cross-distance vectors for unidirectionally coupled Hénon maps at different values of the coupling parameter ϵ. They are obtained from the time series of the subsystems' coordinates x_1 and y_1 and with segment length $L = 10$.

The dependence of the coupling indices $c^{x\to y}$ and $c^{y\to x}$ on the coupling parameter ϵ is shown in Fig. 5(a). In the absence of coupling, both coupling indices are close to zero. With increased coupling, $c^{y\to x}$ increases for small values of ϵ. The other coupling index $c^{x\to y}$ is close to zero until the

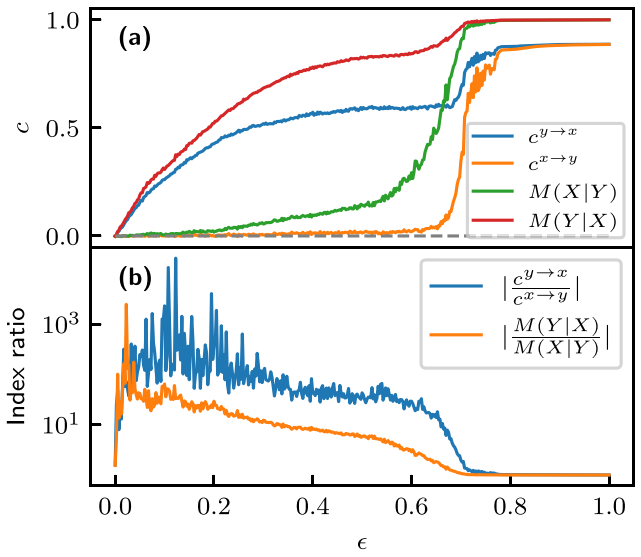

FIG. 5. The indices $c^{y\to x}$, $c^{x\to y}$, $M(Y|X)$, and $M(X|Y)$ (a), and index ratios (b) for unidirectionally coupled Hénon maps at different values of the coupling parameter ϵ. The coupling indices c were calculated by (12) with $k_1 = 10, k_2 = 100$, and the indices M were calculated by (14) with $k = 10$.

synchronization threshold at $\epsilon \approx 0.75$. Therefore, the cross-distance vectors can be used to infer the coupling direction in unsynchronized Hénon maps correctly.

B. Rössler systems

The Rössler system is a system of three nonlinear ordinary differential equations, which define a chaotic continuous-time dynamical system. Two coupled Rössler subsystems are defined by six equations. We chose the same parameters for the subsystems as in [13]. The driven subsystem is thus described by

$$\dot{x}_1 = -0.985x_2 - x_3 + \epsilon(y_1 - x_1), \tag{23}$$

$$\dot{x}_2 = 0.985x_1 + 0.15x_2, \tag{24}$$

$$\dot{x}_3 = 0.2 + x_3(x_1 - 10), \tag{25}$$

and the driving subsystem is described by

$$\dot{y}_1 = -1.015y_2 - y_3, \tag{26}$$

$$\dot{y}_2 = 1.015y_1 + 0.15y_2, \tag{27}$$

$$\dot{y}_3 = 0.2 + y_3(y_1 - 10). \tag{28}$$

Coupling is unidirectional in the direction $y \to x$. It should be noted that the first subsystem is in a regular regime for $\epsilon = 0$, and in a chaotic regime for $\epsilon > 0$, while the second subsystem is always chaotic. Therefore, we omit analysis at zero coupling.

Time-series parameters are $N = 2 \times 10^4$, $\Delta t = 0.5$. The system integration was done with the Runge-Kutta 4 integrator with time step 0.01. We choose the time series of the subsystems' coordinates x_1 and y_1 and segment length $L = 20$ for the calculation of the cross-distance vectors.

The behavior of the cross-distance vectors for a few values of the coupling parameter ϵ is shown in Fig. 6. It is similar to the examples seen so far. For weak coupling, the initial values of $\boldsymbol{v}^{y\to x}$ decrease from the bulk, while $\boldsymbol{v}^{x\to y}$ stays roughly constant. For strong coupling, both subsystems become identical, and so do both cross-distance vectors.

The dependence of the coupling indices $c^{x\to y}$ and $c^{y\to x}$ on the coupling parameter ϵ is shown in Fig. 7(a). Similar to the previous example, $c^{y\to x}$ increases with increased coupling strength while $c^{x\to y}$ stays close to zero. At $\epsilon \approx 0.15$, synchronization occurs, and the coupling direction can no longer be inferred from the coupling indices.

This analysis shows that the cross-distance vectors can again be used to infer the coupling direction in unsynchronized Rössler subsystems correctly.

C. Duffing systems

The Duffing system is a periodically forced nonlinear oscillator with damping. It is a nonautonomous continuous-time dynamical system. It can exhibit chaotic or periodic dynamics based on the values of its parameters. We chose the parameters

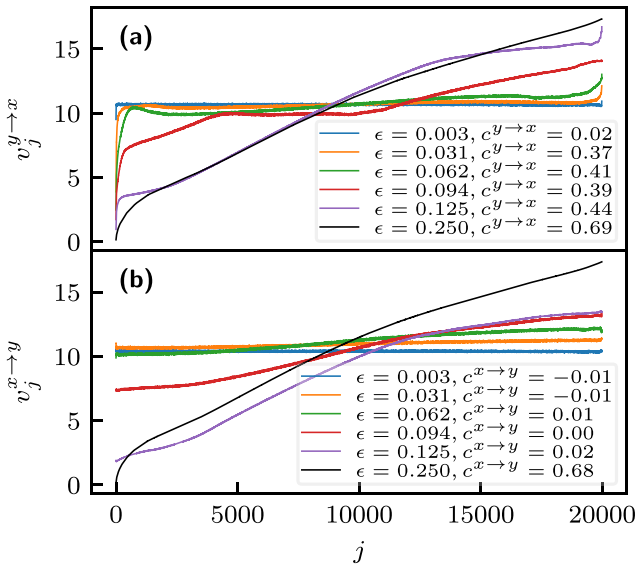

FIG. 6. The cross-distance vectors $\boldsymbol{v}^{y\to x}$ and $\boldsymbol{v}^{x\to y}$ for unidirectionally coupled Rössler subsystems at different values of the coupling parameter ϵ. They are obtained from the time series of the subsystems' coordinates x_1 and y_1 and with segment length $L = 20$.

of the two subsystems the same as in [26], resulting in coupled chaotic subsystems. They are described by

$$\ddot{x} + 0.2\dot{x} - x + x^3 = 0.3\cos(t) + \epsilon_1(y - x), \tag{29}$$

$$\ddot{y} + 0.3\dot{y} - y + y^3 = 0.5\cos(1.2t) + \epsilon_2(x - y). \tag{30}$$

We consider a unidirectional case with $\epsilon_2 = 0$ and a bidirectional case with $\epsilon_2 = 0.1$.

Time-series parameters are $N = 5 \times 10^4$ and $\Delta t = 0.5$. The system integration was done with the Runge-Kutta 4

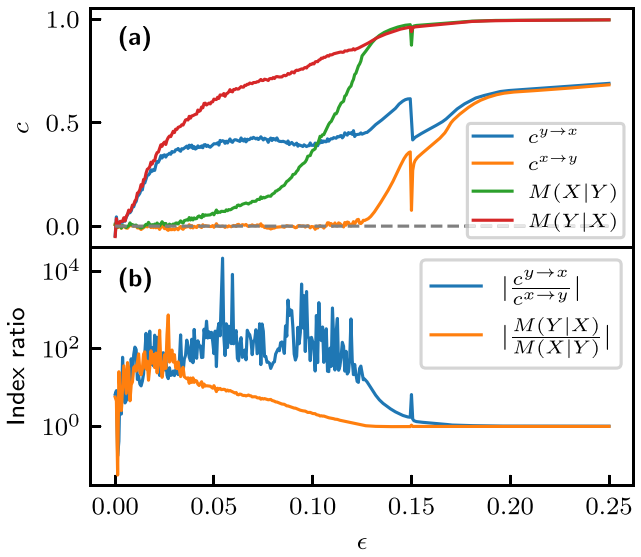

FIG. 7. The indices $c^{y\to x}$, $c^{x\to y}$, $M(Y|X)$, and $M(X|Y)$ (a), and index ratios (b) for unidirectionally coupled Rössler subsystems at different values of the coupling parameter ϵ. The coupling indices c were calculated by (12) with $k_1 = 10, k_2 = 100$, and the indices M were calculated by (14) with $k = 10$.

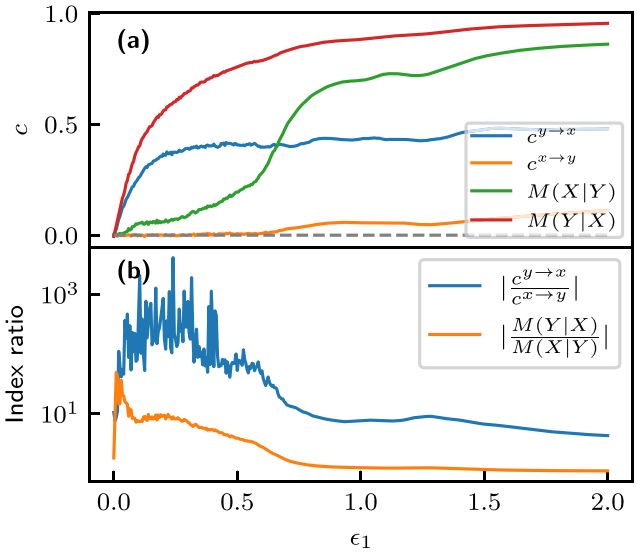

FIG. 8. The indices $c^{y\to x}$, $c^{x\to y}$, $M(Y|X)$, and $M(X|Y)$ (a) and index ratios (b) for unidirectionally coupled Duffing subsystems at different values of the coupling parameter ϵ_1. The coupling indices c were calculated by (12) with $k_1 = 10$, $k_2 = 100$, and the indices M were calculated by (14) with $k = 10$.

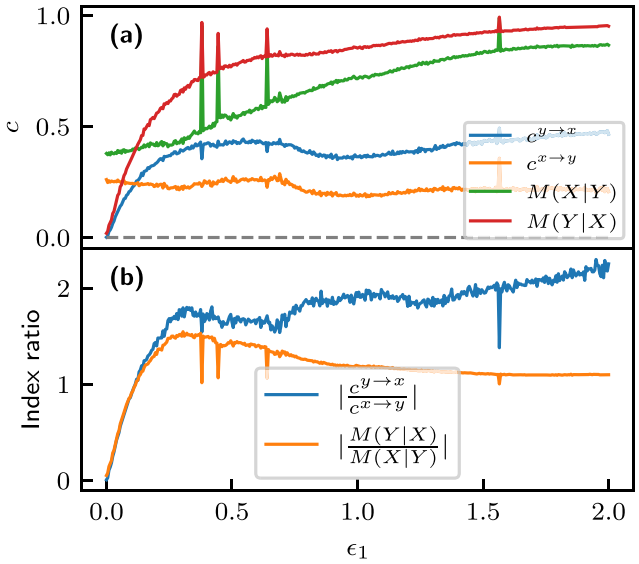

FIG. 9. The indices $c^{y\to x}$, $c^{x\to y}$, $M(Y|X)$, and $M(X|Y)$ (a) and index ratios (b) for bidirectionally coupled Duffing subsystems at different values of the coupling parameter ϵ_1 and at $\epsilon_2 = 0.1$. The sudden increases in all the indices, seen in four values of ϵ_1, are due to system bifurcations. The coupling indices c were calculated by (12) with $k_1 = 10$, $k_2 = 100$, and the indices M were calculated by (14) with $k = 10$.

integrator with a time step of 0.01. The time series of the first coordinates (positions) and segment length $L = 20$ were chosen for calculating the cross-distance vectors. Since the behavior of the cross-distance vectors is very similar to the above examples, here we only consider the coupling index dependences.

The dependence of the coupling indices $c^{x\to y}$ and $c^{y\to x}$ on the coupling parameter ϵ_1 is shown in Fig. 8(a) (unidirectional case) and Fig. 9(a) (bidirectional case). In the unidirectional case, $c^{y\to x}$ again increases with increased coupling strength while $c^{x\to y}$ stays close to zero. Synchronization occurs at around $\epsilon_1 \approx 0.75$. Therefore, cross-distance vectors can also be used to infer the coupling direction in nonautonomous Duffing subsystems correctly.

In the bidirectional case, $c^{x\to y}$ always has a positive value, while $c^{y\to x}$ increases with increased ϵ_1 similar to the unidirectional case. At around $\epsilon_1 = \epsilon_2 = 0.1$, the values of the coupling indices are the same. Therefore, cross-distance vectors can also be used to quantify coupling strength in each direction in bidirectionally coupled subsystems.

D. Comparison to established indices

We have discussed the behavior of the dependences of the coupling indices on the coupling parameter for various systems. The comparison between the coupling indices c and the established indices M is shown in Figs. 5(a), 7(a), 8(a), and 9(a). Both index variants were obtained from the same segments. The choice of the parameter k in (14) was done in a similar manner as the choice of k_1 in (12). It turns out that the optimal value of k is similar to the optimal value of k_1. This is not surprising since k_1 is chosen such that it captures the initial tail, much like k. In all of the examples in this article, $k_1 = k = 10$.

In the unidirectional cases, both indices behave similarly in the sense that in the direction $y \to x$, they increase with increased coupling, while the index in the other direction stays close to zero.

An important difference is between $c^{x\to y}$ and $M(X|Y)$. Ideally, these indices should be zero when the coupling direction is $y \to x$. The new index $c^{x\to y}$ is significantly smaller than $M(X|Y)$. Most importantly, the ratio $c^{y\to x}/c^{x\to y}$ is significantly larger than the ratio $M(Y|X)/M(X|Y)$, which is shown in Figs. 5(b), 7(b), and 8(b). As explained in Sec. II B, the summation in (15a) goes up to $N - L + 1$, which captures the increasing trend seen in the cross-distance vectors and leads to larger values of $M(X|Y)$.

Ideally, the index ratios should be infinite. By comparing the coupling indices, the coupling direction is more accurately determined with the c indices.

In the bidirectional case, the main difference between the two methods is in the indices of the direction $x \to y$. Ideally, they should be constant since $\epsilon_2 = 0.1$ is constant. The coupling parameter $c^{x\to y}$ does vary slightly, but less than $M(X|Y)$. Interestingly, bifurcations have a small impact on the coupling indices c and a large impact on M.

IV. NUMERICAL STABILITY

We have shown that the cross-distance vectors can detect the coupling direction from measured time series. In this section, we will discuss the numerical stability and parameter selection of this method. All the analysis will be done on the

test system of unidirectionally coupled Duffing subsystems with the coupling parameters $\epsilon_1 = 0.1$ and $\epsilon_2 = 0$, where the system integration is done with the Runge-Kutta 4 integrator and then sampled at $\Delta t = 0.5$. As in the previous section, the position coordinates' time series will be used to obtain the cross-distance vectors. We chose this system because it consists of continuous chaotic subsystems, a property commonly found in real systems. However, analysis of all systems in Sec. III gives similar results. The analysis in this section focuses solely on the cross-distance vectors and the new index c. A detailed comparison of numerical properties of the indices c and M is done in Appendix B.

A. Time-series length

An important property is the convergence of the cross-distance vectors with the length of the time series N. In Fig. 10, the dependence of the cross-distance vectors on the length of the time series N is shown at constant $L = 20$.

The beginning of the cross-distance vector $\boldsymbol{v}^{y\to x}$ is significantly smaller than the bulk, i.e., the vector has an initial tail. By increasing N, the first point (represented by the black line) lowers even further from the bulk, which is desired. This happens because any entry of the cross-distance vector $\boldsymbol{v}^{y\to x}$ cannot be smaller than the smallest entry of the distance matrix (9), since the vector entry itself is an average of these distances. When dealing with a finite number of segments (finite N), the smallest distance between a pair of segments will be a finite value. With increased N, the smallest distance (most likely) decreases due to a bigger number of segments. Thus, the lowest possible value of the cross-distance vector also decreases, and so do the initial values of $\boldsymbol{v}^{y\to x}$. This means that coupling is easier to detect for longer time series. In the limit $N \to \infty$, the initial values of $\boldsymbol{v}^{y\to x}$ would reach zero.

In the opposite direction with no coupling, the effect is opposite. The initial values of $\boldsymbol{v}^{x\to y}$ converge towards the bulk of the vector, i.e., there is no initial tail, which is also desired. This means that at large enough N, no coupling is detected in the direction with no coupling.

Another behavior we notice from Fig. 10 is the change of the whole shape of the cross-distance vectors. Their smoothness increases with increased N, and they seem to converge to a particular shape (which depends on the system).

To sum up, by increasing the length of the time series N, the reliability of this method increases. For large enough N, the coupling will not be detected in the direction without coupling, and it will be detected in the direction of coupling. Interestingly, the coupling direction is reliably inferred in short time series that contain only about 40 oscillations.

B. Algorithm parameter dependence

We use the same test system for this analysis. The time-series length is $N = 2 \times 10^4$. The only parameter of the cross-distance vectors algorithm is the segment length L. Figure 11(a) shows the dependence of the first points and of the mean of the cross-distance vectors on the segment length L.

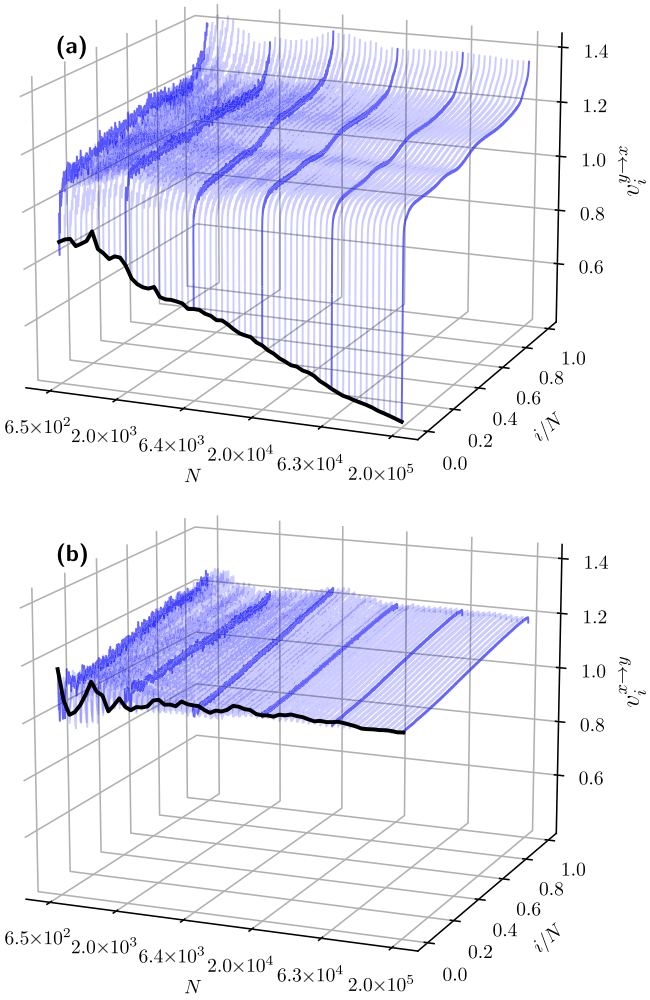

FIG. 10. The dependence of the cross-distance vectors $\boldsymbol{v}^{y\to x}$ and $\boldsymbol{v}^{x\to y}$ on the length of the time series N. The blue lines represent the cross-distance vectors at a certain N (these are the same lines as in, for example, Fig. 2). The black lines represent the values of the first points of the cross-distance vectors. For a better visibility, six cross-distance vectors are highlighted and have N that is written in the figure ticks. The scale on the N axis is logarithmic. The i axis of each plotted cross-distance vector was normalized to i/N (a value between 0 and 1) for a simpler comparison.

The value of the first point $v_1^{y\to x}$ generally decreases with increasing L up to $L \approx 200$. Since the mean values of both cross-distance vectors increase only by a little with increasing L, this indicates that the significant change is in the initial tail. In the other direction, $v_1^{x\to y}$ stays close to the mean $v_{\text{mean}}^{x\to y}$ until it starts to decrease at around $L \approx 50$. This is reflected in the coupling indices $c^{y\to x}$ and $c^{x\to y}$, the dependence of which is shown in Fig. 11(b). It tells us two important properties.

First, we notice that $c^{y\to x}$ does not detect coupling for $L = 1$. This is because, at $L = 1$, the subsystems are not well reconstructed with the segments. The Takens' embedding theorem [27] gives a minimum dimension of delay embedding vectors needed for reconstructing a system's attractor. It is $2n + 1$, where n is the system dimension (though often, less

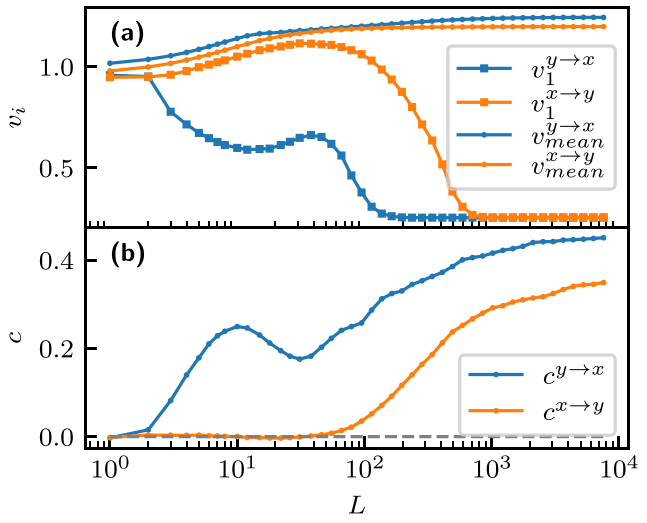

FIG. 11. The dependence of the first points and the averages of the cross-distance vectors (a) and the coupling indices (b) on the segment length L. Coupling indices were obtained with Eq. (12) with $k_1 = 10$ and $k_2 = 100$.

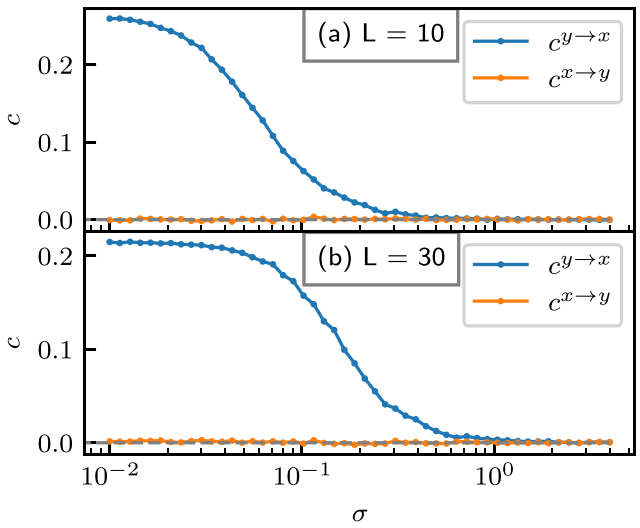

FIG. 12. The noise dependence of the coupling indices $c^{y\to x}$ and $c^{x\to y}$ with segment lengths $L = 10$ (a) and $L = 30$ (b). Coupling index parameters are $k_1 = 10$ and $k_2 = 100$.

than that is needed). For Duffing subsystems in our example, $L = 1$ does not reconstruct the attractor, which results in falsely not detecting coupling.

Second, we can see that for $L > 1$, $c^{y\to x}$ is significantly larger than $c^{x\to y}$ and generally increases with increased L, except for a local maximum at $L = 10$. The other index $c^{x\to y}$ stays close to zero until $L \approx 50$, where it starts to increase visibly. This means that a too large L results in falsely detecting coupling. The inherent similarity of neighboring segments is the reason for false coupling detection in the direction $x \to y$ at $L > 50$.

The similarity between segments will generally decrease if we increase segment length L. This becomes obvious when we notice that with increased L, more dimensions of segments must match to maintain high similarity. However, the neighboring segments $\boldsymbol{o}_i^x$ and $\boldsymbol{o}_{i+1}^x$ are autocorrelated and will therefore always be very similar for any L. This can be seen from the definition of the distance measure (7).

Therefore, when L becomes large enough, the closest segment to $\boldsymbol{o}_i^x$ will most likely be $\boldsymbol{o}_{i+1}^x$ (or $\boldsymbol{o}_{i-1}^x$). The same will hold for segments of the other subsystem, i.e., the closest to $\boldsymbol{o}_i^y$ will most likely be $\boldsymbol{o}_{i+1}^y$. This makes it seem as if both statements (5) and (6) are technically correct (but only for time autocorrelated segments), regardless of whether there is coupling. This is the reason for the increase of $c^{x\to y}$ at $L \approx 50$ in our example. It shows that L cannot be too large as it can result in falsely detecting coupling. A more detailed analysis of this effect is done in Appendix C. Guidelines for tuning this parameter are given in Sec. IV E.

The detected coupling direction turns out to be robust with respect to the choice of k_1 and k_2 when calculating the coupling indices. The general rule is that k_1 should contain the initial tail, which contains the information about coupling. The choice of k_2 is significantly less important. In this article, we chose $10k_1 < k_2 < 100k_1$, though smaller and larger values give similar results. The point is that k_2 must be much smaller than N. An analysis of the influence of k_1 and k_2 values on the indices c is done in Appendix D.

C. Noise dependence

Let us consider the noise robustness of this method. We use time series of the same test system. The time-series length is $N = 5 \times 10^4$. We add Gaussian noise to each point of the time series $x(t_i) \to x(t_i) + \xi_i$, $\xi_i \sim \mathcal{N}(0, \sigma^2)$, where σ is the standard deviation of the noise.

In Fig. 12, the dependence of the coupling indices $c^{y\to x}$ and $c^{x\to y}$ on σ is shown. As one might expect, the reliability of the detected coupling direction decreases with increased σ. For $L = 10$, the index $c^{y\to x}$ decreases to zero at around $\sigma \approx 0.4$, and for $L = 30$ at around $\sigma \approx 0.7$, which is more than a third of the subsystems' amplitudes. The other index $c^{x\to y}$ is close to zero for all values of σ.

Noise robustness can be further increased by increasing L. However, one must be careful not to increase it to the point of false detection, explained in Sec. IV B. This method is, therefore, quite robust to noise.

D. Robustness to artefacts and missing data

Measurements can contain artefacts, such as spikes, or have missing values for a time period. Coupling detection in such data can be problematic. Coupling indices are resilient to such imperfections in time series.

The solution is to delete the distance matrix elements whose values were obtained from segments with artefacts or missing values. This is done by deleting the corresponding rows and columns, decreasing the matrix size. They must be deleted from both distance matrices, even if the artefact is only present in one time series. This allows us to ignore any unwanted sections of either time series, making this approach

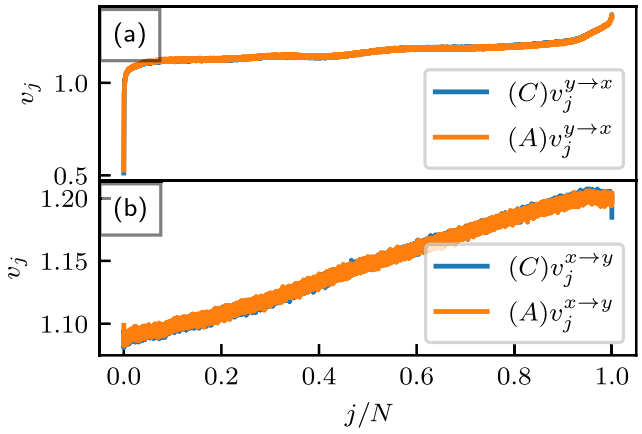

FIG. 13. Cross-distance vectors obtained from clean data (C) and from data with artefacts (A). $\boldsymbol{v}^{y\to x}$ is shown in (a) and $\boldsymbol{v}^{x\to y}$ is shown in (b). The j axis of each plotted cross-distance vector was normalized to j/N (a value between 0 and 1) for a simpler comparison. Note that the vectors obtained from clean data and from data with artefacts are nearly indistinguishable. The index values obtained from clean data are $c^{y\to x} = 0.268$, $c^{x\to y} = 0.000$, $M(Y|X) = 0.407$, $M(X|Y) = 0.052$. The index values obtained from data with artefacts are $c^{y\to x} = 0.263$, $c^{x\to y} = -0.001$, $M(Y|X) = 0.385$, $M(X|Y) = 0.049$.

very flexible. The only requirement is manually choosing the time-series points to ignore.

To give an example, consider the time series of the same test system. The time-series length is $N = 5 \times 10^4$. We change the values of x between points 5000 and 9000 and the values of y between 30 000 and 36 000 to random values to simulate artefacts. Therefore, when computing the distance matrices, we ignore $4000 + 6000 = 10\,000$ rows and columns (which will result in cross-distance vectors with 10 000 fewer points). Let us compare cross-distance vectors, c indices, and M indices obtained from clean time series and time series containing artefacts.

The results are shown in Fig. 13. The cross-distance vectors obtained from clean data and data containing artefacts are nearly indistinguishable. The c and the M indices are also nearly the same. The difference in c is seen in the third decimal. The difference in M is larger but still small. This shows that state-space approaches are resilient to artefacts and missing values.

E. Practical computational details

In this section, we will briefly discuss the practical aspects of the algorithm and provide a suggestion that can prove useful.

Tuning the L parameter. For this purpose, we can use the large similarity of neighboring segments (explained in Sec. IV B). For a chosen L, we can check whether the closest segment is often one of the neighbors, i.e., whether the distance matrices (8) and (9) have very small subdiagonals. If at least one of them does, we must lower L until subdiagonals have similar values to the rest of the matrices since small subdiagonals lead to false detection. This gives the maximal possible value $L_{\max}$. In practice, we recommend a value close to the maximal $L_{\max}$, for example, $L_{\max}/2$, since larger L generally gives more accurate and noise-robust results.

Neighboring segments. In some cases, especially in time series with a large sampling rate (small time step Δt), lowering L cannot adequately raise the values of the subdiagonals. If the time step is very small, the neighboring segments will be autocorrelated and will therefore always be very close such that $d(\boldsymbol{o}_i^x, \boldsymbol{o}_{i+1}^x) \to 0$. This can lead to false coupling detection, as explained in Sec. IV B. We propose two solutions.

The first solution is to downsample the signal. The neighboring segments become less similar by increasing the time step Δt. We must downsample the time series to the point where neighboring segments are no longer the most similar, i.e., when the subdiagonal values of the distance matrices are no longer small compared to the rest of the values.

The second solution is manually decreasing the dimensions of the distance matrices. This is needed in a case where downsampling is not an option. One such example is stiff subsystems, i.e., subsystems that contain small and large frequency components. In such cases, downsampling can erase the high-frequency component (and thus erase possibly crucial information) but still not raise the values of the subdiagonals. For this purpose, we suggest an alternative approach. We can only calculate every Mth value of the full distance matrices, i.e., we construct them from every Mth segment. Choosing M large enough ignores the (small) subdiagonals that appear in full matrices.

Both approaches should be done with a fixed L, for example $L = 5$. Once the subdiagonals are adequately raised, the chosen approach can be repeated for a larger L. If successful, the larger L should be taken for better accuracy and noise robustness.

Both approaches ignore small subdiagonals that would appear in full matrices, as well as other values that can be redundant. For example, a full matrix contains elements $d(\boldsymbol{o}_i^x, \boldsymbol{o}_j^x)$ and $d(\boldsymbol{o}_i^x, \boldsymbol{o}_{j+1}^x)$, which have similar values if $d(\boldsymbol{o}_j^x, \boldsymbol{o}_{j+1}^x) \approx 0$.

The downsampling approach is computationally more efficient, as it effectively decreases segment length L. Therefore, if possible, it should be chosen over manually decreasing dimensions.

Time and memory limitations. In a time series of length N, the computational complexity of the algorithm is $O(N^2 \log(N))$ due to the sorting of all rows of the distance matrices. As the previous paragraph explains, downsampling the original time series is recommended since it significantly decreases the execution time.

Furthermore, the matrices $\boldsymbol{D}^x$ and $\boldsymbol{D}^{y\to x}$ can, in practice, be too large to store in computer memory. To avoid this, the rows of the matrices (8) and (9) can be calculated individually to obtain a single row of $\boldsymbol{D}^{y\to x}$. One summation in (11) is done for each row, and the cross-distance vector is obtained by only storing a few sets of data of size $N - L + 1$ at once.

GPU implementation. Since the algorithm is based on matrix operations, GPU devices can significantly decrease the execution time. For this purpose, we are providing a GPU-based implementation written in Python using the JAX library [28]. A time-efficient and memory-efficient implementation is available at [29].

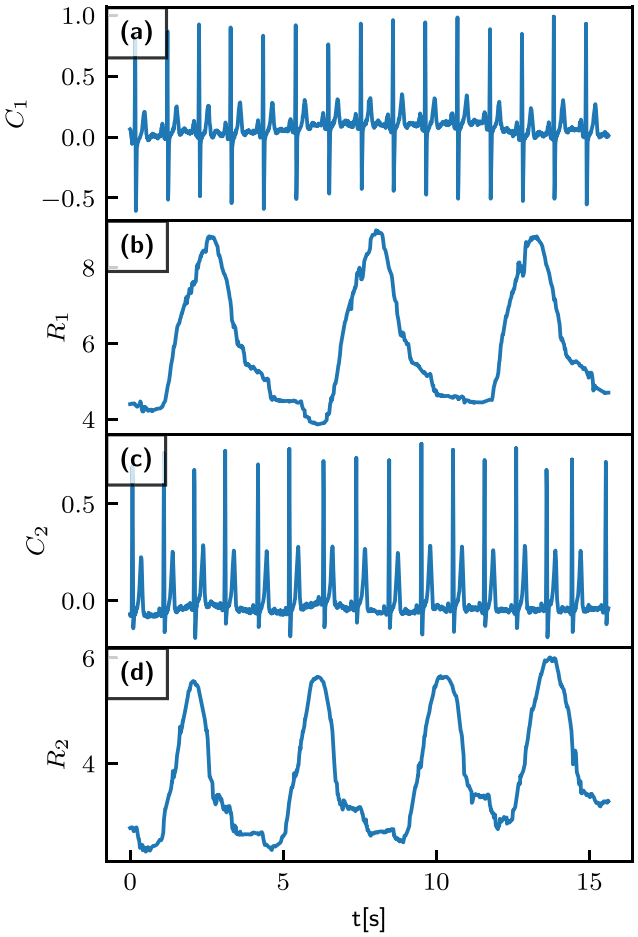

FIG. 14. A part of the ECG and respiration signals used for analysis. Label C means ECG, and label R means respiration. R_1 and C_1 were measured simultaneously on one subject, and R_2 and C_2 were measured simultaneously on another subject. Time-series parameters are $N = 172\,800$ and $\Delta t = \frac{1}{96}s$, corresponding to a measurement time of 30 min.

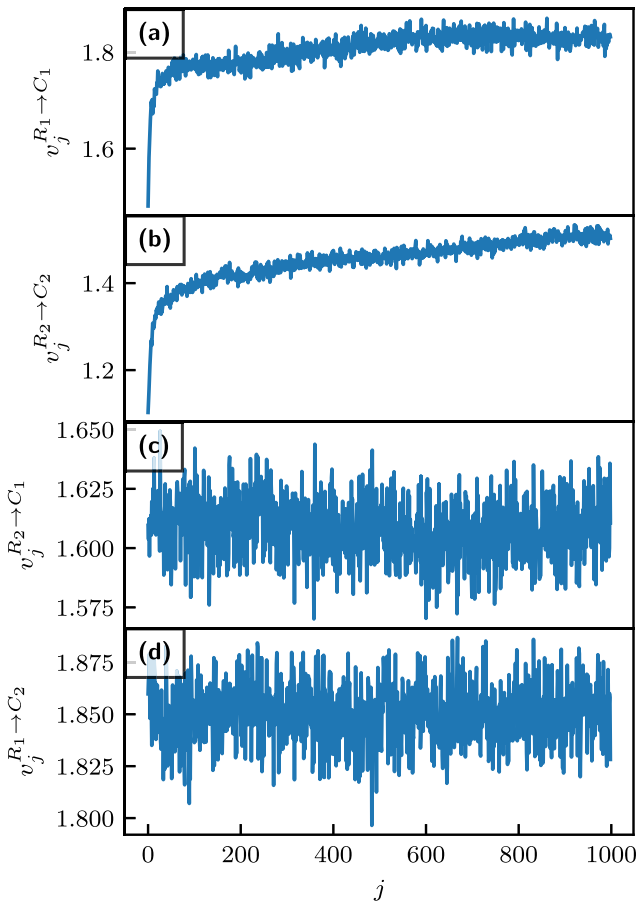

FIG. 15. The first 1000 points of the cross-distance vectors in the direction from the respiratory to the cardiac subsystem. In (a) and (b), the analyzed signals belong to the same subject, while in (c) and (d), they are independent. The segment length is $L = 20$. Dimensions of distance matrices were decreased by a factor 20.

V. APPLICATION TO PHYSIOLOGICAL SIGNALS

In this section, we will apply the cross-distance vectors algorithm to time series of physiological measurements. The goal is to show the applicability of cross-distance vectors to real-life systems. We will analyze coupling in the human cardiorespiratory system. The cardiac subsystem is characterized by ECG (electrocardiogram), and the respiratory subsystem by respiration curves obtained with a respiratory belt sensor. These subsystems are inherently bidirectionally coupled, i.e., both subsystems depend on each other. A survey of the mechanisms responsible for this dependence is given in [30]. Specifically, we will investigate coupling in the direction from the respiratory to the cardiac subsystem, which we label with $R \to C$.

The signals used in the analysis are shown in Fig. 14. Thirty minutes of ECG and respiration curves were measured on two subjects. In such a way, we obtain two pairs of signals, marked R_1 and C_1 for the first subject and R_2 and C_2 for the second subject.

The most dominant frequency component in ECG signals is around 1 Hz. The R peak is, however, very short, which means this subsystem is stiff. Therefore, we do not downsample the time series but rather manually decrease the distance matrix sizes by a factor M, as explained in Sec. IV E. In this case, we chose $M = 20$, which means we are comparing segments that are apart by a multiple of $M\Delta t = 20/96s \approx 0.2s$.

Figures 15(a) and 15(b) represent cross-distance vectors for $R_1 \to C_1$ and $R_2 \to C_2$. In these cases, ECG and respiratory signals belong to the same person and were measured simultaneously. Therefore, we expect to detect coupling. Indeed, the cross-distance vectors have an initial tail, suggesting coupling is present in the underlying subsystems.

Figures 15(c) and 15(d) represent cross-distance vectors for $R_2 \to C_1$ and $R_1 \to C_2$. Since the signals belong to different subjects that are inherently independent, we do not expect to detect coupling. Indeed, the cross-distance vectors do not have an initial tail, suggesting no coupling in the underlying subsystems.

Let us compare the c indices, obtained with parameters $k_1 = 10$, $k_2 = 1000$. The indices $c^{R_1\to C_1} = 0.105$ and $c^{R_2\to C_2} = 0.176$ are nearly two orders of magnitude larger

than $c^{R_2\to C_1} = -0.0004$ and $c^{R_1\to C_2} = -0.006$. This means that coupling indices have significantly larger values when the coupling is present in the underlying subsystems than when the subsystems are independent. Coupling indices $c^{R_2\to C_1}$ and $c^{R_1\to C_2}$ even have a small negative value, which is a strong indication of the absence of coupling.

For comparison, the M indices were also computed with parameter $k = 10$. They were computed from the same distance matrices as the c indices, i.e., matrices obtained by comparing every 20th segment with $L = 20$. The obtained values are $M(R_1|C_1) = 0.150$, $M(R_2|C_2) = 0.254$, $M(R_2|C_1) = -0.003$, and $M(R_1|C_2) = -0.009$. The M indices also correctly detect the existence of coupling in the first two cases and have a small negative value in the second two cases.

When considering the coupling indices c in an application, it should be noted that they require the time series to belong to a dynamical system that can be reconstructed with time-delay embedding. Otherwise, approaches such as Granger causality or information transfer are more suitable. However, contrary to the indices c, these approaches may not be reliable in short time series. To sum up, the new coupling indices c excel in causality detection from bivariate time series generated by a dynamical systems, especially in short signals.

VI. CONCLUSION

In this article, we have defined *cross-distance vectors* as a means of inferring the direction of coupling from bivariate time series, and we provided an algorithm for calculating them. Cross-distance vectors provide information about coupling by calculating two coupling indices, which quantify coupling strength in both directions.

The new coupling indices can infer the coupling direction in various coupled dynamical systems. Comparing the new coupling indices to the conventional indices based on state-space distance shows more accurate results with the presented approach. Analysis of numerical stability has shown that the reliability of the new indices increases with the length of the time series but is also reliable in short time series, containing only about 40 oscillations. The performance of the coupling indices was also evaluated in detecting cardiorespiratory interaction in measured data.

The algorithm has a simple implementation that requires the choice of only a maximum of three parameters. The selection of the optimal parameters' values can be made systematically, which results in robust performance and circumvents the challenge of determining optimal embedding parameters. A numerically efficient implementation is available at [29].

A logical continuation is an extension of the new method for inferring connections in a network of multiple subsystems. Should the multivariate extension be as effective as the bivariate variant, it could become an essential tool in analyzing complex multivariate problems such as brain connectivity.

The data that support the analysis of this article have been generated by the authors and can be fully reproduced from the repository in Ref. [29].

ACKNOWLEDGMENTS

The authors acknowledge Project No. J3-4525 and the research core funding No. P2-0001, which were financially supported by the Slovenian Research Agency.

The experiment from Sec. V was approved by the Ethical Committee of the University Medical Centre Ljubljana, Slovenia. All subjects provided written informed consent.

APPENDIX A: MAPPING OF CLOSE STATES

In what follows, we will provide an argument to illustrate why close states in the driven subsystem are mapped to close states in the driving subsystem for various subsystems with different properties.

One might assume that the statement (5) is false and the statement (6) is true. It may seem that the times when the driving subsystem is self-similar will appear as times of large self-similarity in the driven subsystem via coupling. Hence (6) is true. Since this logic does not apply in the other direction, one might expect that the statement (5) is false. This is, however, not the case. In a special case under two assumptions, we provide an analytic argument. For a more general case, we will provide a heuristic argument.

Special case. Consider that two segments of the driven subsystem $\boldsymbol{o}_i^x$ and $\boldsymbol{o}_j^x$ are identical (this is only possible for subsystems in a regular dynamical regime),

$$\begin{aligned}&\boldsymbol{x}(t_{i+k}) = \boldsymbol{x}(t_{j+k}),\\ &k = 0, 1, \ldots, L-1.\end{aligned} \tag{A1}$$

If the subsystem coordinates match over a time period, their time evolution must also match. The first assumption is that $\boldsymbol{f}$ is time-independent, which gives us the following L equations:

$$\begin{aligned}&\boldsymbol{f}(\boldsymbol{x}(t_{i+k})) + \boldsymbol{g}(\boldsymbol{x}(t_{i+k}), \boldsymbol{y}(t_{i+k}))\\ &\quad = \boldsymbol{f}(\boldsymbol{x}(t_{j+k})) + \boldsymbol{g}(\boldsymbol{x}(t_{j+k}), \boldsymbol{y}(t_{j+k})),\\ &k = 0, 1, \ldots, L-1.\end{aligned} \tag{A2}$$

Additionally, from (A1) it follows that

$$\begin{aligned}&\boldsymbol{f}(\boldsymbol{x}(t_{i+k})) = \boldsymbol{f}(\boldsymbol{x}(t_{j+k})),\\ &k = 0, 1, \ldots, L-1.\end{aligned} \tag{A3}$$

Combining (A2) and (A3) gives us

$$\begin{aligned}&\boldsymbol{g}(\boldsymbol{x}(t_{i+k}), \boldsymbol{y}(t_{i+k})) = \boldsymbol{g}(\boldsymbol{x}(t_{j+k}), \boldsymbol{y}(t_{j+k})),\\ &k = 0, 1, \ldots, L-1.\end{aligned} \tag{A4}$$

Since (A1) holds, we can consider the first argument of $\boldsymbol{g}$ as constant and define k functions

$$\begin{aligned}&\tilde{\boldsymbol{g}}(\boldsymbol{y}(t_{i+k})) = \boldsymbol{g}(\boldsymbol{x}(t_{i+k}), \quad \boldsymbol{y}(t_{i+k})),\\ &k = 0, 1, \ldots, L-1.\end{aligned} \tag{A5}$$

The second assumption is that functions $\tilde{\boldsymbol{g}}(\boldsymbol{y}(t_{i+k}))$ are injective. If this is the case, from (A4) it follows that

$$\begin{aligned}&\boldsymbol{y}(t_{i+k}) = \boldsymbol{y}(t_{j+k}),\\ &k = 0, 1, \ldots, L-1.\end{aligned} \tag{A6}$$

This means that statement (5) is *true*. This argument does not work in the other direction with swapped $\boldsymbol{x}$ and $\boldsymbol{y}$, since $\boldsymbol{y}$ does not depend on $\boldsymbol{x}$, i.e., there is no coupling function in the time evolution of $\boldsymbol{y}$. Therefore, the statement (6) is *false*.

General case. We argue that if the subsystems are sufficiently nice, this also holds without the two assumptions if segment length L is large enough. To obtain (A4) from (A2) with time-dependent $\boldsymbol{f}(\boldsymbol{x}, t)$, we argue that it would seem unlikely for the sum of $\boldsymbol{f}$ and $\boldsymbol{g}$ to match over a time period if they do not match individually. The analysis in Sec. III C shows that this indeed holds for coupled periodically forced Duffing subsystems. To obtain (A6) from (A4) if $\tilde{\boldsymbol{g}}(\boldsymbol{y}(t_{i+k}))$ are not injective, we would similarly argue that if $\boldsymbol{g}$ matches over a long enough time period, so must its arguments.

We can use the same arguments for chaotic subsystems by demanding the distance of segments to be less than δ instead of them being identical. Under the admissibility conditions of the Poincaré recurrence theorem, the choice of δ can be arbitrarily small. The arguments hold for chaotic subsystems by swapping all the equalities in Eqs. (A1)–(A6) with arbitrarily small proximity.

APPENDIX B: DETAILED COMPARISON OF *c* and *M*

Here the goal is to compare the numerical stability of c and M indices. For that purpose, the analysis from Sec. IV is repeated for M, and both results are presented jointly. All the analysis is done on the same test system of coupled Duffing oscillators as in Sec. IV. Also, all the parameters are the same as in Sec. IV. Coupling is unidirectional with direction $y \to x$.

1. Dependence on time-series length

The analysis in Sec. IV A was done on the cross-distance vectors. For results to be comparable to M, we compute the c indices. As explained in Sec. III D, the indices are most fairly compared when their parameters are $k = k_1$. In our case, $k = k_1 = 10$ and $k_2 = 100$ are taken, the same as in Sec. III C. While these are not optimal parameters for every N, we keep them fixed for simplicity. The segment length is $L = 20$, as in Sec. IV A. The comparison is done in Fig. 16.

The general behavior is similar for both indices, as seen in Fig. 16(a). At small N, all indices are large. The main difference between M and c is seen at large N where $c^{x\to y}$ converges to zero, which is desirable, while $M(X|Y)$ seems to converge to a finite positive value. As explained in Sec. II B, this is because c ignores possible trends in the cross-distance vectors, while M does not.

The index ratios are shown in Fig. 16(b). Ideally, the ratios are infinite since the coupling is unidirectional. For nearly all values of N, the ratio $c^{y\to x}/c^{x\to y}$ is larger than the ratio $M(Y|X)/M(X|Y)$, especially for large N. For small N, the difference is smaller, but the c ratio is generally still larger. This shows that c better determines the coupling direction for both short and long time series.

2. Dependence on *L*

Let us compare the L dependence from Fig. 11 for indices c and M. The chosen time-series length is $N = 2 \times 10^4$, same as in Sec. IV B.

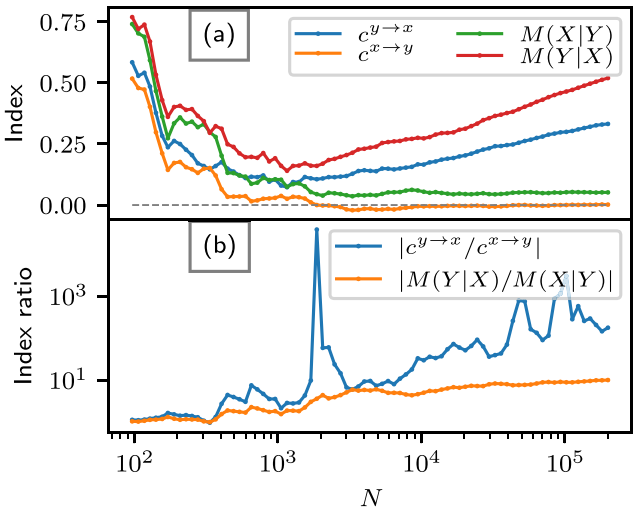

FIG. 16. The dependence of the indices $c^{y\to x}$, $c^{x\to y}$, $M(Y|X)$, $M(X|Y)$ (a) and the index ratios $c^{y\to x}/c^{x\to y}$, $M(Y|X)/M(X|Y)$ (b) on the length of the time series N. The M index parameter is $k = 10$ and the c index parameters are $k_1 = 10, k_2 = 100$.

The dependence of the indices c and M on the segment length L is shown in Fig. 17(a). The dependence is very similar for both index variants. The main difference is that both M indices are slightly larger (since they do not ignore trends seen in cross-distance vectors). At $L = 1$, the M indices both have a very similar positive value, while the c indices are both much closer to zero. Interestingly, the bias of $M(X|Y)$ due to trends is nearly constant for segment length up to $L \approx 50$, where L becomes too large (as explained in Sec. IV B).

The index ratios $c^{y\to x}/c^{x\to y}$ and $M(Y|X)/M(X|Y)$ are shown in Fig. 17(b). The ratio of the c indices is significantly larger than that of the M indices for all values of L except for $L = 1$. This means that the c indices better determine

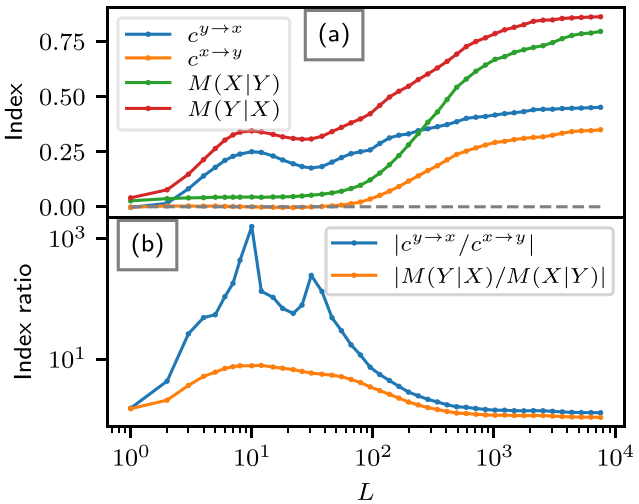

FIG. 17. The dependence of the c and M indices (a) and the index ratios $c^{y\to x}/c^{x\to y}$ and $M(Y|X)/M(X|Y)$ (b) on the segment length L. The M index parameter is $k = 10$ and the c index parameters are $k_1 = 10, k_2 = 100$.

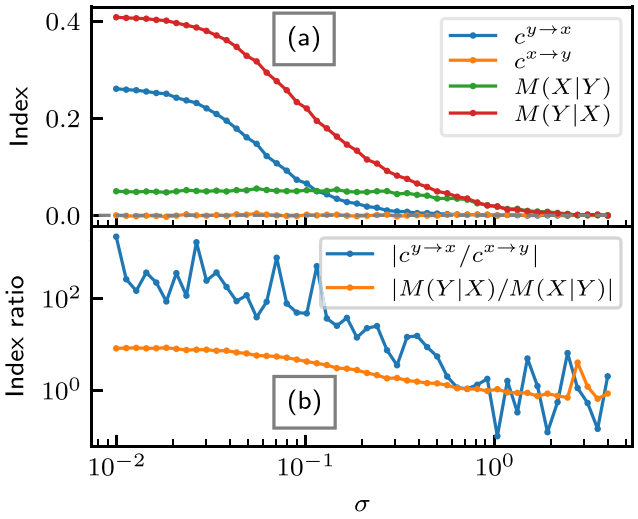

FIG. 18. The dependence of the c and M indices (a) and the index ratios $c^{y\to x}/c^{x\to y}$ and $M(Y|X)/M(X|Y)$ (b) on the standard deviation of noise σ. The M index parameter is $k = 10$ and the c index parameters are $k_1 = 10, k_2 = 100$. The segment length is $L = 10$.

the coupling direction regardless of the choice of segment length L.

3. Dependence on noise

Let us compare the noise robustness of the c and the M indices similarly as in Sec. IV C. The chosen time-series length is again $N = 5 \times 10^4$ and the chosen segment length is $L = 10$, the same as in Fig. 12(a).

The dependence of the c and M indices on the standard deviation of noise σ is shown in Fig. 18(a). It turns out that the dependence is very similar for both indices. They are both robust to noise. As seen in Fig. 18(b), the index ratio is larger for c than for M up to around $\sigma \approx 0.5$, at which point both ratios become close to 1.

APPENDIX C: THE N and L DEPENDENCE OF CROSS-DISTANCE VECTORS

To get a complete picture of the behavior of the cross-distance vectors, we compute them for numerous values of pairs (N, L). We again use the test system from Sec. IV. We are interested in the cross-distance vectors' first (nonzero) point. The results are shown in Fig. 19. Figure 19 can be understood as plotting the black lines in Fig. 10, calculated for different L. Equivalently, Fig. 19(a) can be seen as plotting $v_1^{y\to x}$ from Figs. 11(a) and 19(b) as $v_1^{x\to y}$ from Fig. 11(a), both calculated for different N.

Figure 19(a) shows $v_1^{y\to x}$, which corresponds to the direction of coupling. One can roughly identify three areas in the (N, L) grid that are highlighted using two red lines. Note that the areas are not strictly defined but assist in explaining the figure. Area 1 has very small values. There, L is too large at a given N, which results in detecting coupling regardless of the underlying dynamics (area of falsely detecting coupling).

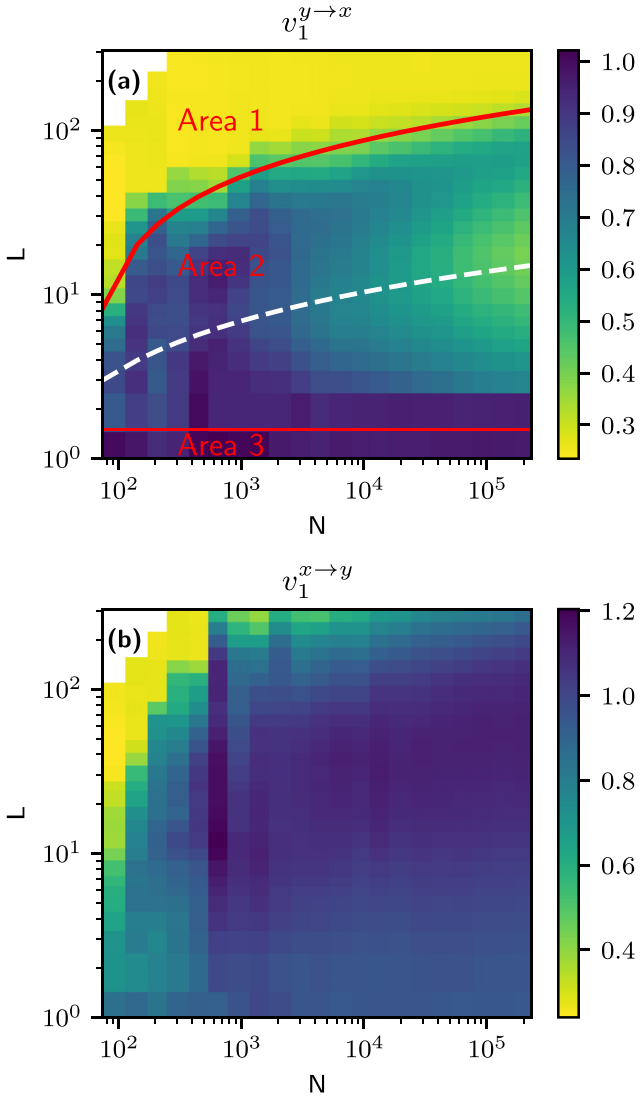

FIG. 19. The first point of the cross-distance vectors $v_1^{y\to x}$ (a) and $v_1^{x\to y}$ (b) for different values of the time-series length N and the segment length L. In (a), the two red lines separate the grid into three areas, and the white line approximately represents optimal L at a given N. The white area in the upper left corner represents the impossible pairs (N, L) where $L \geqslant N$.

Area 3 has large values. There $L = 1$, which is too small (at any N) to reconstruct the underlying state space, which results in not detecting coupling regardless of the underlying dynamics (area of falsely not detecting coupling). Area 2 has moderate values. There, L is large enough to reconstruct the underlying state space but small enough to avoid false detection.

The white line highlights the approximate area where the optimal L at a given N is. We understand the optimal L as the value in area 2 where $v_1^{y\to x}$ is the smallest at a given N. The optimal L increases with increased N.

Figure 19(b) shows $v_1^{x\to y}$, which corresponds to the direction without coupling. In this case, the three areas and the optimal L are not as obvious as in the other direction. We only

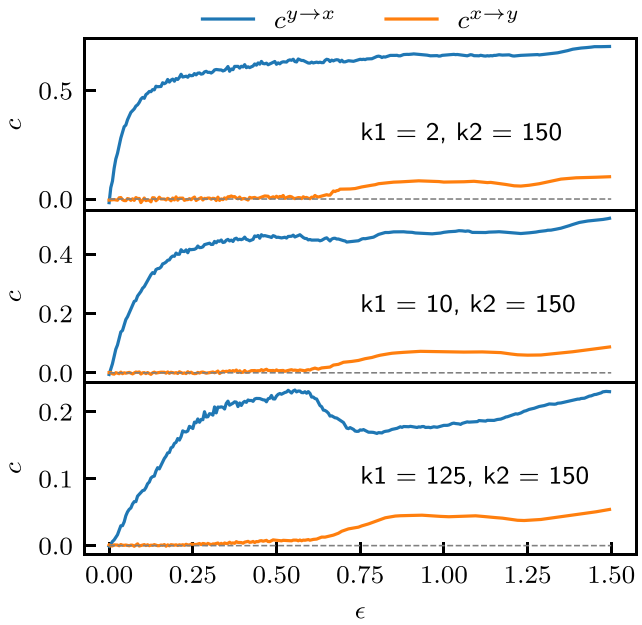

FIG. 20. The dependence of the coupling indices c on the coupling parameter ϵ for different values of the parameter k_1 and fixed $k_2 = 150$.

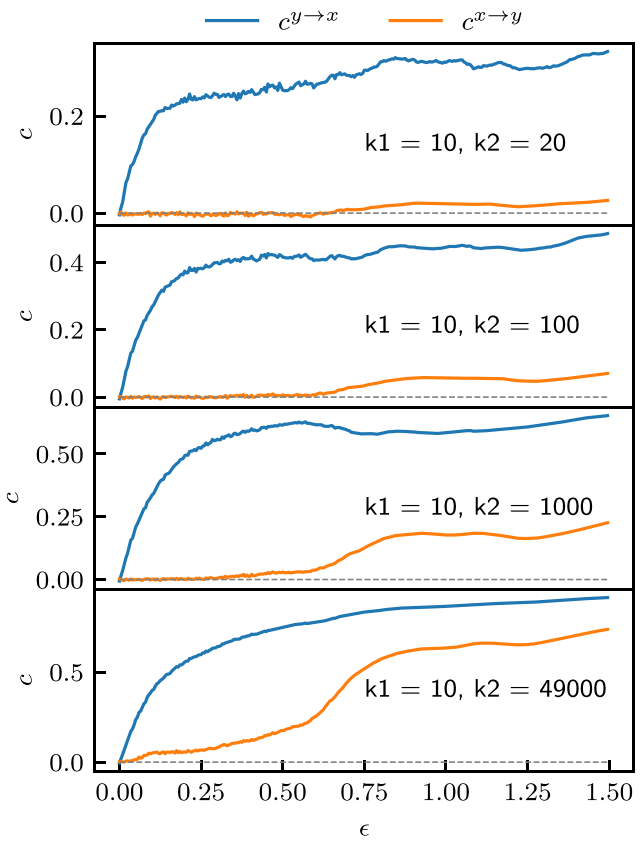

FIG. 21. The dependence of the coupling indices c on the coupling parameter ϵ for different values of the parameter k_2 and fixed $k_1 = 10$.

clearly see where L becomes too large, which leads to false coupling detection.

It should be noted that in both figures, there is a white area in the upper left corner. This area represents the impossible pairs (N, L), i.e., $L \geqslant N$.

APPENDIX D: THE CHOICE OF PARAMETERS k_1 AND k_2

To analyze the influence of the parameters k_1 and k_2 on the coupling indices c, we consider the same test system used in Sec. IV. Specifically, we will plot the c indices from Fig. 8(a) (blue and orange lines), obtained with different k_1 and k_2.

The influence of the change of k_1 is shown in Fig. 20. In this case, we fixed the parameter $k_2 = 150$, which is close to k_2 most often used in the article. We can make some important observations. First, we notice that for small values of k_1, the values of $c^{y\to x}$ increase quickly with increased ϵ, which allows for more reliable detection at small coupling. Furthermore, the values of $c^{y\to x}$ reach higher values, while the values of $c^{x\to y}$ remain unchanged, which is also desirable. However, there is a negative side to using such small values of k_1. The variance of both indices is not negligible, as seen by a larger spread of $c^{x\to y}$ around zero and a negative value of $c^{y\to x}$ at $\epsilon = 0$. On the other hand, increasing k_1 decreases the variance of both indices. However, it also reduces the rate of increase of $c^{y\to x}$ and introduces a bias at moderate values of ϵ (around 0.5). Therefore, the choice of k_1 offers a tradeoff between bias and variance of the indices c.

The influence of the change of k_2 is shown in Fig. 21. Similar to the influence of k_1, the variance of both indices is larger at smaller k_2. Furthermore, larger k_2 increases $c^{x\to y}$ at moderate values of ϵ, increasing the false positive error. Most importantly, this false positive error increases drastically when k_2 is close to the time-series length N ($k_2 = 49\,000$ in our case). One can notice a strong similarity between the case of $k_2 = 49\,000$ and the M indices in Fig. 8(a) (green and red lines). Based on this analysis, we draw the conclusion that the safe choice for k_2 is approximately $10k_1 < k_2 < 100k_1$.

[1] J. Runge, M. Riedl, A. Müller, H. Stepan, J. Kurths, and N. Wessel, Quantifying the causal strength of multivariate cardiovascular couplings with momentary information transfer, Physiol. Meas. **36**, 813 (2015).

[2] S. Schulz, F.-C. Adochiei, I.-R. Edu, R. Schroeder, H. Costin, K.-J. Bär, and A. Voss, Cardiovascular and cardiorespiratory coupling analyses: A review, Philos. Trans. R. Soc. A **371**, 20120191 (2013).

[3] M. Wibral, R. Vicente, and J. T. Lizier, *Directed Information Measures in Neuroscience* (Springer, Berlin, 2014).

[4] J. Runge, S. Bathiany, E. Bollt, G. Camps-Valls, D. Coumou, E. Deyle, C. Glymour, M. Kretschmer, M. D. Mahecha, J. Muñoz-Marí, E. H. van Nes, J. Peters, R. Quax, M. Reichstein, M. Scheffer, B. Schölkopf, P. Spirtes, G. Sugihara, J. Sun, K. Zhang *et al.*, Inferring causation from time series in earth system sciences, Nat. Commun. **10**, 2553 (2019).

[5] G. Sugihara, R. May, H. Ye, C. hao Hsieh, E. Deyle, M. Fogarty, and S. Munch, Detecting causality in complex ecosystems, Science **338**, 496 (2012).

[6] H. Ye, E. R. Deyle, L. J. Gilarranz, and G. Sugihara, Distinguishing time-delayed causal interactions using convergent cross mapping, Sci. Rep. **5** (2015).

[7] C. W. J. Granger, Investigating causal relations by econometric models and cross-spectral methods, Econometrica **37**, 424 (1969).

[8] K. D. Hoover, Causality in economics and econometrics, in *The New Palgrave Dictionary of Economics* (Palgrave Macmillan, UK, 2008), pp. 1–13.

[9] A. Papana, E. Siggiridou, and D. Kugiumtzis, Detecting direct causality in multivariate time series: A comparative study, Commun. Nonlin. Sci. Numer. Simul. **99**, 105797 (2021).

[10] P. Clemson, G. Lancaster, and A. Stefanovska, Reconstructing time-dependent dynamics, Proc. IEEE **104**, 223 (2016).

[11] L. A. Baccalá and K. Sameshima, Partial directed coherence: a new concept in neural structure determination, Biol. Cybern. **84**, 463 (2001).

[12] T. Schreiber, Measuring Information Transfer, Phys. Rev. Lett. **85**, 461 (2000).

[13] M. Paluš and M. Vejmelka, Directionality of coupling from bivariate time series: How to avoid false causalities and missed connections, Phys. Rev. E **75**, 056211 (2007).

[14] M. G. Rosenblum and A. S. Pikovsky, Detecting direction of coupling in interacting oscillators, Phys. Rev. E **64**, 045202(R) (2001).

[15] M. Paluš and A. Stefanovska, Direction of coupling from phases of interacting oscillators: An information-theoretic approach, Phys. Rev. E **67**, 055201(R) (2003).

[16] A. Bandrivskyy, A. Bernjak, P. McClintock, and A. Stefanovska, Wavelet phase coherence analysis: Application to skin temperature and blood flow, Cardiovasc. Eng. **4**, 89 (2004).

[17] J. Jamšek, A. Stefanovska, and P. V. E. McClintock, Wavelet bispectral analysis for the study of interactions among oscillators whose basic frequencies are significantly time variable, Phys. Rev. E **76**, 046221 (2007).

[18] J. Arnhold, P. Grassberger, K. Lehnertz, and C. Elger, A robust method for detecting interdependences: application to intracranially recorded EEG, Physica D **134**, 419 (1999).

[19] R. G. Andrzejak, A. Kraskov, H. Stögbauer, F. Mormann, and T. Kreuz, Bivariate surrogate techniques: Necessity, strengths, and caveats, Phys. Rev. E **68**, 066202 (2003).

[20] D. Chicharro and R. G. Andrzejak, Reliable detection of directional couplings using rank statistics, Phys. Rev. E **80**, 026217 (2009).

[21] S. Guo, A. K. Seth, K. M. Kendrick, C. Zhou, and J. Feng, Partial granger causality—eliminating exogenous inputs and latent variables, J. Neurosci. Methods **172**, 79 (2008).

[22] J. Sun and E. M. Bollt, Causation entropy identifies indirect influences, dominance of neighbors and anticipatory couplings, Physica D **267**, 49 (2014).

[23] S. H. Strogatz, *Nonlinear Dynamics and Chaos* (Taylor & Francis, 2015).

[24] E. Ott, *Chaos in Dynamical Systems* (Cambridge University Press, 2002).

[25] M. Paluš, V. Komárek, Z. Hrnčíř, and K. Štěrbová, Synchronization as adjustment of information rates: Detection from bivariate time series, Phys. Rev. E **63**, 046211 (2001).

[26] M. Brešar, P. Boškoski, and M. Horvat, Detection of coupling in duffing oscillator systems, Chaos **31**, 063130 (2021).

[27] F. Takens, Detecting strange attractors in turbulence, in *Lecture Notes in Mathematics* (Springer, Berlin, 1981), pp. 366–381.

[28] Jax library, https://github.com/google/jax.

[29] Python implementation of the cross-distance vectors algorithm, https://repo.ijs.si/e2pub/cd-vec.

[30] T. E. Dick, Y.-H. Hsieh, R. R. Dhingra, D. M. Baekey, R. F. Galán, E. Wehrwein, and K. F. Morris, Cardiorespiratory coupling, in *Progress in Brain Research* (Elsevier, Amsterdam, 2014), pp. 191–205.

5.2 A Rank-Based Measure with Improved Accuracy and Its Application to EEG Data

The coupling index c defined in Chapter 5.1 has been shown to infer the coupling direction significantly more accurately than the classical state space measures. However, it still has a drawback which can lead to three problems. In what follows, these problems are first discussed. Then, a new rank-based measure c^r that alleviates the drawback is introduced. Finally, c^r is combined with bivariate surrogates and applied to an electroencephalogram (EEG) database, showing its applicability to real data.

5.2.1 Drawback of the coupling index c

The drawback of the coupling index c is that its range of possible values is not between 0 and 1 and can strongly depend on the analyzed time series. This can lead to three problems, which are discussed in this section.

First problem To illustrate the first problem with the coupling index c, let us again consider two unidirectionally coupled Rössler systems with slightly offset frequencies, described by the equation (5.1). Let us compare the behavior of the measures c and M, obtained for realizations of this system at different values of the coupling strength ε. The results are shown in Figure 5.24. At large coupling strengths, the dynamics are nearly

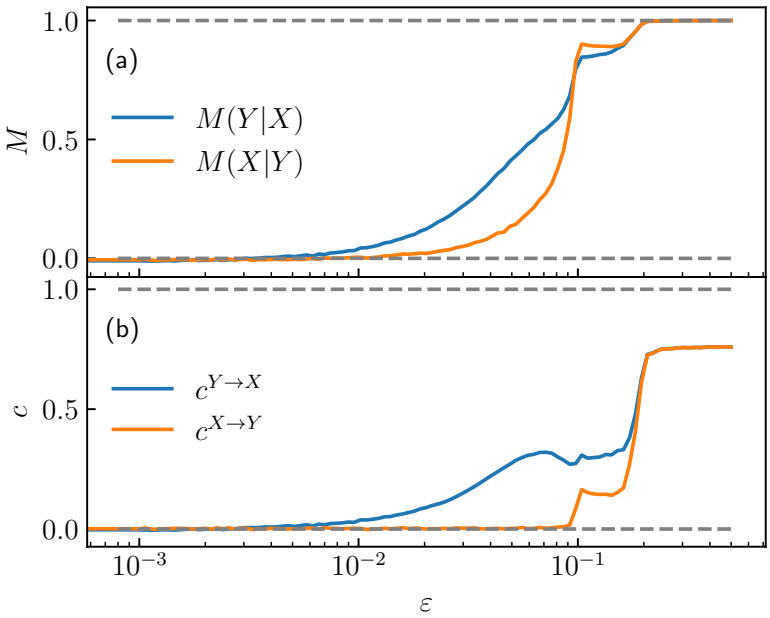

Figure 5.24: Values of the two directional coupling measures M (a) and c (b), obtained for unidirectionally coupled Rössler systems (5.1) for 100 values of ε spaced equidistantly on a logarithmic scale. Solid lines represent the mean values of 100 realizations, and colored bands represent $\pm$ one standard deviation at each value of ε. The system is solved with random initial conditions with an integration step 0.01. All the parameters are kept the same as in Figure 5.1.

identical, and the values of c are considerably below 1, as opposed to the values of M, which are much closer to 1. This happens because the values of the components of the

cross-distance vector $\boldsymbol{v}^{Y\to X}$ cannot be smaller than the smallest entry of the respective distance matrix $\boldsymbol{D}^Y$, and the initial tail cannot reach zero. The maximal possible value of c is thus substantially smaller than 1. On the other hand, the value of M is exactly 1 for identical dynamics, making interpreting the results simpler than when using c.

Second problem The second problem is that the systems X and Y typically do not have the same distribution of values of entries of their respective distance matrices $\boldsymbol{D}^X$ and $\boldsymbol{D}^Y$. This leads to different possible ranges of values of the measures $c^{Y\to X}$ and $c^{X\to Y}$, resulting in a less equitable comparison. This means it is harder to reliably infer the direction of coupling with c indices when the distributions of values of the entries of $\boldsymbol{D}^X$ and $\boldsymbol{D}^Y$ are very different.

Third problem The third problem pertains to surrogate data. As stated above, different distributions of distances lead to inequitable comparisons of index values. This is also a problem when comparing the values obtained from the original time series to those obtained from the surrogates. The reason is that the surrogates $s_x(t_i)$ often have substantially different distributions of values in their distance matrices than the original signal $x(t_i)$. Therefore, using surrogates to provide a baseline for the values of the measure c can be problematic.

5.2.2 Rank-based measure c^r

To alleviate the drawback discussed above while retaining the increased accuracy of the coupling index c, a rank-based measure c^r is defined as a novelty in this dissertation.

The idea of using ranks instead of indices comes from the L measure (3.19), defined in Chapter 3.5.3.2. Recall that the cross-rank matrix $\boldsymbol{B}^{Y\to X}$ is obtained by ranking the rows of the cross-distance matrix $\boldsymbol{D}^{Y\to X}$. Each row of the cross-rank matrix contains integers from 1 to N. If the entry $D_{ij}^{Y\to X}$ tells the distance from $\boldsymbol{x}_i$ to its j-th conditioned nearest neighbor, then the entry $B_{ij}^{Y\to X}$ tells which true neighbor of $\boldsymbol{x}_i$ its j-th conditioned nearest neighbor is. For example, if the first conditioned nearest neighbor of $\boldsymbol{x}_i$ is also its first (true) nearest neighbor, then $B_{i1} = 1$. In analogy with the definition of the cross-distance vector, one can define the *cross-rank vector* as the mean of the rows of the cross-rank matrix

$$\boldsymbol{r}^{Y\to X},\ r_j^{Y\to X} = \frac{1}{N}\sum_{i=1}^{N} B_{ij}^{Y\to X}. \tag{5.4}$$

The other cross-rank vector $\boldsymbol{r}^{X\to Y}$ is obtained similarly by swapping X and Y.

The comparison of the cross-distance vectors and the cross-rank vectors obtained for the coupled Rössler systems (5.1) is shown in Figure 5.25. One can see that much like the cross-distance vectors $\boldsymbol{v}^{Y\to X}$, the cross-rank vectors $\boldsymbol{r}^{Y\to X}$ also have an initial tail, making it possible to quantify coupling in the same manner with both of them. Apart from the difference in scale, the plots of the cross-distance vectors and cross-rank vectors look very similar. The most interesting difference seen in the figure is in the case of strong coupling. There, the coupled systems are nearly identical, and the rows of $\boldsymbol{B}^{Y\to X}$ and $\boldsymbol{B}^{X\to Y}$ are just the first N integers in sequential order. The cross-rank vector, which is the mean of these rows, therefore also contains simply the first N integers in sequential order, as shown by the red lines in Figure 5.25 (b) and (d). The most important difference, not visible in these plots, is that the distribution of ranks is always uniform for all time series.

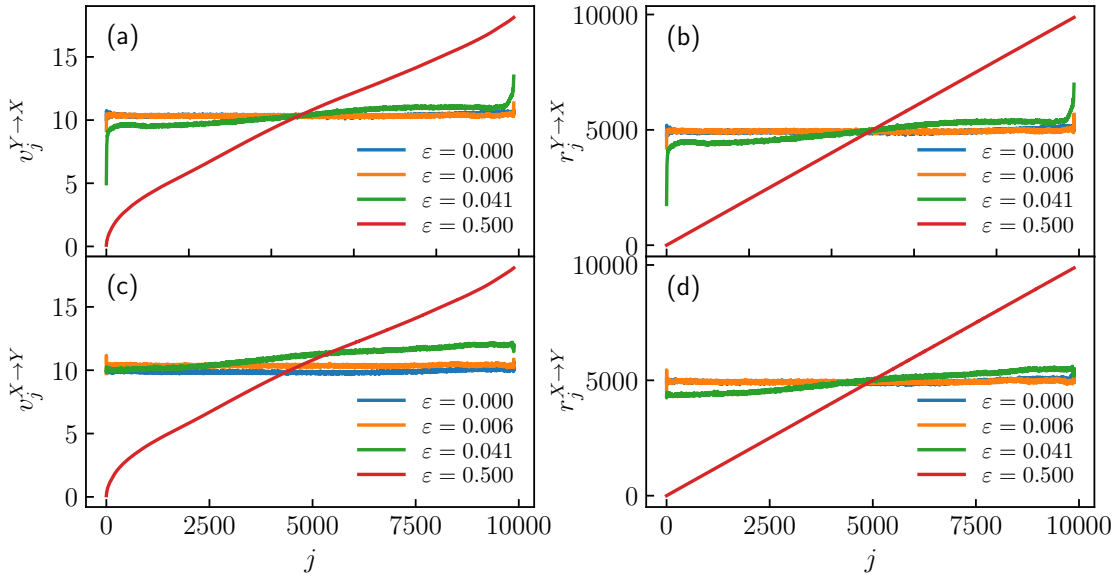

Figure 5.25: Plot of the values of the components of the cross-distance vectors $\boldsymbol{v}^{Y\to X}$ (a) and $\boldsymbol{v}^{X\to Y}$ (c), and of the cross-rank vectors $\boldsymbol{r}^{Y\to X}$ (b) and $\boldsymbol{r}^{X\to Y}$ (d). They are computed on realizations of the Rössler dynamics (5.1) at four different values of coupling strength ε. All the parameters are kept the same as in Figure 5.1.

The final measure $c^{r,Y\to X}$ that quantifies couplings $Y \to X$ is given by

$$c^{r,Y\to X} = \frac{r^{Y\to X}_{k_1+1:k_2} - r^{Y\to X}_{1:k_1}}{r^{Y\to X}_{1:k_2}}, \tag{5.5}$$

where

$$r^{Y\to X}_{i:j} = \frac{1}{j-i+1}\sum_{k=i}^{j} r^{Y\to X}_{k}. \tag{5.6}$$

The measure $c^{r,X\to Y}$ quantifies couplings $X \to Y$ and is obtained similarly by swapping the roles of X and Y. Note that the equations (5.4)–(5.6) are in complete analogy with the definition of the distance-based coupling index c (5.3). The only difference is using the cross-rank matrix $\boldsymbol{B}^{Y\to X}$ instead of the cross-distance matrix $\boldsymbol{D}^{Y\to X}$.

Figure 5.26 shows the analysis of the coupled Rössler systems using the rank-based measures L and c^r. The plots look very similar to Figure 5.24, which used the distance-based measures M and c. The mean value of the measure $c^{r,X\to Y}$ starts increasing from zero at a much stronger coupling than the mean value of the measure $L(X|Y)$. This shows that much like the distance-based c, the rank-based c^r more accurately determines the coupling direction than the classical state-space measures M and L for a wider range of coupling strengths. However, c^r reaches values very close to 1 when the coupling is strong, while c does not. The first problem of c discussed in Chapter 5.2.1 is thus solved when using c^r.

Additionally, because the distributions of ranks are identical (they are uniform) regardless of the time series, the comparison of measures $c^{r,Y\to X}$ and $c^{r,X\to Y}$ is more equitable than the comparison of $c^{Y\to X}$ and $c^{X\to Y}$. Thus, c^r is a more reliable coupling direction detection tool than c. The second problem of c is thus also solved. For the same reasons, the measure c^r also enables a more equitable comparison of original values to surrogate values than c, solving the third problem of the measure c.

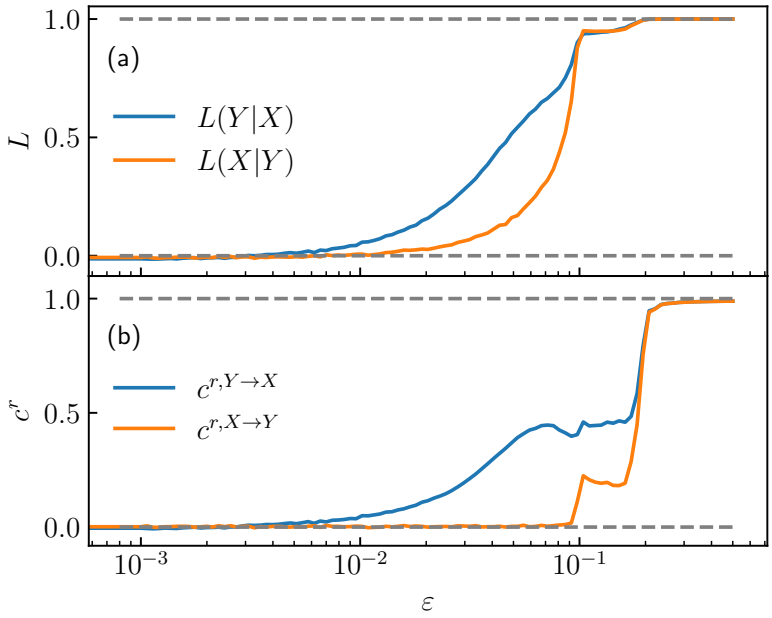

Figure 5.26: Values of the two directional coupling measures L (a) and c^r (b), obtained for unidirectionally coupled Rössler systems (5.1) for 100 values of ε spaced equidistantly on a logarithmic scale. Solid lines represent the mean values of 100 realizations, and colored bands represent $\pm$ one standard deviation at each value of ε. All the parameters are kept the same as in Figure 5.1.

5.2.3 Application of the rank-based measure c^r combined with bivariate surrogates to EEG data

An application of the rank-based measure c^r to a database of EEG measurements is presented to assess the applicability of the new rank-based measure on real signals. The analyzed database is the publicly available Bern-Barcelona EEG database [9]. It comprises 7500 pairs of signals extracted from intracranial EEG recordings of five epilepsy patients during the seizure-free intervals. One half of the pairs were recorded from brain areas where the first seizure-related EEG signal changes were detected for the individual patient (focal signal pairs), and the other half from brain areas that were not involved in the patients' seizures at their onset (nonfocal signal pairs).

It has been shown that focal signals exhibit a larger degree of nonlinear interdependence than nonfocal signals during the seizure-free interval [9], [46], [65]. The potential clinical application is to assist in localizing the brain areas where seizures start in order to assess whether the patient can benefit from the neurosurgical resection of these parts of the brain. It is crucial that the difference can be seen in the seizure-free interval, as every seizure is potentially dangerous. Thus, all the signals in the database were taken from recordings of the seizure-free interval. Focal and nonfocal signal pairs were picked randomly across patients, time, and channel pairs within the respective brain areas. They each have a length of 20 seconds at a sampling frequency of 512 Hz and were recorded simultaneously at neighboring EEG channels. For a more detailed description of the signal acquisition, composition, and preprocessing, the reader is referred to Ref. [9]. An example of a pair of focal signals is shown in Figure 5.27 (a).

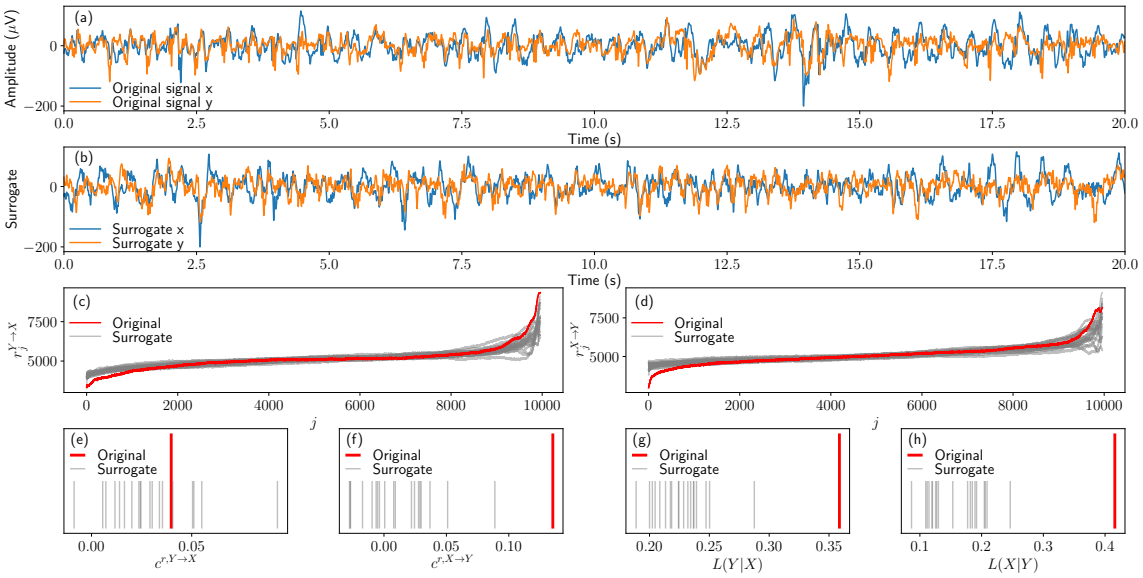

Figure 5.27: (a) Example of a focal EEG signal pair, (b) example of a surrogate pair of this signal pair, (c)-(d) cross-rank vectors $\boldsymbol{r}$ for signals and surrogates, (e)-(h) L and c^r values obtained for the original signal pairs and values obtained for the surrogates.

5.2.3.1 Detecting interactions within EEG signals

In the initial analysis of the Bern-Barcelona EEG database, the L measure was combined with bivariate surrogates, and results showed more rejections for focal than for nonfocal signals [9]. Here, the analysis is extended by including not only L but also c^r. For each pair of signals, 19 surrogates are computed. Note that taking 19 surrogates and using a one-sided rank-order test corresponds to the significance level of $\alpha = 0.05$ [51]. An example of a bivariate surrogate signal is shown in Figure 5.27 (b).

Unlike the original analysis, the data is not downsampled by a factor of four to preserve as much information about the dynamics as possible. The embedding parameters are $\tau = 1$, $m = 128$, the Theiler correction window is $W = 76$, the parameter of L is $k = 10$ and the parameters of c^r are $k_1 = 10, k_2 = 100$. The cross-rank vectors obtained for the exemplary pair of EEG signals, along with the ones obtained for 19 pairs of surrogate signals, are shown in Figure 5.27 (c),(d), while (e)-(h) show the respective c^r and L measures. In this example, the test based on L rejects the null hypothesis for both directions, while using c^r, it is rejected only for one direction. This is not an untypical example, as c^r leads to rejections in *both* directions in only around 1% of cases, while L does so in some 23%.

Since the signal pairs were selected randomly from different patients, times, and brain areas, the directions $X \to Y$ and $Y \to X$ carry no significant meaning. Andrzejak, Schindler, and Rummel [9] did thus not consider the aspect of direction and used a symmetrized measure to quantify the overall strength of the interactions: $L^S = (L(X|Y) + L(Y|X))/2$. In what follows, the symmetrized measure $c^{r,S} = (c^{r,Y\to X} + c^{r,X\to Y})/2$ is considered to compare new results to the ones of Ref. [9].

Table 5.1: The proportions of rejection for focal data p_f and for nonfocal data p_n, and the contrast D, obtained with the symmetrized measures L^S and $c^{r,S}$. Recall that the test has a significance level of 0.05. Note that the resulting proportions of rejection obtained with L^S are close to, but not identical to, the ones obtained in Ref. [9]. This is due to different surrogate realizations and the difference in data downsampling, and perhaps due to slightly different nearest neighbor parameter used in calculating the L measure ($k = 10$ in contrast with their $k = 5$).

	p_f	p_n	D
L^S	0.511	0.370	0.160
$c^{r,S}$	0.107	0.056	0.313

Table 5.2: Average values of the symmetrized measures $\langle L^S \rangle$ and $\langle c^{r,S} \rangle$. Averaging is done over all focal and over all nonfocal EEG signals.

	Focal	Nonfocal
$\langle L^S \rangle$	0.526	0.485
$\langle c^{r,S} \rangle$	0.084	0.092

5.2.3.2 Results

To determine whether the measures can help in distinguishing between focal and nonfocal signals, following Ref. [9], the contrast D is defined as the relative difference

$$D = \frac{p_f - p_n}{p_f + p_n}, \tag{5.7}$$

where p_f and p_n are the proportions of rejection of the surrogate null hypothesis across all signal pairs in the focal and the nonfocal group, respectively. The proportions and the resulting contrasts are shown in Table 5.1.

The test based on L^S leads to much higher proportions of rejection than the one based on $c^{r,S}$ for both focal and nonfocal signals. Comparing the measures' contrasts, however, one finds that $c^{r,S}$ has a nearly two times larger contrast than L^S. This is because the L measure is more influenced by signal properties other than nonlinear interdependence, as shown by the analysis of Chapter 5.1. The resulting contrasts reveal that the measure c^r has an increased ability to distinguish focal from nonfocal signals compared to the L measure. This shows that c^r not only performs better on simulated data but also gives better results in an application.

Finally, a significant insight is revealed by observing the mean values of the symmetrized measures, shown in Table 5.2. Here, the surrogates are not taken into account. One can see that there is very little difference in the focal versus the nonfocal values. The mean focal value of $c^{r,S}$ is even smaller than the mean nonfocal value of $c^{r,S}$. This would contradict the established understanding that focal signals are more interdependent than nonfocal. The larger interdependence within focal signals only becomes apparent when the surrogates are included in the analysis, making them a crucial tool for applying coupling detection measures to EEG data.

Chapter 6

Quantifying Neurovascular Coupling Strength by a Perturbation Experiment

This chapter presents a perturbation experiment for quantifying neurovascular coupling in patients with severe aortic stenosis (AS) [66]. *Neurovascular coupling* is a term used to describe the interactions between the neural and the vascular subsystems of the human body. It causes alterations in local perfusion that occur in response to changes in neuronal activity [67]. AS is a condition where the aortic valve opening narrows. It is characterized by the obstruction of blood outflow from the left ventricle, which can impair target organ perfusion, such as the brain.

The dynamics behind the regulatory mechanisms of the neurovascular system are highly complex and not easy to uncover. However, by performing a perturbation experiment, the strength of specific couplings can be quantified. The neurovascular couplings can be quantified by analyzing the blood flow response in the arteries to some external stimulus [68]. Our experiment was conducted in collaboration with the University Medical Centre Ljubljana. A visual stimulus was shown to a person, evoking a response in the blood flow in the posterior cerebral artery (PCA). Because this artery leads to the part of the brain responsible for vision, the visual stimulus results in an increased PCA blood flow. Note that while neurovascular coupling is a broader term, from now on, it is used to refer specifically to the influence of the neural system on the PCA blood flow.

In the experiment, visual stimulation was performed with a checkerboard with black and white squares. Every 0.5 s, the colors of the squares swapped for maximal stimulation. The experiment consisted of ten cycles, each with a 20 s rest phase (OFF phase) during which the subject had their eyes closed and a 30 s phase during which the patient looked at the screen (ON phase).

Blood velocity v was measured by the noninvasive transcranial Doppler ultrasonography [69]. An example of a measurement of one cycle is shown in Figure 6.1 (a). The oscillations with frequency around 1 Hz are a consequence of heartbeat, and the sudden increase at $t = 20\,\mathrm{s}$ is the response to the patient opening their eyes and looking at the visual stimulus. This response is better seen in Figure 6.1 (b), which shows the velocity measurement for all cycles with an applied low-pass filter. One can see large differences between the ten cycles. Seemingly random deviations like this typically appear when analyzing complicated physiological systems. Analyzing ten cycles substantially decreases the variance of results due to such randomness.

One can quantify the amount of blood transferred by the PCA by the measured velocity of its blood flow. Assuming a constant surface area of the artery and a constant velocity

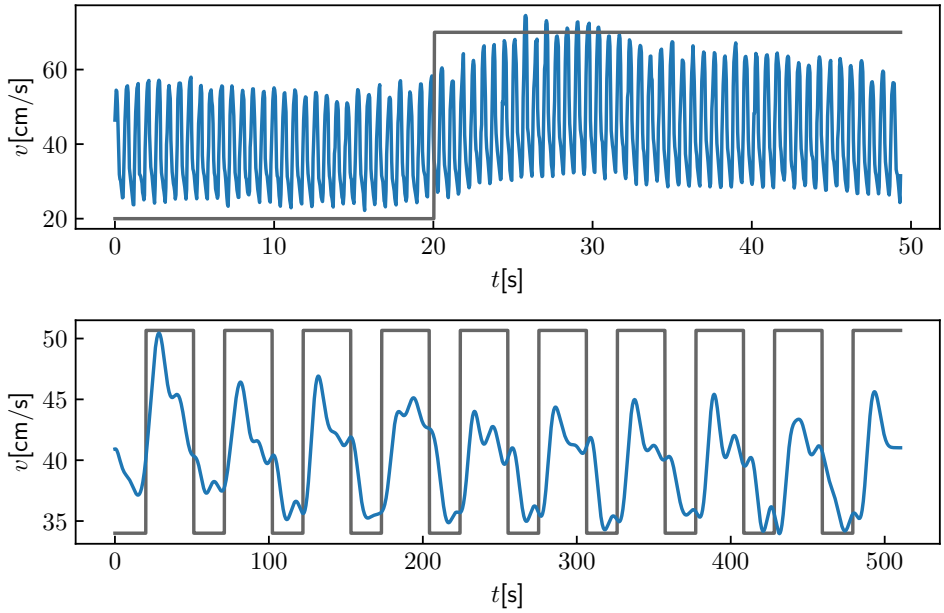

Figure 6.1: (a) An exemplary cycle of the PCA velocity measurement, and (b) an exemplary velocity signal of all ten cycles with an applied low-pass filter, which removed the frequencies below 0.1 Hz. The gray lines represent the time periods of the ON phases (larger values) and the OFF phases (smaller values).

across this surface, the blood flow j is directly proportional to the velocity. Thus, we consider the relative change in the measured velocities between the ON and the OFF phases, which equals the respective relative change in the blood flow. This is called the visually evoked cerebral blood flow velocity response (VEFR) [70]. It is defined as

$$\mathrm{VEFR} = \frac{j_{\mathrm{stim}} - j_{\mathrm{rest}}}{j_{\mathrm{rest}}} = \frac{v_{\mathrm{stim}} - v_{\mathrm{rest}}}{v_{\mathrm{rest}}}, \tag{6.1}$$

where v_{rest} and v_{stim} are computed as the mean of the last 5 s of the OFF phase, and the last 10 s of the ON phase, respectively. This is done in order to quantify the (ideally) stationary values, which the velocity tends to overshoot in the beginning of the ON phase, as seen in Figure 6.1. The VEFR is computed for each of the ten cycles, resulting in ten values for each measurement.

The study involved 54 patients with AS and 43 age- and sex-matched healthy controls. The clinical importance was determining if AS leads to dysfunction in the regulatory mechanisms of cerebral blood flow. This was evaluated by identifying a statistically significant difference in the quantified neurovascular coupling between the healthy group and the AS group. Contrary to expectations, the study found that neurovascular coupling was larger in the AS group compared to the control. The difference can be easily seen by observing the mean responses of each group, shown in Figure 6.2. Although the characteristic response curve of the healthy group starts increasing faster compared to that of the AS group, the latter reaches larger maximal values, as well as larger end values. These results show that contrary to initial expectations, there is no decline but still a dysregulation in neurovascular coupling.

The work done as part of this dissertation included designing a program to display visual stimuli, assisting with the setup of the measurement system and data storage, and conducting time series analysis. The latter consisted of preprocessing and extracting features

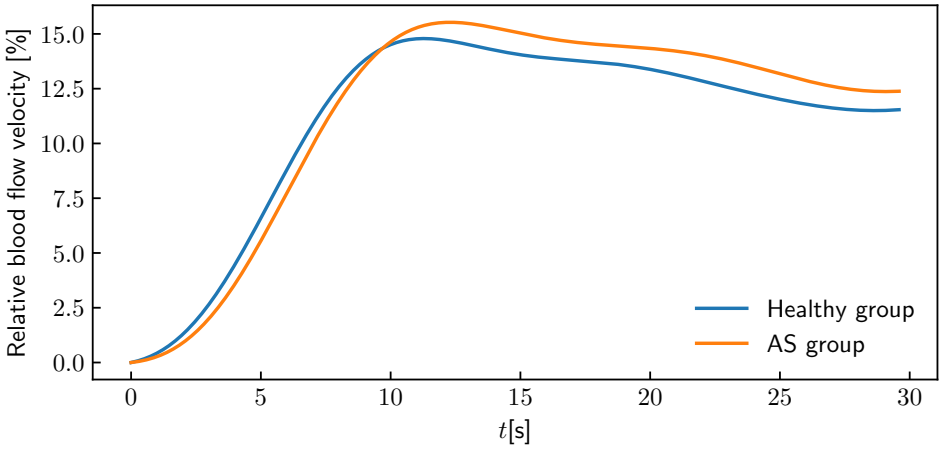

Figure 6.2: The average relative change in blood flow velocity of each group. The averaging is done over all ten cycles of all the individuals in a group, resulting in a single characteristic response curve for each group. A low-pass filter that removed frequencies below 0.1 Hz was applied before the averaging to obtain a clearer depiction of the response curves. The relative blood flow velocity is computed as the relative change from the beginning of the ON phase.

used for statistical analysis. The selection of participants, conducting the measurements, and performing the statistical analysis were carried out by collaborators at the University Medical Centre Ljubljana.

6.1 Neurovascular Coupling in Severe Aortic Valve Stenosis

Received: 28 February 2023 | Revised: 18 May 2023 | Accepted: 6 July 2023

DOI: 10.1002/brb3.3155

ORIGINAL ARTICLE

Brain and Behavior Open Access WILEY

Neurovascular coupling in severe aortic valve stenosis

Ana Ovsenik[1,2] | Matej Podbregar[3,4] | Nikola Lakič[5] | Martin Brešar[6,7] | Pavle Boškoski[7] | Ivan Verdenik[8] | Andrej Fabjan[9,10]

[1]Faculty of Medicine, Department of Biomedicine, University of Ljubljana, Ljubljana, Slovenia

[2]Department of Cardiology, University Medical Centre Ljubljana, Ljubljana, Slovenia

[3]Faculty of Medicine, Department of Internal Medicine, University of Ljubljana, Ljubljana, Slovenia

[4]Department of Intensive Care, General Hospital Celje, Celje, Slovenia

[5]Department of Cardiovascular Surgery, University Medical Centre Ljubljana, Ljubljana, Slovenia

[6]Jožef Stefan International Postgraduate School, Ljubljana, Slovenia

[7]Department of Systems and Control, Jožef Stefan Institute, Ljubljana, Slovenia

[8]Department of Obstetrics and Gynaecology, Division for Research, University Medical Centre Ljubljana, Ljubljana, Slovenia

[9]Faculty of Medicine, Institute for Physiology, University of Ljubljana, Ljubljana, Slovenia

[10]Department of Vascular Neurology and Neurological Intensive Care, University Medical Centre Ljubljana, Ljubljana, Slovenia

Correspondence
Andrej Fabjan, MD PhD, Department of Vascular Neurology and Neurological Intensive Care, University Medical Centre Ljubljana, Zaloska cesta 2, 1000 Ljubljana, Slovenia.
Email: andrej.fabjan@mf.uni-lj.si

Funding information
Slovenian Research and Innovation Agency, Grant/Award Number: P3-0019

Abstract

Objectives: Aortic stenosis (AS) is characterized by obstruction of blood outflow from the left ventricle, which can impair target organ perfusion such as the brain. We hypothesized that hemodynamic changes in AS may lead to dysfunction of cerebral blood flow regulatory mechanisms. The aim of our study was to evaluate neurovascular coupling in patients with AS by Transcranial Doppler ultrasonography.

Methods: Neurovascular coupling was assessed using visually evoked cerebral blood flow velocity responses (VEFR) calculated as relative blood flow velocity changes in the posterior cerebral artery upon visual stimulation. We analyzed peak systolic, mean and end diastolic VEFR in 54 patients with severe AS and 43 controls in 10 consecutive cycles of visual stimulation. Repeated-measures ANOVA test was used to compare cerebral hemodynamic data by group.

Results: Patients with AS had significantly higher peak systolic (12.9% ± 5.6% and 10.5% ± 4.5%; $p = .009$) and mean VEFR (14.4% ± 5.8% and 12.2% ± 4.9%; $p = .021$) compared to controls, whereas only a tendency for higher end diastolic VEFR was observed (16.7% ± 6.9% and 14.4% ± 6.2%; $p = .061$).

Conclusion: We have shown for the first time that patients with severe AS exhibit higher VEFR than controls indicating dysregulation of neurovascular coupling, which can be one of the factors contributing to development of cognitive decline.

KEYWORDS
aortic stenosis, cerebral blood flow, neurovascular coupling, transcranial Doppler

1 | INTRODUCTION

Aortic stenosis (AS) is the most frequent primary valvular heart disease in the developed world, affecting 2.8% of population older than 75 years (Rashedi & Otto, 2015). Progressive aortic valve narrowing with concomitant left ventricular pressure overload and resultant left ventricular hypertrophy lead to the classic triad of AS symptoms including dyspnea, angina, and syncope (Joseph et al., 2017). In

addition, cognitive scores of patients with severe AS are considerably lower compared with age, sex and education-matched individuals without AS (Abdul-Jawad Altisent et al., 2016). The precise mechanisms by which AS might precipitate brain dysfunction have not been fully elucidated, but may include improper initial upstroke time of velocity in carotid and vertebral arteries due to obstruction of blood outflow from the left ventricle (Kleczynski et al., 2017). In time, this can lead to dysfunction of cerebral blood flow (CBF) regulation, which may be reflected in cognitive decline (Ovsenik et al., 2021).

Multiple regulatory mechanisms overlap to provide tight CBF control due to the brain's high metabolic demand for oxygen, limited intracellular capacity for energy storage, rapid changes of metabolic demand with neuronal activity and enclosed cranium limited space (Ovsenik et al., 2021; Toth et al., 2017). Dysfunction in any of the regulatory mechanisms can cause functional deficits in the brain. Impairment of neurovascular coupling has been suggested as a major contributor to cognitive decline in hypertension and Alzheimer's disease (Girouard & Iadecola, 2006). Neurovascular coupling presents a complex functional association between astrocytes, neurons and microvasculature, which enables regional CBF to adapt to local neuronal activity (Phillips et al., 2016). The increase in regional CBF might be initiated from the direct effect of neuronal activity on the microvasculature, but the broader regional increase in CBF results from conduction of vasodilatation and myogenic responses to the remote upstream blood vessels (Iadecola, 2017). Fortunately, these are accessible to insonation with Transcranial Doppler Ultrasonography (TCD), which enables noninvasive assessment of neurovascular coupling by measurement of visually evoked cerebral blood velocity responses (VEFR) reflecting relative blood flow velocity changes in the posterior cerebral artery (PCA) upon visual stimulation (Aaslid, 1987; Panczel et al., 1999).

In this study, we hypothesized that neurovascular coupling may be impaired in AS due to chronic hemodynamic changes in the cerebral circulation. As there has been no report on neurovascular coupling in AS, our aim was to evaluate VEFR in patients with AS using TCD.

TABLE 1 Participants' characteristics.

	Aortic stenosis	Controls	*p* Value
n	54	43	
Clinical characteristics			
Age (years)	70.7 (± 9.8)	70.6 (± 10.9)	.957
Sex (*n* women)	19 (35.2%)	13 (30.2%)	.384
BMI (kg/m2)	28.0 (± 4.5)	25.7 (± 3.3)	.007
Arterial hypertension (*n*)	45 (83.3%)	18 (41.9%)	<.001
Diabetes mellitus (*n*)	17 (31.5%)	5 (11.6%)	.017
Hyperlipidemia (*n*)	34 (63.0%)	25 (58.1%)	.391
Smoking (*n*)	5 (9.3%)	2 (4%)	.323
Medication intake (*n*)			
Beta-blocker	28 (51.9%)	4 (9.3%)	<.001
ACEi	33 (61.1%)	13 (30.2%)	.002
ARB	6 (11.1%)	5 (11.6%)	.592
MRA	1 (1.9%)	0	.557
Ca^{2+} blockers	13 (24.1%)	5 (11.6%)	.095
Diuretics	23 (42.6%)	7 (16.3%)	.005
Statins	32 (59.3%)	14 (32.6%)	.008
Hemodynamic measurements			
MAP (mmHg)	93 (± 15)	113 (± 22)	<.001
Et-CO_2 (mmHg)	36 (± 4)	37 (± 4)	.141
HR (/min)	71 (± 10)	66 (± 10)	.035
Mean PCA (cm/s)	32.4 (± 7.8)	31.4 (± 6.0)	.557
Mean MCA (cm/s)	43.5 (± 9.5)	45.5 (± 11.1)	.356
LVEF	65 (± 9)	66 (± 3)	.418

BMI: body mass index, ACEi: angiotensin converting enzyme inhibitors, ARB: angiotensin II receptor blockers, MRA: mineralocorticoid receptor blockers, MAP: mean arterial pressure, Et-CO_2: end-tidal CO_2, HR: heart rate, mean PCA: mean velocity in posterior cerebral artery, mean MCA: mean velocity in medial cerebral artery, LVEF: left ventricular ejection fraction.
Numerical variables are presented as mean ± SD, while categorical variables are presented as absolute values and percentages.

2 | MATERIALS AND METHODS

2.1 | Participants

The study included 54 patients with severe AS (35 men, 19 women; mean age 70.7 ± 9.8 years) and 43 age- and sex-matched controls without AS or other cardiac disease (30 men, 13 women; mean age 70.6 ± 10.9 years). The AS group consisted of patients with severe AS, who were admitted to the Department of Cardiovascular Surgery, University Medical Centre Ljubljana, for isolated aortic valve replacement surgery without concomitant intervention on the other valves, coronary arteries, the ascending aorta and carotid arteries. The diagnosis and indication for surgery were undertaken according to the latest ESC Guidelines on valvular heart disease (Vahanian et al., 2021). Community-dwelling controls without known cardiac disease were recruited from general practices of the Primary Healthcare Centre Ljubljana after undergoing echocardiography to exclude AS. Exclusion criteria for patients as well as controls included age <18 years, ≥50% stenosis of the common or internal carotid artery as assessed by duplex sonography, history of ischemic stroke in the PCA territory, epilepsy, alcohol abuse, left ventricular ejection fraction less than 30%, noncorrectable vision and poor temporal acoustic window.

The experimental procedures for the study were approved by the National Ethical Committee of the Republic of Slovenia (No. 0120–97/2018) and followed the principles of the Helsinki Declaration. A written consent was obtained from all the participants. Participants' characteristics are presented in Table 1.

2.2 | Research protocol

TCD examination was performed in a dark, soundproof room with temperature of around 22°C. The examination protocol was thoroughly explained to the participants before the examination.

Participants were instructed breathe calmly, not to talk and not to move heads during the procedure, which was performed in the sitting position. They had 2 MHz Doppler probes (Delica-9 series, SMT Medical) mounted on the head using a flexible plastic commercial head holder. Blood flow velocity (BFV) in P2 segment of the right posterior cerebral artery (PCA) and M1 segment of the medial cerebral artery (MCA) were recorded through the temporal bones. The M1 segment of the left MCA served as a reference for the control of the nonspecific effects of systemic factors. The strongest signal of the corresponding artery was found with adjustment of probes' position, depth and sample volume, as described elsewhere (Phillips et al., 2016; Willie et al., 2011). Participants were seated 1.5 m from the screen onto which the visual stimulus was projected. Visual stimulation was performed with the use of a checkerboard with 100% contrast between light and dark squares that appeared in the manner of the inverse-pattern with the frequency of 1 Hz. The experiment contained 10 cycles, consisting of a 20-s rest phase (phase OFF) during which the subject had their eyes closed and the screen was dark, and a 30-s phase of visual stimulation during which the patient focused on the red cross in the middle of the checkerboard on the screen (phase ON). Patients' BFV in the left MCA and right PCA, arterial blood pressure (BP) and breath-by-breath partial pressure of end-tidal carbon dioxide (Et-CO_2) were measured continuously. BP was monitored in a noninvasive manner with the cuff on the right ring finger on the level of the right hip under the level of the heart (Finapress 2300 Blood pre, Ohmeda) and Et-CO_2 across the facial mask with the use of a capnometer (Oscaroxy capnometer, Datex).

2.3 | Signal processing and data analysis

The transcranial Doppler signals were demodulated down to audible frequency range and sampled at 8.1 kHz. The cardiorespiratory signals were sampled at 5 kHz. The signals were synchronized by using external digital input that was triggered at the start of each measurement session. Individual ON/OFF cycles in the signals that were affected by artifacts, such as external noise disturbances that significantly decreased the signal-to-noise ratio and could potentially lead to erroneous outcomes, were excluded.

An envelope curve of the PCA and MCA signals was used for velocity analysis. To evaluate peak systolic and end diastolic velocities, the peaks and valleys within the signal were identified, whereas mean velocities were estimated according to the Equation (1):

$$\text{Mean velocity} = \frac{\text{Systolic velocity} + (2 \times \text{Diastolic velocity})}{3}. \quad (1)$$

HR was obtained from times between peaks in the PCA velocities and the Et- CO_2 values were determined by peaks in the CO_2 signal. Mean values of BP, Et-CO_2, and HR were calculated for ON and OFF phases and averaged for the 10 consecutive cycles.

According to the mechanism of neurovascular coupling, the stimulus leads to increase of blood flow velocity after approximately 1 s of visual stimulation, reaches the maximum after 5–10 s, followed by decrease and stabilization of the velocity on a lower level (plateau phase) (Aaslid, 1987). After removal of the visual stimulus, blood flow velocity falls to baseline level as presented schematically in Figure 1. For the assessment of neurovascular coupling, VEFR presenting the relative change of blood flow velocity in plateau phase in relation to baseline was calculated using the Equation (2):

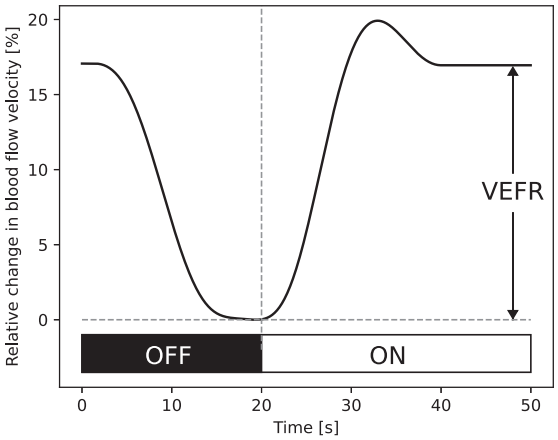

FIGURE 1 Schematic presentation of the visually evoked relative blood flow velocity time course in relation to baseline in PCA. VEFR: visually evoked cerebral blood flow velocity response, PCA: posterior cerebral artery.

$$\text{VEFR} = \frac{v\,(\text{stimul}) - v\,(\text{rest})}{v\,(\text{rest})} \times 100\%, \quad (2)$$

where *v*(stimul) was average BFV during the last 10 s of visual stimulation and *v*(rest) average BFV during the last 5 s of rest (Boms et al., 2010; Fabjan et al., 2015; Olah et al., 2008; Rosengarten et al., 2001). VEFR were calculated separately for peak systolic, mean and end diastolic velocities of the PCA. Within one person, cerebral blood flow velocity data of 10 cycles were averaged and compared between the AS and control group (Fabjan et al., 2012). Additionally, relative PCA blood flow velocity changes in the early phase of visual stimulation were estimated for the time period 10 s from the peak onset in the hemodynamic response and compared between groups. Relative changes in the MCA BFV during stimulation were calculated according to the same formula as VEFR (Equation 2).

2.4 | Statistical analysis

Statistical analysis was performed using IBM SPSS 27. Evaluation of normality was performed with Shapiro–Wilk's test. Normally distributed numerical variables were presented with arithmetic mean and standard deviation, while categorical variables were presented as absolute values and percentages (%). Statistical significance for intergroup differences was assessed by Student's *t*-test for numerical variables and by Pearson's χ^2 test for categorical variables. Repeated-measures ANOVA test was used to compare cerebral hemodynamic

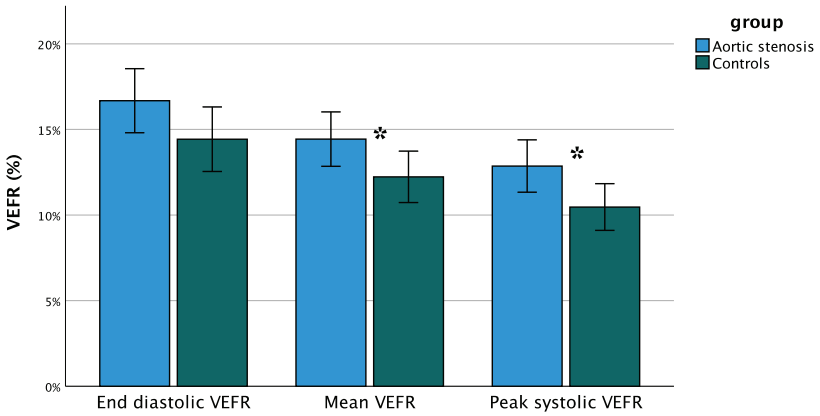

FIGURE 2 End diastolic VEFR, mean VEFR and peak systolic VEFR in both groups of participants presented as mean ± 2 SE. *Statistical significance computed from repeated-measures ANOVA. VEFR: visually evoked cerebral blood flow velocity response.

data by group. To evaluate for a possible habituation phenomenon, we performed multiple linear regression analysis on all cycles with cycle number as an independent variable. The limit of statistical significance was set at $p < .05$. Assuming a 5% SD for VEFR (Fabjan et al., 2015), a minimum of 40 patients per group was needed to detect a 3 % difference between groups at power of 80% and 5% alpha.

3 | RESULTS

3.1 | Baseline

Participants' characteristics are presented in Table 1. Groups were matched in age and sex. Patients with AS exhibited higher BMI values, higher incidence of arterial hypertension, and diabetes mellitus and were more likely to take beta blockers, ACEi, diuretics, and statins. There were no statistically significant differences in baseline Et-CO_2, left ventricular ejection fraction (LVEF), mean MCA, and PCA velocities among the two groups; however, controls had higher MAP values and lower HR (Table 1).

3.2 | Comparison of VEFR between groups

Patients with AS had significantly higher peak systolic and mean VEFR compared to age- and sex-matched controls, whereas only a tendency for higher end diastolic VEFR was found ($p = .064$) (Figure 2, Table 2). The most significant difference was observed in peak systolic VEFR ($p = .009$). As there was no difference in resting (phase OFF) PCA velocities between the groups, higher VEFR in AS group was contributed to higher PCA velocities during visual stimulation (phase ON) (Table S1). Moreover, higher relative PCA blood flow velocity changes were recorded in AS patients in the early phase of visual stimulation, however differences between groups did not reach statistical significance (Table S2).

TABLE 2 Relative cerebral blood flow velocity responses upon visual stimulation in patients with AS and controls.

	Aortic stenosis	Controls	*p* Value
Peak systolic VEFR (%)	12.9 (± 5.6)	10.5 (± 4.5)	.009*
Mean VEFR (%)	14.4 (± 5.8)	12.2 (± 4.9)	.021*
End diastolic VEFR (%)	16.7 (± 6.9)	14.4 (± 6.2)	.061
Δ Peak systolic MCA (%)	2.0 (± 2.4)	1.8 (± 2.4)	.775
Δ Mean MCA (%)	2.3 (± 2.4)	2.2 (± 2.8)	.987
Δ End diastolic MCA (%)	2.9 (± 3.4)	2.8 (± 3.9)	.971

AS: aortic stenosis, VEFR: visually evoked cerebral blood flow velocity response, PCA: posterior cerebral artery, MCA: medial cerebral artery. Peak systolic, mean, and end diastolic VEFR represent the relative changes in PCA velocities upon visual stimulation, while Δ peak systolic, Δ mean, and Δ end diastolic MCA represent the relative changes in MCA velocities. Values are displayed as mean ± SD. *p* Values represent ANOVA test results. *p value < .05 is considered statistically significant.

Average time trace of the peak systolic, mean and end diastolic PCA blood flow velocity response to the visual stimulus for a sample subject from the stenosis and control group is presented in Figure 3.

The relative MCA velocity changes were smaller compared to VEFR and were found to be no different between the AS group and control group (Table 2). During visual stimulation, MAP and Et-CO_2 did not change significantly between ON and OFF phases in both groups; however, there was a tendency for slightly higher HR during ON phase, which did not reach statistical significance ($p = .066$ and $p = .051$, respectively).

3.3 | Variability of repeated VEFR

Peak systolic VEFR at each consecutive cycle in both groups of participants are presented in Figure 4. As the differences in VEFR between groups do not answer the question, whether these can be contributed to different values of VEFR per se or to different trends of responses

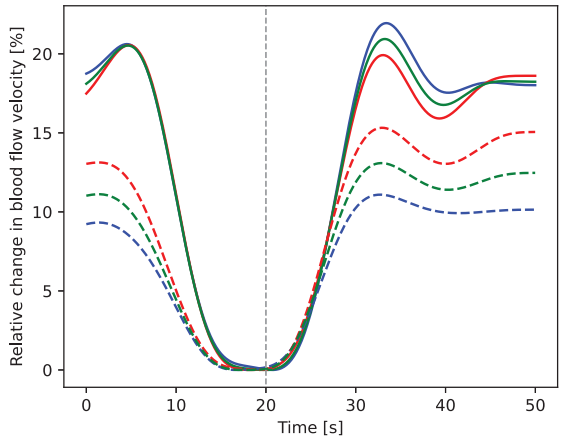

FIGURE 3 Visually evoked relative blood flow velocity time courses, averaged over 10 cycles for a sample subject from the aortic stenosis group (solid lines) and the control group (dashed lines). Blue lines represent peak systolic, green lines mean and red lines end diastolic values. The vertical dashed line at 20 s time represents the switch from OFF to the ON phase. PCA: posterior cerebral artery.

upon repetitive stimulation reflecting the habituation phenomenon, we performed multiple linear regression with VEFR as a dependent variable and cycle number and group as independent variables. Additionally, we added possible confounder variables (age, BMI, sex, smoking status) to obtain an adjusted model. There was no significant effect of cycle number to observed VEFR in none of the analyzed parameters. After adjustment for confounders, we obtained significant effect of group to peak systolic, mean and end diastolic VEFR ($p < .001$, Tables S3–S5).

4 | DISCUSSION

To the best of our knowledge, this is the first study to evaluate visually evoked cerebral blood flow velocity responses (VEFR) as a measure of neurovascular coupling (NVC) in patients with severe aortic valve stenosis (AS) using Transcranial Doppler Ultrasonography (TCD). The main finding of this research is that patients with severe AS exhibit higher VEFR than controls which may indicate dysregulation of NVC.

NVC is a dynamic process constantly orchestrating the balance between local cerebral perfusion to its regional metabolic needs. As a crucial component of CBF homeostasis, disturbances in NVC have critical consequences on the brain function (Iadecola, 2017). Insufficient blood supply on one side of the spectrum or hyperperfusion on the other can disturb O_2 delivery and be detrimental for neuronal function (Alosco et al., 2013; Rasmussen et al., 2015). The exaggerated hyperemic response can lead to an inappropriate increase in CBF in the metabolically active neuronal area, however at a cost of high energy expenditure, which is highly limited in the brain. The constant volume of intracranial blood volume implies that the cerebral blood overflow to active areas may lead to a shortage in vulnerable parts of the human brain, predisposing them to hypoperfusion. NVC dysregulation has been thoroughly studied in several pathological states such as traumatic brain injury, intracranial hemorrhage, migraine, cerebral ischemia and others (Fabjan et al., 2015; Hinzman et al., 2014; Koide et al., 2013; Rossetti et al., 2021; Zaletel et al., 2005). Furthermore, impairment of NVC has been suggested in various subgroups of patients with cardiac disease. A recent study in patients with atrial fibrillation reported on reduced cerebrovascular conductance upon visual stimulation when compared to age-matched healthy controls (Junejo et al., 2020). Moreover, NVC response assessed by second-order linear equation was found to be impaired in patients with heart failure with reduced ejection fraction (Aires et al., 2020). Even though, TCD was used in these two previous studies as well as in our study, the results might have differed due to diverse underlying cardiac pathology and data analysis.

Contrary to our expectations, patients with AS exhibited higher VEFR than controls. Episodes of intermittent cerebral hypoperfusion due to obstruction of blood outflow from the left ventricle are proposed as the main macro pathophysiological perturbation in aortic stenosis patients. This may in turn lead to structural and functional changes on the level of microcirculation, which is involved in NVC. Recent studies have shown that CBF measured by spin labeling MRI increased significantly after transcatheter aortic valve replacement, pointing out the possibility that CBF might indeed be diminished in severe AS patients (Vlastra et al., 2021). Reduced cerebral perfusion leads to hypoxia, which elicits a direct vascular effect and was shown to be associated with CBF changes (Willie et al., 2014). Some studies have revealed that hypoxia may lead to an increase in global CBF, while others have shown diminished regional CBF and reduction in the amplitude of NVC response during the hypoxic period (Ainslie & Subudhi, 2014; Lawley et al., 2017; Noth et al., 2008; Rossetti et al., 2021). How exactly intermittent hypoperfusion in AS affects NVC is not known yet. Our study was not designed to analyze individual components of NVC; however, an increased NVC response might in theory result from exaggerated hyperemic response to neuronal activity or increased neural excitability upon visual stimulation.

A possible mechanism in exaggerated hyperemic response could be increased sensitivity of endothelial cells to vasodilative stimuli. Various vasodilative molecules are believed to be involved in NVC such as nitric oxide, prostaglandins, epoxyeicosatrienoic acids, adenosine triphosphate, adenosine, H^+, and K^+ (Iadecola, 2017). An example of increased sensitivity of endothelial cells to vasodilative stimuli was presented in a study with familial migraine mice models, where increased hyperemic response was suggested to result from increased expression of inwardly rectifying potassium (Kir) channels on endothelial cells (Staehr et al., 2020). Kir channels promote K^+ efflux and hyperpolarization of the cell membrane, which through various signaling pathways results in smooth muscle relaxation and vasodilatation (Knot et al., 1996; Longden & Nelson, 2015). Increased susceptibility of mice to vasospasm due to a genetic defect was believed to initially cause cerebral hypoperfusion and accumulation of metabolic factors, which in turn stimulated the increased expression of Kir channels on the endothelial blood cells and their sensitivity to vasodilative

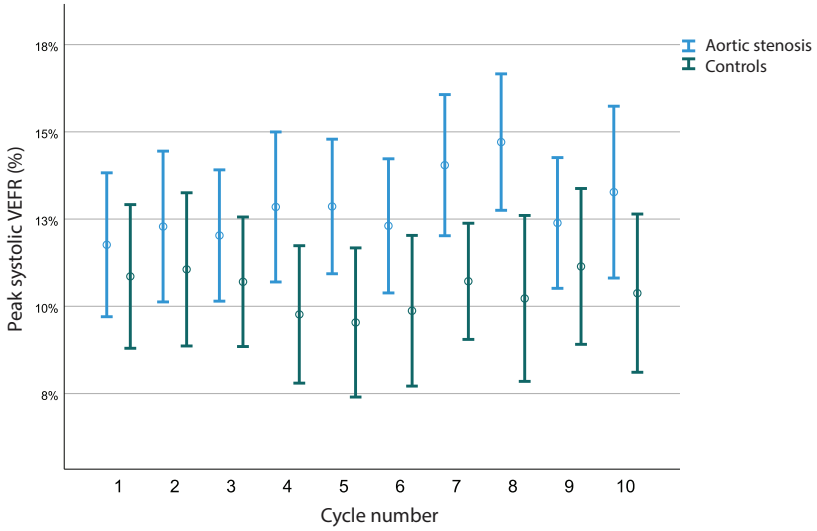

FIGURE 4 Peak systolic VEFR at each consecutive cycle in both groups of participants displayed as mean ± SD. VEFR: visually evoked cerebral blood flow velocity response.

stimuli (Staehr et al., 2020). Similarly, episodes of chronic cerebral hypoperfusion in AS patients may lead to the accumulation of vasodilative substances and translational changes on the cellular level, which results in an exaggerated hyperemic response.

An alternative explanation for the higher VEFR could be increased neural excitability upon visual stimulation. The only electroencephalographic (EEG) study up to now analyzing neuronal activity in AS showed EEG patterns indicating changes in the cerebral circulation provoked by compression of carotid arteries. These changes were present even in patients who had no history of neurological symptoms pointing towards a latent vascular lesion which becomes manifest during temporary cerebral hypoxia (Prusik & Bazika, 1968). Furthermore, a study by Vecchio et al. (2012) revealed that acute ischemic hypoxia due to a cardiovascular or pulmonary crisis in chronic heart failure patients may induce EEG changes. Whether these EEG changes described in acute settings can be translated to the setting of chronic intermittent hypoperfusion remains unclear. However, there has been no study up to date studying evoked potentials as a measure of neuronal activation in AS. We believe that this mechanism is less likely to be the cause of increased VEFR.

Nevertheless, we hypothesized that there may be another reason for the differences in VEFR. As the comparison of peak systolic, mean and end diastolic VEFR between groups was performed using VEFR from 10 consecutive cycles, different trends (ascending or descending) in the repeated VEFR could have contributed to the final higher VEFR value in AS group. The succeeding decline in the evoked cerebral blood flow responses upon repetitive stimulation reflecting habituation phenomenon has been described in healthy subjects (Obrig et al., 2002). Habituation is considered to reflect an adaptive cortical mechanism protecting from sensory overstimulation (Thompson et al., 1979) and lactate accumulation (Sappey-Marinier et al., 1992) as a response to sustained stimulus of equal intensity. A lack of habituation has been found in certain disease states which affect CBF regulation (Ambrosini et al., 2003). We used linear regression analysis, which showed no significant variability between the cycles in both groups that could support this hypothesis. Accordingly, lack of habituation is very unlikely to be the underlying explanation for higher VEFR in AS group.

Interestingly, there was no statistically significant difference in relative PCA blood flow velocity changes in the early phase of visual stimulation between groups, although the values tended to be higher in the AS group. The assessment of neurovascular coupling in our study was primarily based on the evaluation of the plateau phase of the visual blood flow velocity response in PCA (i.e., VEFR) to avoid the variability of the transitional phenomenon in the early phase. The method was found to be reliable and valid in previous literature (Boms et al., 2010; Fabjan et al., 2015; Fabjan et al., 2012; Olah et al., 2008), therefore the authors of this study used this methodology to answer the hypothesis according to the aim of our study.

The most prominent differences between groups were observed considering peak systolic VEFR compared to mean and end diastolic VEFR. Most studies use mean VEFR for blood flow velocity quantification, as peak systolic and end diastolic velocity indices describe the velocity extremes at two time points of one heart cycle, however they add valuable information on cerebrovascular hemodynamics. Functional TCD investigations demonstrated that the end diastolic blood flow velocity index may be more sensitive for changes in NVC mechanism than peak systolic velocity index, but is of no advantage if a stimulus is used that results in a clear blood flow velocity increase (Rosengarten et al., 2001), such as in case of visual stimulus used in this study. On the other hand, peak systolic velocity index is easier to obtain being less influenced by Doppler artifacts (Rosengarten et al., 2001). As it correlates with CBF in cardiac systole, these prominent differences between groups may be ascribed to peak systolic VEFR reflecting the pumping function of the heart, which is known to be disturbed in AS.

4.1 | Limitations

Several potential limitations need to be considered. As TCD measures blood flow velocity rather than absolute CBF, the measurements of blood flow velocity are only proportional to CBF in case of constant diameter of the insonated vessel. This can only be assumed on a short-term basis if the systemic parameters such as MAP, pH and $EtCO_2$ remain constant. Transformation of the data to relative values improves correlation between velocity and blood flow changes as well as gains independence of the measurements from the insonation angle. Another limitation were the differences in baseline patient characteristics that could not be matched between groups. One of the differences was medication intake, which could have a potential effect on neural firing and resting vessel tone. Subanalysis of our data did not show any relevant effect of medication intake on VEFR estimates (Table S6), which is in accordance with previous research (van Rijssel et al., 2022). However, only limited conclusions can be withdrawn as the study was not designed to evaluate the effect of different medication subgroups on VEFR estimates. Nonetheless, we believe that dissimilarities in patients' characteristics are not an important factor in the observed differences in VEFR between groups. Furthermore, we selected a homogenous group of patients with severe AS undergoing surgical aortic valve replacement, however, if these results can be generalized for the whole population of severe AS patients remains unknown.

5 | CONCLUSION

This study shows higher visually evoked cerebral blood flow velocity responses in aortic stenosis patients compared to controls, which may indicate dysregulation of neurovascular coupling. Episodes of intermittent cerebral hypoperfusion due to obstruction of blood outflow from the left ventricle are proposed as the main macro pathophysiological perturbation in aortic stenosis leading to structural and functional changes on the level of microcirculation involved in neurovascular coupling. Future research including assessment of cerebral autoregulation, regulation of cerebral blood flow by gasses and autononomic nervous system control in aortic stenosis patients is mandatory to better elucidate how obstruction of blood outflow from the left ventricle influences cerebral blood flow regulatory mechanisms.

AUTHOR CONTRIBUTIONS

All authors have made substantial contributions to the conception and design of the manuscript, acquisition of data, analysis and interpretation of data, drafting and critical revision of the article, and have approved the final version to be submitted.

CONFLICT OF INTEREST STATEMENT

The authors declare no conflicts of interest.

PATIENT CONSENT STATEMENT

A written consent was obtained from all the participants.

DATA AVAILABILITY STATEMENT

The data that support the findings of this study are available from the corresponding author upon request.

ORCID

Ana Ovsenik https://orcid.org/0000-0002-7307-5826
Martin Brešar https://orcid.org/0000-0002-1674-3314
Pavle Boškoski https://orcid.org/0000-0003-4498-0509
Andrej Fabjan https://orcid.org/0000-0001-8527-4948

PEER REVIEW

The peer review history for this article is available at https://publons.com/publon/10.1002/brb3.3155.

REFERENCES

Aaslid, R. (1987). Visually evoked dynamic blood flow response of the human cerebral circulation. *Stroke; A Journal of Cerebral Circulation*, *18*, 771–775. https://doi.org/10.1161/01.str.18.4.771

Abdul-Jawad Altisent, O., Ferreira-Gonzalez, I., Marsal, J. R., Ribera, A., Auger, C., Ortega, G., Cascant, P., Urena, M., Del Blanco, B. G., Serra, V., Sureda, C., Igual, A., Rovira, A., González-Alujas, M. T., Gonzalez, A., Puri, R., Cuellar, H., Tornos, P., Rodés-Cabau, J., & Garcia-Dorado, D. (2016). Neurological damage after transcatheter aortic valve implantation compared with surgical aortic valve replacement in intermediate risk patients. *Clinical Research in Cardiology*, *105*, 508–517. https://doi.org/10.1007/s00392-015-0946-9

Ainslie, P. N., & Subudhi, A. W. (2014). Cerebral blood flow at high altitude. *High Altitude Medicine & Biology*, *15*, 133–140. https://doi.org/10.1089/ham.2013.1138

Aires, A., Andrade, A., Azevedo, E., Gomes, F., Araújo, J. P., & Castro, P. (2020). Neurovascular coupling impairment in heart failure with reduction ejection fraction. *Brain Sciences*, *10*, 714. https://doi.org/10.3390/brainsci10100714

Alosco, M. L., Gunstad, J., Jerskey, B. A., Xu, X., Clark, U. S., Hassenstab, J., Cote, D. M., Walsh, E. G., Labbe, D. R., Hoge, R., Cohen, R. A., & Sweet, L. H. (2013). The adverse effects of reduced cerebral perfusion on cognition and brain structure in older adults with cardiovascular disease. *Brain and Behavior*, *3*, 626–636. https://doi.org/10.1002/brb3.171

Ambrosini, A. (2003). Lack of habituation causes high intensity dependence of auditory evoked cortical potentials in migraine. *Brain*, *126*, 2009–2015. https://doi.org/10.1093/brain/awg206

Beyersdorf, F., Vahanian, A., Milojevic, M., Praz, F., Baldus, S., Bauersachs, J., Capodanno, D., Conradi, L., De Bonis, M., De Paulis, R., Delgado, V., Freemantle, N., Gilard, M., Haugaa, K. H., Jeppsson, A., Jüni, P., Pierard, L., Prendergast, B. D., Sádaba, J. R., … Wojakowski, W. (2021). 2021 ESC/EACTS Guidelines for the management of valvular heart disease. *European Journal of Cardio-Thoracic Surgery*, *60*, 727–800. https://doi.org/10.1093/ejcts/ezab389

Boms, N., Yonai, Y., Molnar, S., Rosengarten, B., Bornstein, N. M., Csiba, L., & Olah, L. (2010). Effect of smoking cessation on visually evoked cerebral blood flow response in healthy volunteers. *Journal of Vascular Research*, *47*, 214–220. https://doi.org/10.1159/000255964

Fabjan, A., Bajrović, F. F., Musizza, B., Vidmar, J., Štrucl, M., & Zaletel, M. (2015). Study of neurovascular coupling during cold pressor test in patients with migraine. *Cephalalgia*, *35*, 692–701. https://doi.org/10.1177/0333102414554661

Fabjan, A., Musizza, B., Bajrović, F. F., Zaletel, M., & Štrucl, M. (2012). The effect of the cold pressor test on a visually evoked cerebral blood flow velocity response. *Ultrasound in Medicine & Biology*, *38*, 13–20. https://doi.org/10.1016/j.ultrasmedbio.2011.10.007

Girouard, H., & Iadecola, C. (2006). Neurovascular coupling in the normal brain and in hypertension, stroke, and Alzheimer disease. *Journal of Applied Physiology (1985)*, *100*, 328–335. https://doi.org/10.1152/japplphysiol.00966.2005

Hinzman, J. M., Andaluz, N., Shutter, L. A., Okonkwo, D. O., Pahl, C., Strong, A. J., Dreier, J. P., & Hartings, J. A. (2014). Inverse neurovascular coupling to cortical spreading depolarizations in severe brain trauma. *Brain*, *137*, 2960–2972. https://doi.org/10.1093/brain/awu241

Iadecola, C. (2017). The Neurovascular unit coming of age: A journey through neurovascular coupling in health and disease. *Neuron*, *96*, 17–42. https://doi.org/10.1016/j.neuron.2017.07.030

Joseph, J., Naqvi, S. Y., Giri, J., & Goldberg, S. (2017). Aortic stenosis: Pathophysiology, diagnosis, and therapy. *American Journal of Medicine*, *130*, 253–263. https://doi.org/10.1016/j.amjmed.2016.10.005

Junejo, R. T., Braz, I. D., Lucas, S. J., Van Lieshout, J. J., Phillips, A. A., Lip, G. Y., & Fisher, J. P. (2020). Neurovascular coupling and cerebral autoregulation in atrial fibrillation. *Journal of Cerebral Blood Flow and Metabolism*, *40*, 1647–1657. https://doi.org/10.1177/0271678X19870770

Kleczyński, P., Petkow Dimitrow, P., Dziewierz, A., Surdacki, A., & Dudek, D. (2017). Transcatheter aortic valve implantation improves carotid and vertebral arterial blood flow in patients with severe aortic stenosis: Practical role of orthostatic stress test. *Clinical Cardiology*, *40*, 492–497. https://doi.org/10.1002/clc.22684

Knot, H. J., Zimmermann, P. A., & Nelson, M. T. (1996). Extracellular K(+)-induced hyperpolarizations and dilatations of rat coronary and cerebral arteries involve inward rectifier K(+) channels. *The Journal of Physiology*, *492*(2), 419–430. https://doi.org/10.1113/jphysiol.1996.sp021318

Koide, M., Sukhotinsky, I., Ayata, C., & Wellman, G. C. (2013). Subarachnoid hemorrhage, spreading depolarizations and impaired neurovascular coupling. *Stroke Research and Treatment*, *2013*, 1. https://doi.org/10.1155/2013/819340

Lawley, J. S., Macdonald, J. H., Oliver, S. J., & Mullins, P. G. (2017). Unexpected reductions in regional cerebral perfusion during prolonged hypoxia. *The Journal of Physiology*, *595*, 935–947. https://doi.org/10.1113/JP272557

Longden, T. A., & Nelson, M. T. (2015). Vascular inward rectifier K+ channels as external K+ sensors in the control of cerebral blood flow. *Microcirculation*, *22*, 183–196. https://doi.org/10.1111/micc.12190

Nöth, U., Kotajima, F., Deichmann, R., Turner, R., & Corfield, D. R. (2008). Mapping of the cerebral vascular response to hypoxia and hypercapnia using quantitative perfusion MRI at 3 T. *Nmr in Biomedicine*, *21*, 464–472. https://doi.org/10.1002/nbm.1210

Obrig, H., Israel, H., Kohl-Bareis, M., Uludag, K., Wenzel, R., Müller, B., Arnold, G., & Villringer, A. (2002). Habituation of the visually evoked potential and its vascular response: Implications for neurovascular coupling in the healthy adult. *Neuroimage*, *17*, 1–18. https://doi.org/10.1006/nimg.2002.1177

Oláh, L., Raiter, Y., Candale, C., Molnár, S., Rosengarten, B., Bornstein, N., & Csiba, L. (2008). Visually evoked cerebral vasomotor response in smoking and nonsmoking young adults, investigated by functional transcranial Doppler. *Nicotine & Tobacco Research*, *10*, 353–358. https://doi.org/10.1080/14622200701825874

Ovsenik, A., Podbregar, M., & Fabjan, A. (2021). Cerebral blood flow impairment and cognitive decline in heart failure. *Brain and Behavior*, *11*, e02176. https://doi.org/10.1002/brb3.2176

Panczel, G., Daffertshofer, M., Ries, S., Spiegel, D., & Hennerici, M. (1999). Age and stimulus dependency of visually evoked cerebral blood flow responses. *Stroke; A Journal of Cerebral Circulation*, *30*, 619–623. https://doi.org/10.1161/01.str.30.3.619

Phillips, A. A., Chan, F. H., Zheng, M. M. Z., Krassioukov, A. V., & Ainslie, P. N. (2016). Neurovascular coupling in humans: Physiology, methodological advances and clinical implications. *Journal of Cerebral Blood Flow and Metabolism*, *36*, 647–664. https://doi.org/10.1177/0271678X15617954

Prusík, B., & Bazika, V. (1968). Aortic stenosis in aged patients. Electroencephalographic trial. *Angiologica*, *5*, 49–54. https://doi.org/10.1159/000157733

Rashedi, N., & Otto, C. M. (2015). Aortic stenosis: Changing disease concepts. *Journal of Cardiovascular Ultrasound*, *23*, 59–69. https://doi.org/10.4250/jcu.2015.23.2.59

Rasmussen, P. M., Jespersen, S. N., & Østergaard, L. (2015). The effects of transit time heterogeneity on brain oxygenation during rest and functional activation. *Journal of Cerebral Blood Flow and Metabolism*, *35*, 432–442. https://doi.org/10.1038/jcbfm.2014.213

Rosengarten, B., Aldinger, C., Kaufmann, A., & Kaps, M. (2001). Comparison of visually evoked peak systolic and end diastolic blood flow velocity using a control system approach. *Ultrasound in Medicine & Biology*, *27*, 1499–1503. https://doi.org/10.1016/s0301-5629(01)00464-1

Rossetti, G. M., D'avossa, G., Rogan, M., Macdonald, J. H., Oliver, S. J., & Mullins, P. G. (2021). Reversal of neurovascular coupling in the default mode network: Evidence from hypoxia. *Journal of Cerebral Blood Flow and Metabolism*, *41*, 805–818. https://doi.org/10.1177/0271678X20930827

Sappey-Marinier, D., Calabrese, G., Fein, G., Hugg, J. W., Biggins, C., & Weiner, M. W. (1992). Effect of photic stimulation on human visual cortex lactate and phosphates using 1H and 31P magnetic resonance spectroscopy. *Journal of Cerebral Blood Flow and Metabolism*, *12*, 584–592. https://doi.org/10.1038/jcbfm.1992.82

Staehr, C., Rajanathan, R., Postnov, D. D., Hangaard, L., Bouzinova, E. V., Lykke-Hartmann, K., Bach, F. W., Sandow, S. L., Aalkjaer, C., & Matchkov, V. V. (2020). Abnormal neurovascular coupling as a cause of excess cerebral vasodilation in familial migraine. *Cardiovascular Research*, *116*, 2009–2020. https://doi.org/10.1093/cvr/cvz306

Thompson, R. F., Berry, S. D., Rinaldi, P. C., Bhatnagar, S., Clayton, D. F., Colombo, J., Coppola, G., Geyer, M. A., Glanzman, D. L., Marsland, S., McSweeney, F. K., Wilson, D. A., Wu, C. F., & Thompson, R. F. (1979). Habituation and the orienting reflex: The dual-process theory revisited. In H. D. Kimmel, E. H. van Olst, & J. H. Orlebeke (Eds.), *The orienting reflex in humans* (pp. 21–60) L. Erlbaum Associates, distributed by Halsted Press Language.

Toth, P., Tarantini, S., Csiszar, A., & Ungvari, Z. (2017). Functional vascular contributions to cognitive impairment and dementia: Mechanisms and consequences of cerebral autoregulatory dysfunction, endothelial impairment, and neurovascular uncoupling in aging. *American Journal of Physiology. Heart and Circulatory Physiology*, *312*, H1–H20. https://doi.org/10.1152/ajpheart.00581.2016

Van Rijssel, A. E., Stins, B. C., Beishon, L. C., Sanders, M. L., Quinn, T. J., Claassen, J. A. H. R., & De Heus, R. A. A. (2022). Effect of antihypertensive treatment on cerebral blood flow in older adults: A systematic review and meta-analysis. *Hypertension*, *79*, 1067–1078. https://doi.org/10.1161/HYPERTENSIONAHA.121.18255

Vecchio, F., Valeriani, L., Buffo, P., Scarpellini, M. G., Frisoni, G. B., Mecarelli, O., Babiloni, C., & Rossini, P. M. (2012). Cortical sources of EEG rhythms in congestive heart failure and Alzheimer's disease. *International Journal of Psychophysiology*, *86*, 98–107. https://doi.org/10.1016/j.ijpsycho.2012.06.053

Vlastra, W., Nieuwkerk, A. C., Bronzwaer, A.-S. G. T., Versteeg, A., Bron, E. E., Niessen, W. J., Mutsaerts, H. J. M. M., Ster, B. J. P., Majoie, C. B. L. M., Biessels, G. J., Nederveen, A. J., Daemen, M. J. A. P., Osch, M. J. P., Baan, J., Piek, J. J., Van Lieshout, J. J., & Delewi, R. (2021). Cerebral blood flow in patients with severe aortic valve stenosis undergoing transcatheter aortic valve implantation. *Journal of the American Geriatrics Society*, *69*, 494–499. https://doi.org/10.1111/jgs.16882

Willie, C. K., Colino, F. L., Bailey, D. M., Tzeng, Y. C., Binsted, G., Jones, L. W., Haykowsky, M. J., Bellapart, J., Ogoh, S., Smith, K. J., Smirl, J. D., Day, T. A., Lucas, S. J., Eller, L. K., & Ainslie, P. N. (2011). Utility of transcranial Doppler ultrasound for the integrative assessment of cerebrovascular function. *Journal of Neuroscience Methods*, *196*, 221–237. https://doi.org/10.1016/j.jneumeth.2011.01.011

Willie, C. K., Tzeng, Y.-C., Fisher, J. A., & Ainslie, P. N. (2014). Integrative regulation of human brain blood flow. *The Journal of Physiology*, *592*, 841–859. https://doi.org/10.1113/jphysiol.2013.268953

Zaletel, M., Strucl, M., Bajrovi, F., & Pogacnik, T. (2005). Coupling between visual evoked cerebral blood flow velocity responses and visual evoked potentials in migraneurs. *Cephalalgia*, *25*, 567–574. https://doi.org/10.1111/j.1468-2982.2005.00918.x

SUPPORTING INFORMATION

Additional supporting information can be found online in the Supporting Information section at the end of this article.

How to cite this article: Ovsenik, A., Podbregar, M., Lakič, N., Brešar, M., Boskoski, P., Verdenik, I., & Fabjan, A. (2023). Neurovascular coupling in severe aortic valve stenosis. *Brain and Behavior*, *13*, e3155. https://doi.org/10.1002/brb3.3155

Chapter 7

Conclusions

In conclusion, the findings of this dissertation are discussed in relation to the initial hypotheses. Let us summarize them:

1. In an ideal situation of infinite time series length, the value of the coupling strength exactly determines the information flow between subsystems.

2. The accuracy of the state space based approaches for directional coupling detection can be improved with the method of cross-distance vectors, resulting in a smaller probability of a false positive result.

3. Combining the improved state space measure with surrogate data increases its reliability in inferring the true coupling direction.

4. The index calculated from time series of a perturbation experiment is able to detect a difference between two groups in a clinical study.

The first hypothesis is partially true. Recall that the coupling strength exactly determines the information flow if it increases monotonically with increased coupling strength. In this case, the inverse problem of inferring the coupling strength is solvable. Analysis has shown that information flow between two systems can, in fact, increase monotonically with increased coupling strength for sufficiently weak coupling. This is possible when the response subsystem remains in an orbit around the same attractor and does not transition to a different attractor when coupled. Additionally, if the coupling is diffusive, the information flow decreases monotonically if coupling strength is large enough. Thus, the inverse problem is also solvable given the coupling is strong enough. In conclusion, the inverse problem is solvable, but only in specific scenarios.

A thorough analysis of the accuracy of different state space measures shows that the second hypothesis is confirmed. By computing the cross-distance vectors $\boldsymbol{v}$, the effect of coupling on the closeness of the conditioned nearest neighbors becomes apparent. Specifically, the effect is visible only on some of the closest conditioned nearest neighbors, which is seen as an initial tail in the cross-distance vectors. Quantifying the initial tail results in the coupling index c, which has a substantially reduced risk of resulting in a false positive.

Regarding the third hypothesis, combining the improved state space measure c with surrogate data is not as straightforward as initially thought. It turns out that the new coupling indices obtained from the cross-distance vectors are influenced by the distribution of distances between pairs of embedding vectors of a time series. Because the surrogates have different distributions of these distances than the original signal, this leads to an inequitable comparison of values obtained from the original time series to those obtained from the surrogates. To account for this, a rank-based measure c^r is introduced. It has

all the positive aspects of the measure c but is obtained from ranks instead of distances. Because the distribution of ranks is identical for all time series, including the surrogates, comparing the original values of c^r to the surrogate values of c^r is equitable.

The third hypothesis is confirmed by applying the new rank-based measure c^r and surrogates to an EEG database. The obtained values of c^r are very similar between the focal and the nonfocal signals. Including surrogates in the analysis breaks this similarity. It results in more frequent detection of nonlinear interdependence in the focal signals, revealing the true dynamics. Furthermore, the new measure c^r has an increased ability to differentiate between the focal and the nonfocal signals, showing an increased potential in clinical applications.

Finally, the fourth hypothesis is confirmed. An analysis of the time series measured during the perturbation experiment successfully resulted in the quantification of neurovascular coupling. A statistically significant difference between the AS group and the healthy control group was found, indicating a dysregulation of neurovascular coupling in patients with AS. This shows that computing VEFR can effectively distinguish between the aortic stenosis group and the healthy control group. However, contrary to the initial expectations, the AS group exhibited stronger neurovascular coupling than the healthy control group. The dysregulation of neurovascular coupling in patients with AS is therefore signified by an increase in coupling strength.

References

[1] T. E. Dick, Y.-H. Hsieh, R. R. Dhingra, *et al.*, "Cardiorespiratory coupling," in *The Central Nervous System Control of Respiration*. Elsevier, 2014, pp. 191–205. DOI: 10.1016/b978-0-444-63274-6.00010-2.

[2] C. W. J. Granger, "Investigating causal relations by econometric models and cross-spectral methods," *Econometrica*, vol. 37, no. 3, pp. 424–438, Aug. 1969, ISSN: 0012-9682. DOI: 10.2307/1912791.

[3] S. Z. Chiou-Wei, C.-F. Chen, and Z. Zhu, "Economic growth and energy consumption revisited — evidence from linear and nonlinear granger causality," *Energy Economics*, vol. 30, no. 6, pp. 3063–3076, Nov. 2008, ISSN: 0140-9883. DOI: 10.1016/j.eneco.2008.02.002.

[4] P. Jizba, H. Kleinert, and M. Shefaat, "Rényi's information transfer between financial time series," *Physica A: Statistical Mechanics and its Applications*, vol. 391, no. 10, pp. 2971–2989, May 2012, ISSN: 0378-4371. DOI: 10.1016/j.physa.2011.12.064.

[5] G. Sugihara, R. May, H. Ye, *et al.*, "Detecting causality in complex ecosystems," *Science*, vol. 338, no. 6106, pp. 496–500, Oct. 2012, ISSN: 1095-9203. DOI: 10.1126/science.1227079.

[6] E. A. Bender, T. J. Case, and M. E. Gilpin, "Perturbation experiments in community ecology: Theory and practice," *Ecology*, vol. 65, no. 1, pp. 1–13, Feb. 1984, ISSN: 1939-9170. DOI: 10.2307/1939452.

[7] L. W. Sheppard, V. Vuksanović, P. V. E. McClintock, and A. Stefanovska, "Oscillatory dynamics of vasoconstriction and vasodilation identified by time-localized phase coherence," *Physics in Medicine and Biology*, vol. 56, no. 12, pp. 3583–3601, May 2011, ISSN: 1361-6560. DOI: 10.1088/0031-9155/56/12/009.

[8] M. Paluš, V. Komárek, Z. Hrnčíř, and K. Štěrbová, "Synchronization as adjustment of information rates: Detection from bivariate time series," *Physical Review E*, vol. 63, no. 4, 046211, Mar. 2001, ISSN: 1095-3787. DOI: 10.1103/physreve.63.046211.

[9] R. G. Andrzejak, K. Schindler, and C. Rummel, "Nonrandomness, nonlinear dependence, and nonstationarity of electroencephalographic recordings from epilepsy patients," *Physical Review E*, vol. 86, no. 4, 046206, Oct. 2012, ISSN: 1550-2376. DOI: 10.1103/physreve.86.046206.

[10] N. Boms, Y. Yonai, S. Molnar, *et al.*, "Effect of smoking cessation on visually evoked cerebral blood flow response in healthy volunteers," *Journal of Vascular Research*, vol. 47, no. 3, pp. 214–220, Nov. 2009, ISSN: 1423-0135. DOI: 10.1159/000255964.

[11] E. M. Izhikevich, *Dynamical Systems in Neuroscience: The Geometry of Excitability and Bursting*. The MIT Press, 2006, ISBN: 9780262276078. DOI: 10.7551/mitpress/2526.001.0001.

[12] T. Bossomaier, L. Barnett, M. Harré, and J. T. Lizier, *An Introduction to Transfer Entropy*. Springer International Publishing, 2016, ISBN: 9783319432229. DOI: 10.1007/978-3-319-43222-9.

[13] E. Pereda, R. Q. Quiroga, and J. Bhattacharya, "Nonlinear multivariate analysis of neurophysiological signals," *Progress in Neurobiology*, vol. 77, no. 1–2, pp. 1–37, Sep. 2005, ISSN: 0301-0082. DOI: 10.1016/j.pneurobio.2005.10.003.

[14] T. J. Mosedale, D. B. Stephenson, M. Collins, and T. C. Mills, "Granger causality of coupled climate processes: Ocean feedback on the north atlantic oscillation," *Journal of Climate*, vol. 19, no. 7, pp. 1182–1194, Apr. 2006, ISSN: 0894-8755. DOI: 10.1175/jcli3653.1.

[15] L. A. (Cox and D. A. Popken, "Has reducing fine particulate matter and ozone caused reduced mortality rates in the united states?" *Annals of Epidemiology*, vol. 25, no. 3, pp. 162–173, Mar. 2015, ISSN: 1047-2797. DOI: 10.1016/j.annepidem.2014.11.006.

[16] S. H. Strogatz, *Nonlinear Dynamics and Chaos*. CRC Press, May 2018, ISBN: 9780429961113. DOI: 10.1201/9780429492563.

[17] E. Ott, *Chaos in Dynamical Systems*. Cambridge University Press, Aug. 2002, ISBN: 9780511803260. DOI: 10.1017/cbo9780511803260.

[18] S. Širca and M. Horvat, *Computational Methods in Physics*. Springer International Publishing, 2018, ISBN: 9783319786193. DOI: 10.1007/978-3-319-78619-3.

[19] O. Rössler, "An equation for continuous chaos," *Physics Letters A*, vol. 57, no. 5, pp. 397–398, Jul. 1976, ISSN: 0375-9601. DOI: 10.1016/0375-9601(76)90101-8.

[20] A. Pikovsky, M. Rosenblum, and J. Kurths, *Synchronization: A Universal Concept in Nonlinear Sciences*. Cambridge University Press, Oct. 2001, ISBN: 9780511755743. DOI: 10.1017/cbo9780511755743.

[21] G. Benettin, L. Galgani, A. Giorgilli, and J.-M. Strelcyn, "Lyapunov characteristic exponents for smooth dynamical systems and for hamiltonian systems; a method for computing all of them. part 1: Theory," *Meccanica*, vol. 15, no. 1, pp. 9–20, Mar. 1980, ISSN: 1572-9648. DOI: 10.1007/bf02128236.

[22] T. Stankovski, T. Pereira, P. V. McClintock, and A. Stefanovska, "Coupling functions: Universal insights into dynamical interaction mechanisms," *Reviews of Modern Physics*, vol. 89, no. 4, 045001, Nov. 2017, ISSN: 1539-0756. DOI: 10.1103/revmodphys.89.045001.

[23] D. Eroglu, J. S. W. Lamb, and T. Pereira, "Synchronisation of chaos and its applications," *Contemporary Physics*, vol. 58, no. 3, pp. 207–243, Jul. 2017, ISSN: 1366-5812. DOI: 10.1080/00107514.2017.1345844.

[24] S. Mallat, *A Wavelet Tour of Signal Processing*. Academic Press, 1998, ISBN: 0124666051. DOI: 10.1016/B978-0-12-374370-1.X0001-8.

[25] M. G. Rosenblum, A. S. Pikovsky, and J. Kurths, "Phase synchronization of chaotic oscillators," *Physical Review Letters*, vol. 76, no. 11, pp. 1804–1807, Mar. 1996, ISSN: 1079-7114. DOI: 10.1103/physrevlett.76.1804.

[26] N. F. Rulkov, M. M. Sushchik, L. S. Tsimring, and H. D. I. Abarbanel, "Generalized synchronization of chaos in directionally coupled chaotic systems," *Physical Review E*, vol. 51, no. 2, pp. 980–994, Feb. 1995, ISSN: 1095-3787. DOI: 10.1103/physreve.51.980.

[27] L. Kocarev and U. Parlitz, "Generalized synchronization, predictability, and equivalence of unidirectionally coupled dynamical systems," *Physical Review Letters*, vol. 76, no. 11, pp. 1816–1819, Mar. 1996, ISSN: 1079-7114. DOI: 10.1103/physrevlett.76.1816.

[28] L. M. Pecora and T. L. Carroll, "Synchronization of chaotic systems," *Chaos: An Interdisciplinary Journal of Nonlinear Science*, vol. 25, no. 9, 097611, Apr. 2015, ISSN: 1089-7682. DOI: 10.1063/1.4917383.

[29] H. D. I. Abarbanel, N. F. Rulkov, and M. M. Sushchik, "Generalized synchronization of chaos: The auxiliary system approach," *Physical Review E*, vol. 53, no. 5, pp. 4528–4535, May 1996, ISSN: 1095-3787. DOI: 10.1103/physreve.53.4528.

[30] F. Takens, "Detecting strange attractors in turbulence," in *Dynamical Systems and Turbulence, Warwick 1980*. Springer Berlin Heidelberg, 1981, pp. 366–381, ISBN: 9783540389453. DOI: 10.1007/bfb0091924.

[31] A. M. Fraser and H. L. Swinney, "Independent coordinates for strange attractors from mutual information," *Physical Review A*, vol. 33, no. 2, pp. 1134–1140, Feb. 1986, ISSN: 0556-2791. DOI: 10.1103/physreva.33.1134.

[32] N. Wiener, *The Theory of Prediction: Modern Mathematics for the Engineer*. ed. E. F. Beckenbach, New York: McGraw-Hill, 1956, ISBN: 0486497461.

[33] A. Shojaie and E. B. Fox, "Granger causality: A review and recent advances," *Annual Review of Statistics and Its Application*, vol. 9, no. 1, pp. 289–319, Mar. 2022, ISSN: 2326-831X. DOI: 10.1146/annurev-statistics-040120-010930.

[34] Y. Hong, Y. Liu, and S. Wang, "Granger causality in risk and detection of extreme risk spillover between financial markets," *Journal of Econometrics*, vol. 150, no. 2, pp. 271–287, Jun. 2009, ISSN: 0304-4076. DOI: 10.1016/j.jeconom.2008.12.013.

[35] F. Mormann, K. Lehnertz, P. David, and C. E. Elger, "Mean phase coherence as a measure for phase synchronization and its application to the eeg of epilepsy patients," *Physica D: Nonlinear Phenomena*, vol. 144, no. 3–4, pp. 358–369, Oct. 2000, ISSN: 0167-2789. DOI: 10.1016/s0167-2789(00)00087-7.

[36] M. G. Rosenblum and A. S. Pikovsky, "Detecting direction of coupling in interacting oscillators," *Physical Review E*, vol. 64, no. 4, 045202, Sep. 2001, ISSN: 1095-3787. DOI: 10.1103/physreve.64.045202.

[37] D. S. Bloomfield, R. T. J. McAteer, B. W. Lites, P. G. Judge, M. Mathioudakis, and F. P. Keenan, "Wavelet phase coherence analysis: Application to a quiet-sun magnetic element," *The Astrophysical Journal*, vol. 617, no. 1, pp. 623–632, Dec. 2004, ISSN: 1538-4357. DOI: 10.1086/425300.

[38] T. M. Cover and J. A. Thomas, *Elements of Information Theory*. Wiley, Apr. 2005, ISBN: 9780471748823. DOI: 10.1002/047174882x.

[39] K. E. Petersen, *Ergodic Theory*. Cambridge University Press, May 1983, ISBN: 9780511608728. DOI: 10.1017/cbo9780511608728.

[40] T. Schreiber, "Measuring information transfer," *Physical Review Letters*, vol. 85, no. 2, pp. 461–464, Jul. 2000, ISSN: 1079-7114. DOI: 10.1103/physrevlett.85.461.

[41] M. Paluš and M. Vejmelka, "Directionality of coupling from bivariate time series: How to avoid false causalities and missed connections," *Physical Review E*, vol. 75, no. 5, 056211, May 2007, ISSN: 1550-2376. DOI: 10.1103/physreve.75.056211.

[42] K. Hlaváčková-Schindler, M. Paluš, M. Vejmelka, and J. Bhattacharya, "Causality detection based on information-theoretic approaches in time series analysis," *Physics Reports*, vol. 441, no. 1, pp. 1–46, Mar. 2007, ISSN: 0370-1573. DOI: 10.1016/j.physrep.2006.12.004.

[43] J. Runge, J. Heitzig, V. Petoukhov, and J. Kurths, "Escaping the curse of dimensionality in estimating multivariate transfer entropy," *Physical Review Letters*, vol. 108, no. 25, 258701, Jun. 2012, ISSN: 1079-7114. DOI: 10.1103/physrevlett.108.258701.

[44] S. J. Schiff, P. So, T. Chang, R. E. Burke, and T. Sauer, "Detecting dynamical interdependence and generalized synchrony through mutual prediction in a neural ensemble," *Physical Review E*, vol. 54, no. 6, pp. 6708–6724, Dec. 1996, ISSN: 1095-3787. DOI: 10.1103/physreve.54.6708.

[45] M. Le Van Quyen, J. Martinerie, C. Adam, and F. J. Varela, "Nonlinear analyses of interictal eeg map the brain interdependences in human focal epilepsy," *Physica D: Nonlinear Phenomena*, vol. 127, no. 3–4, pp. 250–266, Mar. 1999, ISSN: 0167-2789. DOI: 10.1016/s0167-2789(98)00258-9.

[46] J. Arnhold, P. Grassberger, K. Lehnertz, and C. Elger, "A robust method for detecting interdependences: Application to intracranially recorded eeg," *Physica D: Nonlinear Phenomena*, vol. 134, no. 4, pp. 419–430, Dec. 1999, ISSN: 0167-2789. DOI: 10.1016/s0167-2789(99)00140-2.

[47] R. G. Andrzejak, A. Kraskov, H. Stögbauer, F. Mormann, and T. Kreuz, "Bivariate surrogate techniques: Necessity, strengths, and caveats," *Physical Review E*, vol. 68, no. 6, 066202, Dec. 2003, ISSN: 1095-3787. DOI: 10.1103/physreve.68.066202.

[48] D. Chicharro and R. G. Andrzejak, "Reliable detection of directional couplings using rank statistics," *Physical Review E*, vol. 80, no. 2, 026217, Aug. 2009, ISSN: 1550-2376. DOI: 10.1103/physreve.80.026217.

[49] J. Theiler, "Spurious dimension from correlation algorithms applied to limited time-series data," *Physical Review A*, vol. 34, no. 3, pp. 2427–2432, Sep. 1986, ISSN: 0556-2791. DOI: 10.1103/physreva.34.2427.

[50] J. Theiler, S. Eubank, A. Longtin, B. Galdrikian, and J. D. Farmer, "Testing for nonlinearity in time series: The method of surrogate data," *Physica D: Nonlinear Phenomena*, vol. 58, no. 1-4, pp. 77–94, 1992.

[51] T. Schreiber and A. Schmitz, "Surrogate time series," *Physica D: Nonlinear Phenomena*, vol. 142, no. 3–4, pp. 346–382, Aug. 2000, ISSN: 0167-2789. DOI: 10.1016/s0167-2789(00)00043-9.

[52] G. Lancaster, D. Iatsenko, A. Pidde, V. Ticcinelli, and A. Stefanovska, "Surrogate data for hypothesis testing of physical systems," *Physics Reports*, vol. 748, pp. 1–60, Jul. 2018, ISSN: 0370-1573. DOI: 10.1016/j.physrep.2018.06.001.

[53] E. N. Lorenz, "Deterministic nonperiodic flow," *Journal of the Atmospheric Sciences*, vol. 20, no. 2, pp. 130–141, Mar. 1963, ISSN: 1520-0469. DOI: 10.1175/1520-0469(1963)020<0130:dnf>2.0.co;2.

[54] J. F. Geweke, "Measures of conditional linear dependence and feedback between time series," *Journal of the American Statistical Association*, vol. 79, no. 388, pp. 907–915, Dec. 1984, ISSN: 1537-274X. DOI: 10.1080/01621459.1984.10477110.

[55] S. Guo, A. K. Seth, K. M. Kendrick, C. Zhou, and J. Feng, "Partial granger causality—eliminating exogenous inputs and latent variables," *Journal of Neuroscience Methods*, vol. 172, no. 1, pp. 79–93, Jul. 2008, ISSN: 0165-0270. DOI: 10.1016/j.jneumeth.2008.04.011.

[56] L. A. Baccalá and K. Sameshima, "Partial directed coherence: A new concept in neural structure determination," *Biological Cybernetics*, vol. 84, no. 6, pp. 463–474, May 2001, ISSN: 0340-1200. DOI: 10.1007/pl00007990.

[57] J. Sun and E. M. Bollt, "Causation entropy identifies indirect influences, dominance of neighbors and anticipatory couplings," *Physica D: Nonlinear Phenomena*, vol. 267, pp. 49–57, Jan. 2014, ISSN: 0167-2789. DOI: 10.1016/j.physd.2013.07.001.

[58] J. Runge, P. Nowack, M. Kretschmer, S. Flaxman, and D. Sejdinovic, "Detecting and quantifying causal associations in large nonlinear time series datasets," *Science Advances*, vol. 5, no. 11, eaau4996, Nov. 2019, ISSN: 2375-2548. DOI: 10.1126/sciadv.aau4996.

[59] P. Yodzis, "Food webs and perturbation experiments: Theory and practice," in *Food Webs: Integration of Patterns & Dynamics*. Springer US, 1996, pp. 192–200, ISBN: 978-1-4615-7007-3. DOI: 10.1007/978-1-4615-7007-3_19.

[60] E. J. Molinelli, A. Korkut, W. Wang, *et al.*, "Perturbation biology: Inferring signaling networks in cellular systems," *PLoS Computational Biology*, vol. 9, no. 12, e1003290, Dec. 2013, ISSN: 1553-7358. DOI: 10.1371/journal.pcbi.1003290.

[61] A. Abakuks, R. W. Hiorns, and D. Cooke, "The mathematical theory of the dynamics of biological populations ii.," *Journal of the Royal Statistical Society. Series A (General)*, vol. 145, no. 4, p. 512, 1982, ISSN: 0035-9238. DOI: 10.2307/2982110.

[62] I. Kovacic and M. J. Brennan, Eds., *The Duffing Equation*. John Wiley & Sons, Ltd, Mar. 2011, ISBN: 9780470977859. DOI: 10.1002/9780470977859.

[63] M. Brešar, P. Boškoski, and M. Horvat, "Detection of coupling in duffing oscillator systems," *Chaos: An Interdisciplinary Journal of Nonlinear Science*, vol. 31, no. 6, 063130, Jun. 2021, ISSN: 1089-7682. DOI: 10.1063/5.0050790.

[64] M. Brešar and P. Boškoski, "Directional coupling detection through cross-distance vectors," *Physical Review E*, vol. 107, no. 4, 044220, Apr. 2023, ISSN: 2470-0053. DOI: 10.1103/physreve.107.044220.

[65] R. G. Andrzejak, D. Chicharro, K. Lehnertz, and F. Mormann, "Using bivariate signal analysis to characterize the epileptic focus: The benefit of surrogates," *Physical Review E*, vol. 83, no. 4, 046203, Apr. 2011. DOI: 10.1103/PhysRevE.83.046203.

[66] A. Ovsenik, M. Podbregar, N. Lakič, *et al.*, "Neurovascular coupling in severe aortic valve stenosis," *Brain and Behavior*, vol. 13, no. 8, e3155, Jul. 2023, ISSN: 2162-3279. DOI: 10.1002/brb3.3155.

[67] T. De Silva and F. Faraci, "Hypertension," in *Primer on Cerebrovascular Diseases*. Elsevier, 2017, pp. 153–157, ISBN: 9780128030585. DOI: 10.1016/b978-0-12-803058-5.00031-x.

[68] G. Panczel, M. Daffertshofer, S. Ries, D. Spiegel, and M. Hennerici, "Age and stimulus dependency of visually evoked cerebral blood flow responses," *Stroke*, vol. 30, no. 3, pp. 619–623, Mar. 1999, ISSN: 1524-4628. DOI: 10.1161/01.str.30.3.619.

[69] S. Purkayastha and F. Sorond, "Transcranial doppler ultrasound: Technique and application," *Seminars in Neurology*, vol. 32, no. 04, pp. 411–420, Jan. 2013, ISSN: 1098-9021. DOI: 10.1055/s-0032-1331812.

[70] B. Rosengarten, C. Aldinger, A. Kaufmann, and M. Kaps, "Comparison of visually evoked peak systolic and end diastolic blood flow velocity using a control system approach," *Ultrasound in Medicine and Biology*, vol. 27, no. 11, pp. 1499–1503, Nov. 2001, ISSN: 0301-5629. DOI: 10.1016/s0301-5629(01)00464-1.

Bibliography

Publications Related to the Thesis

[1] M. Brešar, P. Boškoski, and M. Horvat, "Detection of coupling in duffing oscillator systems," *Chaos: An Interdisciplinary Journal of Nonlinear Science*, vol. 31, no. 6, 063130, Jun. 2021, ISSN: 1089-7682. DOI: 10.1063/5.0050790.

[2] M. Brešar and P. Boškoski, "Directional coupling detection through cross-distance vectors," *Physical Review E*, vol. 107, no. 4, 044220, Apr. 2023, ISSN: 2470-0053. DOI: 10.1103/physreve.107.044220.

[3] A. Ovsenik, M. Podbregar, N. Lakič, *et al.*, "Neurovascular coupling in severe aortic valve stenosis," *Brain and Behavior*, vol. 13, no. 8, e3155, Jul. 2023, ISSN: 2162-3279. DOI: 10.1002/brb3.3155.

Biography

Martin Brešar was born on November 4th, 1994, in Maribor, Slovenia. In 2014, he graduated from II. gimnazija Maribor and went on to study physics at the Faculty of Mathematics and Physics in Ljubljana. He completed his bachelor's degree in 2017 and continued in the master's program in mathematical physics. He began working at the Jožef Stefan Institute during the last year of his master's studies. In 2020, he finished his master's thesis titled "Direction of Coupling in Nonlinear Systems" and received the Prešeren Award of the Faculty of Mathematics and Physics for an outstanding thesis. He was then accepted into the Young Researcher Programme and continued his work at the Jožef Stefan Institute under the supervision of Assoc. Prof. Dr. Pavle Boškoski. His research focuses on advancing directional coupling detection methods and their applications, with publications in several international journals.